NanoJanus and Nanosatellite Assembly for Biomolecular Delivery and Cancer Therapeutics

by

Kanokwan Sansanaphongpricha

A dissertation submitted in partial fulfillment
of the requirements for the degree of
Doctor of Philosophy
(Pharmaceutical Sciences)
In the University of Michigan
2017

Doctoral Committee:

Professor Duxin Sun, Chair
Professor Jinsang Kim
Assistant Professor Yu Lei
Professor Adam J. Matzger
Professor Steven P. Schwendeman
Professor David E. Smith

Kanokwan Sansanaphongpricha

kanokwas@umich.edu

ORCID iD: 0000-0002-2517-8556

©Kanokwan Sansanaphongpricha 2017

DEDICATION

To my family and everyone who believe in sciences

ACKNOWLEDGEMENTS

I would like to thank many people who either directly or indirectly support my study, my work, and my personal life. Firstly, I would like to thank my dissertation advisor, Professor Duxin Sun, who is a great mentor and gave me a huge opportunity in my life to pursue my Ph.D. study at University of Michigan. He has broadened my academic points of view since the day I emailed him to show my interest in his research. My life would not come this far without his support and advice. His perspectives inspire and encourage me to conduct research creatively and positively.

Secondly, I would like to thank my committee members, Dr. Steve Schwendeman, Dr. David Smith, Dr. Adam Matzger, Dr. Jinsang Kim, and Dr. Yu Lei, who always constructively suggest me along the way of my Ph.D. study. I also thank my collaborators Dr. Wei Cheng, Dr. Michael DeSantis, and Dr. Kai Sun, who worked on the Janus nanoparticle project with me and provide me critical feedbacks. Another important collaboration is the Head and Neck cancer vaccine that I worked with wonderful people in Lei lab. I am thankful for the opportunity Dr. Yu Lei handed in to me to work with him and his lab. He introduced me to the world of immunology and guided me along the project. I felt amazed by people who work diligently and helpfully in his lab. It was a great time to work with Dr. Xinyi Zhao, Toktam Moghbeli, Xiaobo Luo, Blake Heath, and especially Dr. Yee Sun Tan, who instilled me many immunological

and biological techniques as well as motivated me to acquire more immunology knowledge.

I also thank faculties from the Pharmaceutical Sciences department, Dr. James Moons, Dr. Gus Rosania, Dr. Kathleen Stringer, Dr. Beata Chertok, and Dr. Amit Pai who discussed with me regarding academic projects, future careers, and exchanged perspectives. I am also thankful to administrative staff in the College of Pharmacy to always assist me in student business included Marisa Gies, Patrina Hardy, Antoinette Hopper, Jeanne Getty, Maria Herbel, Gail Benninghoff and Elaine Griffin.

Many people in Sun lab are very supportive and have established very nice friendships to me since the day I have joined the lab. So, I would like to thank Dr. Hayley Paholak, Dr. Jamie Connarn, Dr. Rebecca Moody, Nathan Truchan, Mari Gasparyan, Chang-Ching (Albert) Lin, Ila Myers, Alex Yu, Garrett Johnson, Jamie Do, Nicholas Stevers, Samantha Tinsley, Dr. Joseph Burnett, Dr. Xin Luan, Dr. Miao-Chia Lo, Dr. Hebao Yuan, Dr. Wen Bo, Miao He, Huixia Zhang, Dr. Jinhui Liao, Dr. Jeremy Felton, Dr. Yanyan Han, Dr. Siwei Li, Dr. Pan Shu, Dr. Ruijuan Luo, Xiaoqing Ren, Dr. Honglin Ren, Dr. Lichao Sun, Mike Bly, Chun Tao, and Dr. Hongwei Chen, who supervised me in many aspects.

I would like to thank my friends, who encourage and always stand beside me including Rungroj Jintamethasawat, Patipan Prasertsom, Plengrapin Buason, Anusarn Sangnimnuan, Dr. Anchitta Satjarak, Dr. Arranee Chotigo, Suchawan Pornsukarom, Pichamon Limcharoenchat, Wasimon Tosuratana, Dr. Thunyarat Amornpetchkul, Dr.

Supang Khondee and many people from Thai Student Association at University of Michigan.

I am also thankful to Royal Thai government for my fellowship and Thai embassy in Washington D.C for document work.

Last and the most important, my family, my mother, my sister, my father, and Ozan Kuru for always support me and believe in me. I would like to thank Ozan who always helps me academically and personally. He has helped review, advise, and support in many of my work and makes my life very happy in everyday. Finally, my mother and my role model, Supathra Songja, who always attaches significance to education of her kids. She is a very hard-working and positive woman. Without her strong support, my life would not be this happy. The other important in my life is my sister, Panisara Sansnaphongprichar. She is a huge part in my life and inspired me to interest in sciences. She is my first teacher in many aspects of learning. Without her, I would not know how to write, how to drive and how to bike. I am very proud of my small family and I know they are also proud of me as well.

Table of Contents

List of Tables

List of Figures

ABSTRACT

Nanotechnology has been utilized widely in medical fields to improve the treatment and diagnosis of several diseases. One of the key players to drive medical nanotechnology forward is nanoparticles, which have been intensively studied and used as a tool for imaging, drug delivery, and disease treatments. Gold and iron oxide, undoubtedly, are on the short list of the nanoparticles used in medical nanotechnology due to their biocompatibility, tunable surface, and unique physico-chemical properties. In this dissertation, we developed novel nanostructures using gold, iron oxide nanoparticles and polymers for various applications including Janus motors, vaccine delivery, and controlled drug release.

We generated an asymmetrical Janus nanostructure using thermo-cleavable polymer, gold, and iron oxide nanoparticles for photothermal enhancement and nano motors through an active rotational motion. Gold/iron oxide Janus nanoparticles (JNS) are developed by a seed-mediated self-assembly using a thermo-cleavable polymer facilitating the process. The formed JNS strongly displays an asymmetrical photothermal effect to activate a rotational motion and enhances photothermia resulting in significant cell killing effects under weak near-infrared (NIR) light exposure. In addition, the JNS displays distinct active rotational motion under NIR laser light due to

the temperature gradient at its surface, which can be used potentially as Janus motors for drug delivery in the future. We next harnessed the same thermo-cleavable polymer used in JNS formation for controlled drug release under NIR laser light irradiation. The iron oxide nanoparticles (IONP) were first encapsulated in the thermo-cleavable polymeric micelles with doxorubicin (Dox), a chemotherapeutic drug. After NIR trigger, the polymer is cleaved due to heat transfer from the IONP resulting in the release of doxorubicin from the micelles. This study demonstrated that the thermo-cleavable polymer could be used as a smart material for controlled drug release.

We also generated another type of secondary structure, a “gold/iron oxide nanosatellite”, using poly (γ- methacryloxypropyl trimethoxysilane) -*b*- poly (ethylene oxide) polymer (MPS-*b*-PEO). This nanosatellite structure, in which IONP is a central core and surrounded by multiple gold nanoparticles as satellites, is used for delivering antigens and an adjuvant for HPV^+ head and neck cancer treatment. These nanosatellites deliver high surface density of E7/E6 oncogenic peptides and cyclic-guanosine-adenosine monophosphate (cGAMP) adjuvant to antigen presenting cells (APC) and further activate type I interferon (IFN-I) response. The nanosatellite vaccine also promotes antigen specific $CD8^+$ T cells to infiltrate the tumors and inhibits tumor growth in an HPV^+ head and neck tumor model when used as a single therapy or in combination therapy with an anti PD-L1 antibody. Nanosatellites offer many advantages for antigenic peptide and adjuvant delivery such as having a larger surface area, higher antigenic peptide density, higher cell uptake, and lower systemic elimination.

This thesis presents the versatile developments and applications of gold/iron oxide nanostructures (Janus and Nanosatellite) which have advantages for drug and vaccine delivery in the future.

CHAPTER 1

INTRODUCTION

1.1 Nanoparticles

A nanoparticle by definition refers to a particle that has a characteristic dimension from 1 to 100 nm and shows a unique property that is different from non-nanoscale particles with the similar chemical composition[1,2]. Nanoparticles can be made from diverse materials such as polymers, lipids, or inorganic metals. Among these materials, gold and iron oxide nanoparticles are on a short list due to their tunable surface, imaging property, photothermal property, and biocompatibility[3,4]. In this dissertation, we focus on gold and iron oxide nanoparticles used for photothermal effects, Janus motors, controlled release and biomolecular delivery.

Iron oxide nanoparticles

Iron oxide nanoparticles (IONP) or magnetic nanoparticles are mostly made of γ-Fe_2O_3 (maghemite) or Fe_3O_4 (magnetite), which have superparamagnetic properties when the size is small enough (< 15nm). IONP becomes a popular candidate for biomedical applications due to its excellent safety profile. Superpara iron oxide

nanoparticles (SPION) exhibit strong response under a magnetic field, which are very useful for magnetic resonance imaging(MRI) and magnetic hyperthermia[5]. The most common methods to synthesize SPION are coprecipitation and thermal decomposition. Although coprecipitation method is easy and can produce SPION in a large scale, the size distribution is relatively wide. While, thermal decomposition requires a more complicated method, the size distribution is well-controlled. Regardless of the synthesis approaches, the major problem of SPIONs is they are not stable without a suitable coating. They tend to aggregate in physiological media or under a strong magnetic field[6]. To solve this problem, stabilizers or surface coating are required to inhibit the SPION aggregation[7]. These stabilizers and coating, generally, create either electrostatic and/or steric repulsions among SPIONs.

I. Surface functionalization

There are several functional groups interacting with the surface of SPION to prevent them from agglomeration and also to further conjugation with drugs, peptides, DNA/RNA or another inorganic nanoparticles[8]. Most commonly used functional groups to react with the SPION include polysiloxanes, carboxylic acids, diols, and phosphonic acids (Figure 1.1)[9]. A large number of hydroxyl groups are generated from iron atoms when SPION is in an aqueous solution making them readily to react with the above mentioned functional groups. Phosphonic acid derivatives demonstrate the highest grafting density followed by carboxylic acid and glycerol respectively. Carboxyl groups can be easily removed by temperature or replaced with higher affinity ligands such as phosphonic acid and alkoxysilanes[10,11]. Some coatings have been approved by Food

and Drug Administration (FDA) such as carboxy-dextran coated SPION (RESOVIST) for MRI[12]. Polyethylene glycol (PEG) with different molecular weights and functional groups are also widely used for SPION coating due to stealthy property. PEG can react with a variety of functional groups. For example, carboxylic acid-PEG coated SPION can be further modified with carbodiimide (EDC)-/sulfo N-hydoxysuccinimide (NHS) coupling chemistry for covalent linking of primary amine and carboxylic acid groups. The single dispersed SPION with suitable bi-functional groups are ready for further conjugations with other molecules such as peptides, DNA/RNA, antibodies, and inorganic metals, which helps expand the applications of SPION for targeted drug delivery and imaging. BSA coated SPION were conjugated with Arg-Gly-Asp (RGD) peptide to target $\alpha_v\beta_3$ integrin on metastatic tumor and tumor endothelial cells via thiolated PEG[13]. Membrane translocation MPAP peptides and siRNA were conjugated on the surface of dextran coated SPION via heterobifunctional linkers, m-maleimidobenzoyl-N-hydroxysuccinimide ester (MBS) crosslinker for MRI and optical imaging[14].

Not only are the single dispersed SPIONs used for biomedical applications, clustered SPIONs such as micelles or liposomes are also applicable for delivery and theranostics. The size range of SPION liposome is 100- 5,000 nm in which SPION are inserted into lipid layer of the liposome or interact with hydrophobic polymers in micelles and form stable structures[10]. Palmityl-nitro DOPA-modified SPION were encapsulated in lipid bilayer of liposomes demonstrates the controlled release of calcein dye as a model drug under alternating magnetic field (AMF)[15]. Oleic coated SPIONs formed stable micelles after mixing d-α-Tocopheryl-co-poly(ethylene glycol) 1000 succinate or vitamin

E TPGS polymer, which have better cellular uptake and T2 mapped MRI in a xenograph mouse model[16].

II. Pharmacokinetics, toxicity and biodistribution of SPION

Pharmacokinetics, toxicity and biodistribution of SPIONs are determined by several factors including size, surface charge, shape, and coating materials[17]. SPIONs are mostly considered biocompatible, which have good safety profiles. SPION can be physiologically metabolized and degraded into free iron ions resulting in the temporary increase of iron amount presenting in the serum. High dose of SPION can cause iron over load in the serum and show toxicity. Reticuloendothelial systems (RES) such as liver, lung, and spleen are the major organs uptaking SPION. Dextran-coated SPIONs were excreted through urine and feces after intravenous injection. *In vivo* data of 10 nm polyol-maghemite nanoparticles show that the nanoparticles mainly accumulated in rats' liver, kidneys, and lungs, while brain and heart remain unaffected. 40% of the nanoparticles were removed from serum within 24 hours and 75% of the nanoparticles were excreted via urine within 72 hours[18]. However, *in vitro* data suggest that the toxicity levels are different across the cell types. The same concentration of SPION (2.25 mM) shows toxicity to human brain cells but compatibility with human kidney cells. The same study also demonstrates that positively charged SPIONs are more toxic than negatively charged SPIONs[19].

Gold nanoparticles

Gold nanoparticle (AuNP) is one of the oldest kinds of nanoparticles that was discovered and used in ancient medicines[20]. This noble metal exhibits vivid colors by nature, which makes it very attractive for investigation[21]. Beyond its beauty, AuNP possesses distinct properties such as surface plasmon resonance, photothermal effect, photodynamic effect, tunable surface, and ionizing radiation[20,22–25].

AuNP can be synthesized in many ways. The most commonly used techniques are Turkevich method, and Brust and Schriffin method. Turkevich used citrate as a reducing and stabilizing agent, yielding water soluble AuNP with the size ranging from 16- 150 nm[26–29]. Brust and Schriffin developed a new way to synthesized alkanethiol-stabilized AuNP with smaller diameter, 1.5-5 nm by using a two-step method. Tetraoctylammonium bromide (TOAB) is used as the phase transfer reagent and sodium borohydride ($NaBH_4$) is used as the reducing agent[30].

Last decades, AuNPs have been developed in different morphology such as gold nanorod (AuNR), gold nanocage, and gold nanostar, or combined with different compositions such as silicon, iron oxide, or silver[31]. These unique shapes and compositions broaden the applications of AuNP-based materials. Gold nanorods (AuNR) and gold nanoshells (AuNS) display strong photothermal effect due to the decay of the plasmon resonances in Au nanocrystals[24]. Gold nanocages are useful for photoactivated drug release, in which a drug is encapsulated inside and released after near infrared laser light irradiation[32]. Gold nanostars exhibit distinct gyromagnetic scattering for enhanced optical contrast under a magnetic field[33]. The surface of AuNP

is ready for further conjugation. This session covers the surface functionalization of AuNP, its biodistribution, and some applications related to next chapters.

I. Surface functionalization

One of the most important reasons that AuNP gains a lot of attention in research is the ease of surface decoration. AuNP can be conjugated with several types of molecules such as peptides, oligo nucleotides, small molecular drugs, and metals. General functional groups interacting with AuNP include thiolate, dithiolate, dithiocarbamate, carboxylate, amine, selenide, phosephine, or isothiocyanate moieties. While thiol-based functional group has been commonly used for non-labile covalent bonding, amine and carboxylate groups are mostly used for acid-base labile conjugations. The chemisorption between thiol and Au happen quickly in millisecond to minutes. A variety of bifunctional crosslinkers are available for AuNP conjugation such as thiol-NHS, thiol-COOH, thiol-NH_3, click thiol-azide, or thiol-alkyne. However, thiols can also rapidly form disulfide bonds among themselves[34]. Using protected thiol functional groups such as ortho-pyridyl disulfide (OPSS) or actylthio can minimize the self-interaction but deprotection is required before use[35,36]. Dithiothreitol (DTT) and tris (2-carboxyethyl) phosephine (TCEP) are common reagents to reduce the disulfide bonds or deprotect the protected thiol groups[37]. Peptides containing a free cysteine can directly conjugate onto the surface of AuNP[38]. Polyethylene glycol (PEG) with different molecular weights usually insert between bifunctional groups to help stabilize the

conjugated molecules and also make them more flexible allowing the molecules to rotate and fit the target sites better[39].

II. Pharmacokinetics, toxicity and biodistribution of AuNP

Pharmacokinetics of AuNP has been intensively studied in both *in vitro* and *in vivo* models. Size, surface charge, shape, and coating are the key parameters determining the fate of the AuNP[40]. Many pieces of evidence show that AuNPs are internalized by liver macrophages, secreted through the bile, and eliminated through feces[41].

The correlation study between biodistribution and size of AuNP shows that after IV. injection of AuNP with the diameter 2-40 nm into mice, 90% of AuNP were found in macrophages in the liver and 10% in macrophages in the spleen[42]. The studies in mice and rats demonstrate the similar trend that the major organ uptaking AuNP is liver; however, the smaller size of the AuNP (10 nm) has higher distribution to kidney and brain than larger size of AuNP (50, 100, and 200 nm)[43,44]. In other words, the smaller sizes of AuNP have higher diffusional displacement. Another study shows that ultrasmall AuNPs with 1.9 nm diameter have very rapid clearance from the serum. The gold concentration in the serum drops by half within 10 minutes after IV injection[45]. AuNPs also have different distribution in blood. Small AuNPs prefer to stay in serum, while large AuNPs interact with blood cells[46]. Sadauskas investigated long term biodistribution of 40 nm AuNP in mice. Interestingly, the gold content in the liver reduce by only 9% after 6 months of IV injection suggesting that AuNPs have long-term accumulation in the body. It is believed that the mechanism of AuNP elimination in liver

mainly happens in Kupffer cells. Neighboring Kupffer cells phagocytosed the Kupffer cells damaged by the AuNP[47].

In addition to size effect of AuNP, the surface coating is similarly important. It has been known that higher density of PEG coated on the surface of AuNP helps prolong the blood circulation of AuNP due to the reduction of protein absorption of the AuNP[48]. Comparing the excretion of 2 nm AuNP with different coating ligands shows that glutathione coating has the most renal clearance due to the best stability in blood compared to citrate and cystine coating[21]. However, the nanoparticles with the hydrodynamic diameter less than 6 nm can be totally eliminated through glomerular filtration regardless of surface charge, while the renal clearance of the nanoparticles with the hydrodynamic diameter 6-8 nm depends on the surface charges. Cationic nanoparticles have higher glomerular filtration than anionic particles[45,49]. Charge-selective glomerular filtration is influenced by the negative charges of the capillary wall in the kidney preventing the anionic nanoparticles to entry[50] (figure 1.2). Sometimes, nanoparticle aggregation in physiological fluid can increase the overall size of the nanoparticles hence they will be uptake to the liver and excreted through feces[51].

Toxicity studies of AuNP have been widely explored. AuNPs are unlike bulk gold. They are more reactive and could be toxic at high concentrations. Smaller AuNP tends to be more toxic than larger size due to high reactivity and oxidative stress resulting in mitochondria damage[52]. LD_{50} of Au is 3.2 g/kg[53,54]. However, there are several factors needed to be considered such as size, charge, and coating materials as mentioned earlier. *In vitro* models cannot always predict *in vivo* results. Therefore, the use of AuNP is still limited in clinical practice and further studies need to be explored.

1.2 Photothermal effect of nanoparticles

Photothermia results from photoexcitation leading to the partial or total production of heat [55]. This phenomenon is more obvious in nanoscale metals such as gold, silver and magnetic particles. The coherent collective oscillation of electrons in the conduction band influences large surface electric fields, intensifying the radiative properties of those metals when interacting with resonant electromagnetic radiation. The strongly absorbed radiation then converts effectively into heat on a pico second time domain attributed to electro-phonon or phonon-phonon processes[56]. This discovery allows researcher to utilize the photothermal effect in cancer treatments, in which photothermal contrast agents were administered into the body followed by a light trigger to raise local temperature at tumors. The cumulative heat in the tumors subsequently ablates the cancer cells by disrupting the cell membrane[57–59]. This method provides an alternative for chemotherapy in drug-resistant patients.

In the first generation of AuNP, gold nanospheres were utilized for hyperthermia applications with the visible region of light approximately 514 nm, which is close to absorption spectrum of AuNP[60]. However, using the UV-VIS light is not favorable due to the serious skin damage in a real clinical setting. An alternative option is to employ near-infrared (NIR) light with the wavelength 650- 900 nm. NIR is considered safer to use as it has far less skin damage and has low absorption by biological fluid including hemoglobin. Last decade, the attention has been shifted from gold nanospheres to gold nanorods, gold nanoshells, gold nanocages, and gold nanosphere clusters because

they can absorb the incident light in NIR region, which is more suitable for clinical use[61] (figure 1.3).

J.L. West group from Rice university discovered Gold nanoshells (GNS) in 2003 and proved that GNS raised the temperature significantly after 6 minutes of NIR laser irradiation resulting in irreversible tumor tissue damage[62]. Another candidate for photothermal therapy is gold nanorods (GNR), which was first developed by El-Sayed group at Georgia tech in 2005. The absorption wavelength of GNR depends upon the aspect ratios of the particle such as transverse and longitudinal axes. The transverse axis plays an important role in NIR light absorption[56]. The major challenge of GNR is the loss of its surface aspect ratio after long exposure to the NIR laser light. The longitudinal axis of GNR slowly melts and it subsequently reshapes to gold nanosphere, which absorbs the VIS light. However, the melting effect of GNR depends on the surface coating. PEG can help slow down the loss of the surface aspect of GNR[63].

In addition to Au-based nanoparticles, magnetic nanoparticles such as Fe_3O_4 also demonstrate photothermal property. Kim et al first reported the use of SPION to produce heat under a pulse laser light at 532 nm[64]. Later, SPIONs with highly crystallinity were developed and able to absorb the NIR light. Chen et al showed that the orientation character along the (100) and (110) lattice planes of the SPIONs synthesized by thermal decomposition significantly contributes to the photothermal capability of SPION. The local temperature raised 33 °C from the beginning after 10 minutes of NIR laser illumination[65].

There are many materials currently being explored for photothermal effect including NIR dyes, carbon nanotubes, and polypyrrol. However, only Aurolase, gold nanoshells, has just completed the clinical trial for head and neck cancer treatment at the end of 2016. The long-term results need further investigation. An important challenge of photothermal therapy is the nanomaterials under the skin are not sufficiently sensitive to NIR laser. The penetration of NIR light is limited only 2 mm under skin; therefore, strong laser power is required[66]. The high laser power can cause damage to normal tissue leading to adverse effects, which hamper the use of PTT in clinical trials. In summary, new materials with high sensitivity for NIR laser light still need to be developed for better photothermal treatment.

1.3 Secondary structures

Secondary structures refer to the structures that form secondary self-assembly from secondary building blocks such as worm-like micelles, vesicular structures, hexagonal structures or liquid crystal structures (figure 1.4). The secondary self-assembly is induced by either aggregation or crosslinking. The interaction between two secondary building blocks can be either attraction or repulsion. The direct secondary self-assembly can happen only the attraction > repulsion force. The molecular rearrangement follows the law of thermodynamics, obeying the energetics of each case; therefore, the secondary structures can appear in several forms[67]. A systematic analysis of the structures of the building blocks is a crucial parameter to govern the self-assembled aggregates regardless of their structural hierarchies. The secondary self-

assembly can form in either symmetric or asymmetric morphology depending upon the directional packing segments[68–70]. Hierarchical self-assembly is influenced by multiple factors such as polymer architects, intrinsic block functionality, and external triggers (Figure 1.5)[71]. In this dissertation, we demonstrate the controllable secondary self-assembly for both asymmetrical and symmetrical structures. A multi-building block Janus nanostructure and a nanosatellite structure are examples for asymmetrical and symmetrical formations respectively.

Asymmetrical Janus structures

Janus, in terms of particles, has been named after the Roman God, who has two faces on the opposite direction. This term has been adopted to explain the nanoparticles that have two different properties on the opposite side of the particles including materials, surface ligands, and morphologies[72]. There are several approaches to develop Janus particles such as surface masking, co-jetting, crosslinking, and self-assembly techniques[73]. However, we focus only on the self-assembly approach in this dissertation. Self-assembly of nanoparticles is able to generate asymmetricalstructures if the different building blocks have different favorable packing direction[74]. These building blocks will form the structure that keeps themselves the most stable.

Asymmetrical structures provide different applications from conventional symmetrical structures. First, two different surfaces of the Janus can conjugate with bi-ligands in an asymmetrical fashion resulting in bi-specific binding to two different types of cells. Another example is Janus motors, in which one side of the Janus particle can

react with a catalyst reagent creating a propellant and driving the particle forward in a uni-direction[75]. The concept of Janus motors has been recently introduced to a biomedical application for cargo delivery and permeability enhancer[76,77]. Nevertheless, the thorough investigations for possible clinical usage and long-term safety are still required

1.4 Nanoparticles for vaccine delivery

Vaccine definition by CDC refers to a product that boosts a person's immune system to produce immunity to a specific disease and protect one from that particular disease. Vaccines have long been used for 215 years since it was first discovered by the farmer Benjamin Jesty and the physician Edward Jenner, who implemented attenuated pustules from cowpox and inoculated to people preventing them against smallpox. Since then the word vaccine and this technique have spread worldwide with on-going development[78,79]. Several decades ago, vaccines were mainly made from whole-cell pathogens, live attenuated pathogens, and inactivated pathogens. However, these conventional types of vaccine have greatly safety concern. Later, subunit vaccine, DNA vaccines, and peptide vaccines were developed to improve the safety; however, these vaccines provide lower immunogenic response. As a consequence, an adjuvant may be required to help elicit better immune response (figure 1.6) [80]. Currently, vaccine products mostly contain both an antigen and adjuvant. Adjuvants are substances added into vaccine products in order to boost the immunogenicity of an antigen. Adjuvants can be ranging from the classical ones such as alum and Freund's adjuvants to modern ones which engage the pathogen-associated molecular pattern (PAMPs) such as oligodeoxynucleotides (ODN)[81,82]. The classical adjuvants are likely to stimulate inflammasome non-specifically, while modern adjuvants can specifically bind to pattern recognition receptors (PRR) such as STING, TLR 9 and NLR, which can subsequently elicit more effectively T helper cell response[82].

However, recombinant DNA antigens, soluble peptide antigens, and water-soluble adjuvants are not effectively internalized by antigen presenting cells *in vivo* due to rapid degradation and diffusion regardless of their strong potency *in vitro*. This hampers the use of these molecules in clinical setting. With the advent of nanotechnology, nanoparticles have been deployed to assist soluble antigen and adjuvant delivery to antigen presenting cells (APC) such as dendritic cells and macrophages by either passive or active ligand targeting methods.

1.4.1 Passive and active delivery

1.4.1 a) Passive vaccine delivery

Passive delivery is mostly controlled by size of the nanocarriers. The nanoparticles with the size less than 200 nm can travel to lymph nodes directly and are internalized by APC in lymph nodes, while the nanoparticles with the size larger than 500 nm are uptake by peripheral APC at the site of administration and then travel to the lymph nodes. The former provides the better adoptive immunity because first, less than 5% of APC travel from the site of administration to lymph nodes and second, the antigens can directly interact with B cells through B cell receptors (BCR) and positively influence the antibody production[81,83–85].

1.4.1. b) Active vaccine delivery

Likewise, other active targeting deliveries, vaccine can also specifically target to dendritic cells (DC). Some targeting ligands were used to deliver an antigen to DC such as CD-40, DEC-205, and gp 96[86,87]. However, to target DC, the choices of ligands used

depend upon specific DC subtypes. For example, DEC-205 expresses on the surface of $CD8^+$ DC and presents the antigen in a context of both MHC-I and MHC-II, while 33D1 expresses $CD8^-$DC and presents the antigen on only MHC-II[88]. DC targeting is not only for antigen delivery, but also provides some specific signal that might polarize the DC in different manners. For instant, Targeting DC with asialoglycoprotein receptor induces DC to secrete IL-10 and polarize T cells into suppressor T cells[88]. Thus, targeting DC for appropriate immune response remains challenging. More deep investigations need to be conducted.

Ex vivo techniques have also been used to activate DC outside the body and the cells are re-administered back to *in vivo*. This approach is so called “Dendritic cell vaccine”. This method readily primes DC to present the antigens to T cells and strongly boost the cytokines secretion from DC, which provides better T cell activation[88]. DC vaccine can also increase the positive NK cell responses and support the production of cytotoxic T lymphocytes (CTL) immunity resulting in tumor rejection. There are some on-going clinical trials of DC vaccine mostly are in phase I/II against melanoma. Overall toxicity reports are tolerable. Systemic side effects are rare and patients’ life quality seems to be preserved[89]. However, DC vaccines are considered as personalized therapy because DCs are generated and expanded from the patients to prevent rejection. There are some critical challenges to implement this technique including the standard procedures of the manufacturing, quality controls, consistency, routes of administration[89]. Moreover, it is less than 5% of *ex vivo* activated DC reaching the lymph nodes. This dampens the effect of activated DC leading to low immune response

and pre-condition may be required[90]. Nevertheless, the discovery of this technology laid the platform for future DC vaccine and move to the forefront of cancer immunotherapy.

1.4.2 Factors influencing the nanoparticle engineering for vaccine delivery

Nanoparticles play a crucial role in facilitating antigen and adjuvant delivery to APC. Numerous studies show that antigen and/or adjuvant-loaded nanocarriers elicit better immune responses, reduce off targets, reduce doses of antigens and adjuvant used, and protect antigens and adjuvants from degradation. However, there are several criteria contributing to a delivery system. Size, surface charges, morphology, elasticity, and antigen density on the surface of nanoparticles contribute to overall immune response and toxicity.

1) **Size:** As mentioned in the earlier session, it has been well studied that nanoparticles with the size less than 200 nm can directly travel to lymph nodes, whereas the nanoparticles with the size larger than 500 nm required APC trafficking to lymph nodes due to the narrow lymph node capillary. However, the APC can squeeze themselves and penetrate the endothelial layer and traffic to the lymph nodes[91,92]. The optimal size for DC uptake is approximately 40 nm[81]. Microparticles are more favorable to be internalized by macrophages[93]. Although both DC and macrophages are considered as professional APC, delivering antigens to DC is more preferred because the antigen cross-presentation to T cells is more efficient in DC. Macrophages tend to degrade the antigen in lysosome after phagocytosis rather than to present it to MHC-I/II in endoplasmic reticulum[94].

2) **Surface charges**: similarly to other cells, cationic nanoparticles are uptake more efficiently in APC than anionic nanoparticles due to the interaction with negatively charged plasma membrane. However, the limitation of cationic nanoparticles is toxicity. The cationic nanoparticles can cause acute systemic toxicity and nonspecific systemic immune responses. Chen et al show that many types of cationic nanoparticles such as PEI, polylysine, cationic dextran and cationic gelatin can interact with TLR4 and induce the release of IL-12[95]. The charge effect is more complicated when the nanoparticles bound with plasma proteins, which impacts the cell uptake and biodistribution.

3) **Morphology:** The shapes of the nanoparticles affect not only the cellular uptake but also cytokine productions. The ability of cellular uptake relies on the angle of the nanoparticles that contacts to the cells. For asymmetrical nanoparticle such as nanorods, the cellular uptake is increasing if the transverse axis interacts with the cell membrane. Agarwal and his team discovered that nanodiscs have higher uptake in bone-marrow derived macrophages (BMDM) than nanorods[96]. Moreover, different morphologies of the nanoparticles influence different cytokine productions. Nanorods are likely to promote inflammasome-related cytokine release such as IL-1β and IL-18, while nanospheres induce proinflammatory cytokine release such as TNF-α and IL-6. T cell polarization is also affected by the morphology of the nanocarriers. Nanospheres promote both Th1 and Th2 polarization against OVA antigen, whereas nanorods promote only Th2 polarization[97].

4) **Elasticity of nanoparticles:** Nanoparticles with higher elasticity have higher lymph node accumulation compared to the rigid nanoparticles with the same size. The nanoparticles with elasticity can squeeze themselves through the paracellular of the endothelial cells and travel to lymph nodes[81]. Moreover, elasticity of nanoparticle facilitates the antigens or targeted ligand conjugated on the surface of the nanoparticles bind to the cell surface receptor easier due to the binding flexibity[98].
5) **Ligand density:** Ligand or antigen density is a key factor to stimulate a proper immune response. DCs have to present a sufficient density of peptide-MHC complex on their surface in order to activate T cell response. T cells, in general, ignore the low density of the peptide-MHC complex[99–101]. This is important to design the nanoparticles mimicking APCs. Furthermore, the density of the antigenic peptides and their pattern on the surface of nanoparticles determines the interaction with the B cells. Non-repetitive self-antigens usually fail to elicit B cell response[81]. In order to bind the antigens with high affinity, B cell receptors need to be sufficiently engaged with the antigens. The highly repetitive structures can induce extensively cross-linking of B cell receptors[102]. Surface antigen density also contributes to the ability of IgG to neutralize the whole antigen. The distance between the antigenic molecules should be approximately 10 nm so two identical arms of Fab of the IgG can form a strong bivalent bridge with the antigen[102]. Bandyopadhyay and co-workers show that different ligand densities on the surface of the nanoparticles induce different cytokine releases, which affects T cell response. Higher density of DEC-205, which targets DC, enhances the release of anti-inflammatory cytokines such as IL-10 via the cross-linking mechanism of the DEC-205 receptor[103].

1.4.3 Nanoparticles as a vaccine platform

Several nanoformulations have been explored for delivering antigenic peptides and adjuvants due to their ability to traffic to lymph nodes, prevent antigen and adjuvant degradation, elicit stronger immune response, and prolong the adjuvant release.

I. Inorganic-based nanoparticles

The most often inorganic-based nanoparticles used for vaccine delivery is gold nanoparticle (AuNP) due to the tunable surface and biocompatibility. As mentioned earlier that surface of AuNP readily reacts with thiol-based functional groups including cysteine on a peptide and thiol-modified oligo nucleotides. In general, the size of inorganic nanoparticle is well-controlled and can be as small as virus, which is easily uptake by DC[104,105]. PEG is usually used as a linker between AuNP and antigenic peptides, oiligo nucleotides, or adjuvants not only to increase the stability of the nanoparticles, but also to improve the flexibility of the ligands for receptor binding. The flexibility of the ligands is reported to be important for the ligands to bind with the pathogen recognition receptors (PRR) on the DC[39].

Another type of inorganic nanoparticles which has been intensively used for vaccine delivery is iron oxide nanoparticles (IONP) due to biodegradable and imaging property. IONP can be tracked without additional labelling process. IONP reduces T2 relaxivity and darkens the tissues, where it accumulates, hence the biodistribution of IONP-based vaccine can be visualized under magnetic resonance imaging (MRI)[106,107].

II. Lipid-based nanoparticles

Liposomes are the most widely used lipid-based nanocarriers for the vaccine. The antigens and/or adjuvants can be loaded either inside the liposome or conjugated on the surface[108–110]. The latter provide better immune response due to the antigenic recognition and direct interaction with PRR on the APC. Antigens and adjuvants can be conjugated on the surface by modified functional groups of lipids in liposomes. The sizes of the liposomes are mostly in the range of 100-500 nm, which is larger than inorganic nanoparticles in general. Cationic liposomes have higher cellular uptake compare to anionic and neutral ones. Some types of lipid such as a combination of phosphatidylethanolamine with carboxylic compounds offer the pH-triggered release. This pH-sensitive liposome can release the antigens and adjuvants in acidic pH of lysosomes via protonation.

Recently, synthetic high density lipoprotein (HDL) has been used to deliver the antigens and adjuvants. HDL can form nanodisc structures with diameter *ca* 10 nm, which is much smaller than conventional liposomes. This facilitates DC uptake and trafficking to lymph nodes resulting in great immune response[111].

III. Polymer-based nanoparticles

Poly (lactic-co-glycolic acid) or PLGA polymer is one of the most widely used for vaccine delivery due to its biodegradability, high safety profile, and FDA approval. The advantages of PLGA particles over the liposomes are the ability to slowly release the antigens and cost-effectiveness. PLGA particles offer the slow release by bulk erosion mechanism. The release rate can be manipulated by the ratios between glycolic and lactic acid, and molecular weight of the polymer[112]. Antigens and adjuvants are mostly

loaded inside the particles, which provide better protection for the cargos against external degradation[91]. However, the trapped molecules, sometimes, cannot fully release resulting in low antigen processing. Size of PLGA particles could be nanoscale or microscale; nevertheless, nanoscopic PLGA particles are more suitable to use as a vaccine platform than microparticles due to higher DC uptake[112].

IV. Viral-like nanoparticles

Viral-like nanoparticles (VLP) is basically a self-assembly viral capsid without infection or reproducibility due to the lack of genome. VLP is considered safer than live-attenuated viral vaccine. VLP elicits very strong both innate and adaptive immune response mainly because of the self-antigenic property and high immune cell uptake[113,114]. Human papilloma virus (HPV) vaccine (Gardasil and Cervarix) approved by FDA in 2006 are examples of the VLP vaccine currently available in the market. These HPV vaccines are composed of L1 capsid protein mimicking the HPV structures, which prime the immune cells to recognize and produce antibody against the L1 capsid proteins. However, these vaccines are limited to use only prophylaxis against new infection of HPV[115,116].

In summary, nanoparticles provide substantial advantages for vaccine delivery, solve the problems of traditional vaccines, and boost the clinical outcomes. There are several vaccine platforms that can be used. Each of them provides different physicochemical characters. Mostly, there is no single system perfect for all but the vaccines are generally designed based on the purpose of treatments. The

developments of vaccine platform are avidly on-going for several infection diseases and cancers. Further studies of long-term efficacy and safety are still required.

1.5 Dissertation

Gold and iron oxide nanoparticles are selected to study in this dissertation because of their biocompatibility and biodegradability properties. Numerous studies prove their safety *in vivo*, which makes them more likely to get FDA approval as nanocomposites and for advancement to clinical trials. They also have useful intrinsic properties for multi modal theranostics. Moreover, the size of inorganic nanoparticles can be precisely controlled and most are smaller compared to lipid-based or polymer-based nanoparticles.

This study also focuses on the secondary structures of the gold/iron oxide nanocomposites because the secondary structures usually exhibit enhanced properties of the primary building blocks such as cumulative or coupling effects. Therefore, I have aimed at developing new secondary structures, both asymmetrical and symmetrical, and to explore their new properties. Asymmetrical secondary structures offer different intrinsic properties from symmetrical secondary structures such as anomalous Brownian motion, gradient photoabsorption, and uneven light scattering. These bring about novel applications, which the symmetrical structures fail to offer.

In addition to the synergistic or combinatorial intrinsic properties, the secondary structures also offer advantages for cargo delivery. The secondary structures provide a

larger surface area and different surface chemistry for different types of bio-conjugation, which make them easier to perform stepwise conjugations. In my study, I demonstrate an application of the secondary structure, nanosatellites, for vaccine delivery because they allow a method to control the antigen pattern and increase the antigen density. In contrast, the primary structures have limited surface area and are not suitable for designed antigen pattern. As mentioned earlier in this chapter, antigen density and patterns are crucial for immunogenic recognition. Low antigen density leads to poor immunogenic response.

Dissertation outline

This dissertation employs inorganic nanocomposites composed of gold and iron oxide nanoparticles to fabricate secondary structures, both asymmetrical and symmetrical, using different types of polymers.

The second chapter focuses on the invention of a thermo-cleavable polymer, which was used for the asymmetrical multi-building block Janus nanostructure formation by seed-mediated self-assembly technique. The mechanism of the Janus formation was then investigated. This asymmetrical Janus can be used as a potent photothermal contrast agent due to strong coupling effect between nanoparticles. Moreover, the uneven photothermal absorption between gold and iron oxide nanoparticles in Janus creates the active rotational motive under the near-infrared (NIR) laser light, which makes the Janus damage cancer cells more effectively than symmetrical nanoparticles.

The third chapter reports on the use of a thermo-cleavable polymer for controlled release of the model drug, doxorubicin, triggered by the NIR laser light. Iron oxide nanoparticles are used as the photothermal contrast to convert NIR light to heat, which subsequently disrupts the thermo-cleavable polymer and releases doxorubicin from the thermo-cleavable micelles.

The forth chapter investigates the development of a symmetrical nanocomposite structure composed of gold and iron oxide nanoparticles called nanosatellites. An iron oxide nanoparticle acts as a core for the attachment of gold satellites. We demonstrate the application of the nanosatellites as a SATVAC vaccine platform. The nanosatellites provide a larger surface area and very high density of E7/E6 antigenic peptide conjugation, which elicits strong specific $CD8^+$ T cell against HPV^+ (Human papilloma virus) head and neck cancer. Di-cyclic nucleotide cGAMP adjuvant was also loaded on the surface of the nanosatellites. The nanosatellite vaccine exhibits robust innate immune response by promoting the up-regulation of type I interferon genes, dendritic cells (DC) maturation, and tumor growth inhibition.

The last chapter, chapter five, the conclusions of all work in this dissertation are drawn. Future perspectives and potential applications are highlighted and discussed. An appendix denoting the work regarding the use of gold and iron oxide nanocomposites for ionizing radiation also included in this dissertation.

1.6 References

1. Auffan, M. *et al.* Towards a definition of inorganic nanoparticles from an environmental, health and safety perspective. *Nat. Nanotechnol.* **4,** 634–41 (2009).
2. Nagarajan, R. *Nanoparticles: synthesis, stabilization, passivation, and functionalization*. (American Chemical Society, 2008).
3. Yoon, H. Y. *et al.* Inorganic nanoparticles for image-guided therapy. *Bioconjug. Chem.* acs.bioconjchem.6b00512 (2016). doi:10.1021/acs.bioconjchem.6b00512
4. Ladj, R. *et al.* Individual inorganic nanoparticles: preparation{,} functionalization and in vitro biomedical diagnostic applications. *J. Mater. Chem. B* **1,** 1381–1396 (2013).
5. Sun, C., Lee, J. S. H. & Zhang, M. Magnetic nanoparticles in MR imaging and drug delivery. *Adv. Drug Deliv. Rev.* **60,** 1252–65 (2008).
6. Gupta, A. K. & Gupta, M. Synthesis and surface engineering of iron oxide nanoparticles for biomedical applications. *Biomaterials* **26,** 3995–4021 (2005).
7. Laurent, S. *et al.* Magnetic iron oxide nanoparticles: synthesis, stabilization, vectorization, physicochemical characterizations, and biological applications. *Chem. Rev.* **108,** 2064–110 (2008).
8. Ito, A., Shinkai, M., Honda, H. & Kobayashi, T. Medical application of functionalized magnetic nanoparticles. *J. Biosci. Bioeng.* **100,** 1–11 (2005).
9. Jadhav, S. A. & Bongiovanni, R. Synthesis and organic functionalization approaches for magnetite (Fe3O4) nanoparticles. *Advanced Materials Letters* **3,** 356–361 (2012).
10. Boyer, C., Whittaker, M. R., Bulmus, V., Liu, J. & Davis, T. P. The design and utility of polymer-stabilized iron-oxide nanoparticles for nanomedicine applications. *NPG Asia Mater.* **2,** 23–30 (2010).
11. Basuki, J. S. *et al.* A block copolymer-stabilized co-precipitation approach to magnetic iron oxide nanoparticles for potential use as MRI contrast agents. *Polym. Chem.* **5,** 2611–2620 (2014).
12. Barrow, M., Taylor, A., Murray, P., Rosseinsky, M. J. & Adams, D. J. Design considerations for the synthesis of polymer coated iron oxide nanoparticles for stem cell labelling and tracking using MRI. *Chem. Soc. Rev.* **44,** 6733–6748 (2015).
13. Lee, J. H. *et al.* All-in-One target-cell-specific magnetic nanoparticles for simultaneous molecular imaging and siRNA delivery. *Angew. Chemie - Int. Ed.* **48,** 4174–4179 (2009).
14. Medarova, Z., Pham, W., Farrar, C., Petkova, V. & Moore, A. In vivo imaging of siRNA delivery and silencing in tumors. *Nat. Med.* **13,** 372–7 (2007).
15. Amstad, E., Kohlbrecher, J., Müller, E. & Schweizer, T. Triggered Release from Liposomes through Magnetic Actuation of Iron Oxide Nanoparticle Containing Membranes. *Nano Lett.* 1664–1670 (2011).
16. Chandrasekharan, P. *et al.* Vitamin E (D-alpha-tocopheryl-co-poly(ethylene glycol) 1000 succinate) micelles-superparamagnetic iron oxide nanoparticles for enhanced thermotherapy and MRI. *Biomaterials* **32,** 5663–72 (2011).
17. Mahmoudi, M., Hofmann, H., Rothen-Rutishauser, B. & Petri-Fink, A. Assessing the in vitro and in vivo toxicity of superparamagnetic iron oxide nanoparticles. *Chem. Rev.* **112,** 2323–38 (2012).
18. Hanini, A. *et al.* Evaluation of iron oxide nanoparticle biocompatibility. *Int. J. Nanomedicine* **6,** 787–794 (2011).
19. Mahmoudi, M., Laurent, S., Shokrgozar, M. A. & Hosseinkhani, M. Toxicity Evaluations of

Superparamagnetic Iron Oxide Nanoparticles: Cell 'Vision' *versus* Physicochemical Properties of Nanoparticles. *ACS Nano* **5,** 7263–7276 (2011).
20. Dykman, L. & Khlebtsov, N. Gold nanoparticles in biomedical applications: recent advances and perspectives. *Chem. Soc. Rev.* **41,** 2256–2282 (2012).
21. Dreaden, E. C., Alkilany, A. M., Huang, X., Murphy, C. J. & El-Sayed, M. a. The golden age: gold nanoparticles for biomedicine. *Chem. Soc. Rev.* **41,** 2740 (2012).
22. Chen, A. & Chatterjee, S. Nanomaterials based electrochemical sensors for biomedical applications. *Chem. Soc. Rev.* **42,** 5425–38 (2013).
23. Wang, Y., Yan, B. & Chen, L. SERS Tags: Novel optical nanoprobes for bioanalysis. *Chem. Rev.* **113,** 1391–1428 (2013).
24. Chen, H., Shao, L., Li, Q. & Wang, J. Gold nanorods and their plasmonic properties. *Chem. Soc. Rev. Chem. Soc. Rev* **42,** 2679–2724 (2013).
25. Yeh, Y.-C., Creran, B. & Rotello, V. M. Gold nanoparticles: preparation, properties, and applications in bionanotechnology. *Nanoscale* **4,** 1871–80 (2012).
26. J. Turkevich, Stevenson, P. C. & Hillier, J. A study of the nucleation and growth processes in the synthesis of colloidal gold. *Discuss. Faraday Soc.* **11,** 55 (1951).
27. Turkevich, J., Stevenson, P. & Hillier, J. The formation of colloidal gold. *J. Phys. Chem.* **57,** 670 (1953).
28. Rohiman, A., Anshori, I., Surawijaya, A. & Idris, I. Study of colloidal gold synthesis using Turkevich method. *AIP Conf. Proc.* **1415,** 39–42 (2011).
29. Kimling, J. *et al.* Turkevich Method for Gold Nanoparticle Synthesis Revisited.pdf. *J. Phys. Chem. B* **110,** 15700–15707 (2006).
30. Brust, M., Walker, M., Bethell, D., Schiffrin, D. J. & Whyman, R. Synthesis of thiol-derivatised gold nanoparticles in a two-phase Liquid–Liquid system. *J. Am. Chem. Soc.* **7,** 801–802 (1994).
31. Ahmad, M. Z. *et al.* Nanometric gold in cancer nanotechnology: current status and future prospect. *J. Pharm. Pharmacol.* n/a-n/a (2013). doi:10.1111/jphp.12017
32. Yavuz, M. S. *et al.* Gold nanocages covered by smart polymers for controlled release with near-infrared light. *Nat. Mater.* **8,** 935–9 (2009).
33. Wei, Q. *et al.* Gyromagnetic Imaging : Dynamic Optical Contrast Using Gold Nanostars with Magnetic Cores. *J. Am. Chem. Soc.* **131,** 9728–9734 (2009).
34. Sapsford, K. E. *et al.* Functionalizing nanoparticles with biological molecules: developing chemistries that facilitate nanotechnology. *Chem. Rev.* **113,** 1904–2074 (2013).
35. Gormley, A. J., Malugin, A., Ray, A., Robinson, R. & Ghandehari, H. Biological evaluation of RGDfK-gold nanorod conjugates for prostate cancer treatment. *J. Drug Target.* **19,** 915–24 (2011).
36. Hoyle, C. E. & Bowman, C. N. Thiol-ene click chemistry. *Angew. Chem. Int. Ed. Engl.* **49,** 1540–73 (2010).
37. Han, J. C. & Han, G. Y. A procedure for quantitative determination of tris(2-carboxyethyl)phosphine, an odorless reducing agent more stable and effective than dithiothreitol. *Analytical biochemistry* **220,** 5–10 (1994).
38. Marjomäki, V. *et al.* Site-specific targeting of enterovirus capsid by functionalized monodisperse gold nanoclusters. *Proc. Natl. Acad. Sci. U.S.A.* **111,** 1277–81 (2014).
39. Lin, A. Y. *et al.* Gold Nanoparticle Delivery of Modified CpG Stimulates Macrophages and Inhibits Tumor Growth for Enhanced Immunotherapy. *PLoS One* **8,** (2013).
40. Almeida, J. P. M., Chen, A. L., Foster, A. & Drezek, R. In vivo biodistribution of nanoparticles. *Nanomedicine (Lond).* **6,** 815–35 (2011).
41. Khlebtsov, N. & Dykman, L. Biodistribution and toxicity of engineered gold nanoparticles: a review of in vitro and in vivo studies. *Chem. Soc. Rev.* **40,** 1647–1671 (2011).

42. Sadauskas, E. *et al.* Kupffer cells are central in the removal of nanoparticles from the organism. *Part. Fibre Toxicol.* **4,** 10 (2007).
43. Sonavane, G., Tomoda, K. & Makino, K. Biodistribution of colloidal gold nanoparticles after intravenous administration: Effect of particle size. *Colloids Surfaces B Biointerfaces* **66,** 274–280 (2008).
44. De Jong, W. H. *et al.* Particle size-dependent organ distribution of gold nanoparticles after intravenous administration. *Biomaterials* **29,** 1912–1919 (2008).
45. Longmire, M., Choyke, P. L. & Kobayashi, H. Clearance properties of nano-sized particles and molecules as imaging agents: considerations and caveats. *Nanomedicine* **3,** 703–717 (2008).
46. Hirn, S. *et al.* Particle size-dependent and surface charge-dependent biodistribution of gold nanoparticles after intravenous administration. *Eur. J. Pharm. Biopharm.* **77,** 407–416 (2011).
47. Sadauskas, E. *et al.* Protracted elimination of gold nanoparticles from mouse liver. *Nanomedicine Nanotechnology, Biol. Med.* **5,** 162–169 (2009).
48. Zhang, G. *et al.* Influence of anchoring ligands and particle size on the colloidal stability and in vivo biodistribution of polyethylene glycol-coated gold nanoparticles in tumor-xenografted mice. *Biomaterials* **30,** 1928–1936 (2009).
49. Alric, C. *et al.* The biodistribution of gold nanoparticles designed for renal clearance. *Nanoscale* **5,** 5930–9 (2013).
50. Deen, W., Lazzara, M. & Myers, B. Structural determinants of glomerular permselectivity. *Am J Physiol Ren. Physiol 281* **36,** F579–F596 (2001).
51. Zhou, C., Long, M., Qin, Y., Sun, X. & Zheng, J. Luminescent gold nanoparticles with efficient renal clearance. *Angew. Chemie - Int. Ed.* **50,** 3168–3172 (2011).
52. Pan, Y. *et al.* Gold nanoparticles of diameter 1.4 nm trigger necrosis by oxidative stress and mitochondrial damage. *Small* **5,** 2067–2076 (2009).
53. Hainfeld, J. F., Slatkin, D. N. & Smilowitz, H. M. The use of gold nanoparticles to enhance radiotherapy in mice. *Phys. Med. Biol.* **49,** N309–N315 (2004).
54. Zaki, A. Al *et al.* Gold-Loaded Polymeric Micelles for Computed Tomography-Guided Radiation Therapy Treatment. *ACS Nano* **8,** 104–112 (2014).
55. Gold, V. IUPAC Compendium of Chemical Terminology. *Isotopomer* 1670 (2014). doi:10.1351/goldbook.I03352
56. Huang, X., El-Sayed, I. H., Qian, W. & El-Sayed, M. a. Cancer cell imaging and photothermal therapy in the near-infrared region by using gold nanorods. *J. Am. Chem. Soc.* **128,** 2115–20 (2006).
57. Loo, C., Lowery, A., Halas, N., West, J. & Drezek, R. Immunotargeted nanoshells for integrated cancer imaging and therapy. *Nano Lett.* **5,** 709–11 (2005).
58. Kennedy, L. C. *et al.* A new era for cancer treatment: gold-nanoparticle-mediated thermal therapies. *Small* **7,** 169–83 (2011).
59. Bear, A. S. *et al.* Elimination of metastatic melanoma using gold nanoshell-enabled photothermal therapy and adoptive T cell transfer. *PLoS One* **8,** e69073 (2013).
60. El-Sayed, I. H., Huang, X. & El-Sayed, M. a. Selective laser photo-thermal therapy of epithelial carcinoma using anti-EGFR antibody conjugated gold nanoparticles. *Cancer Lett.* **239,** 129–35 (2006).
61. Jain, P. & El-Sayed, I. Au nanoparticles target cancer. *Nano Today* **2,** 18–29 (2007).
62. Hirsch, L. R. *et al.* Nanoshell-mediated near-infrared thermal therapy of tumors under magnetic resonance guidance. *Proc. Natl. Acad. Sci. U. S. A.* **100,** 13549–54 (2003).
63. Kennedy, L. C. *et al.* A new era for cancer treatment: gold-nanoparticle-mediated thermal therapies. *Small* **7,** 169–83 (2011).

64. Kim, J., Oh, J., Kang, H. W., Feldman, M. D. & Milner, T. E. Photothermal response of superparamagnetic iron oxide nanoparticles. *Lasers Surg. Med.* **40,** 415–421 (2008).
65. Chen, H. *et al.* Highly crystallized iron oxide nanoparticles as effective and biodegradable mediators for photothermal cancer therapy. *J. Mater. Chem. B* **2,** 757 (2014).
66. Henderson, T. A. & Morries, L. D. Near-infrared photonic energy penetration: can infrared phototherapy effectively reach the human brain? *Neuropsychiatr. Dis. Treat.* **11,** 2191–208 (2015).
67. Yoon S. Lee. in *Self-Assembly and Nanotechnology* 1–19 (John Wiley & Sons, Inc., 2003). doi:10.1002/9780470292525.ch1
68. Lee, Y. S. Control of the Structures of Self-Assembled Aggregates. *Self-Assembly Nanotechnol. Syst.* 111–140 (2011). doi:10.1002/9781118103708.ch5
69. Lee, Y. S. in *Self-Assembly and Nanotechnology Systems* 93–110 (John Wiley & Sons, Inc., 2011). doi:10.1002/9781118103708.ch4
70. Lee, Y. S. in *Self-Assembly and Nanotechnology Systems* 191–256 (John Wiley & Sons, Inc., 2011). doi:10.1002/9781118103708.ch9
71. Gröschel, A. H. & Mueller, A. H. E. Self-Assembly Concepts for Multicompartment Nanostructures. *Nanoscale* 11841–11876 (2015). doi:10.1039/C5NR02448J
72. Du, J. & O'Reilly, R. K. Anisotropic particles with patchy, multicompartment and Janus architectures: preparation and application. *Chem. Soc. Rev.* **40,** 2402–2416 (2011).
73. Lattuada, M. & Hatton, T. A. Synthesis, properties and applications of Janus nanoparticles. *Nano Today* **6,** 286–308 (2011).
74. Walther, A. & Müller, A. H. E. Janus particles: synthesis, self-assembly, physical properties, and applications. *Chem. Rev.* **113,** 5194–261 (2013).
75. Wu, Z., Lin, X., Si, T. & He, Q. Recent Progress on Bioinspired Self-Propelled Micro/Nanomotors via Controlled Molecular Self-Assembly. *Small* **12,** 3080–93 (2016).
76. Gao, W., Pei, A., Feng, X., Hennessy, C. & Wang, J. Organized self-assembly of janus micromotors with hydrophobic hemispheres. *J. Am. Chem. Soc.* **135,** 998–1001 (2013).
77. Kim, D.-H. *et al.* Biofunctionalized magnetic-vortex microdiscs for targeted cancer-cell destruction. *Nat. Mater.* **9,** 165–71 (2010).
78. De Gregorio, E. & Rappuoli, R. From empiricism to rational design: a personal perspective of the evolution of vaccine development. *Nat. Rev. Immunol.* **14,** 505–514 (2014).
79. Plotkin, S. A. & Plotkin, S. L. The development of vaccines: how the past led to the future. *Nat. Rev. Microbiol.* **9,** 889–893 (2011).
80. Pasquale, A., Preiss, S., Silva, F. & Garçon, N. Vaccine Adjuvants: from 1920 to 2015 and Beyond. *Vaccines* **3,** 320–343 (2015).
81. Bachmann, M. F. & Jennings, G. T. Vaccine delivery: a matter of size, geometry, kinetics and molecular patterns. *Nat. Rev. Immunol.* **10,** 787–96 (2010).
82. Reed, S. G., Orr, M. T. & Fox, C. B. Key roles of adjuvants in modern vaccines. *Nat. Med.* **19,** 1597–1608 (2013).
83. Fifis, T. *et al.* Size-Dependent Immunogenicity: Therapeutic and Protective Properties of Nano-Vaccines against Tumors. *J. Immunol.* **173,** 3148–3154 (2004).
84. Park, Y.-M. *et al.* Nanoparticle-based vaccine delivery for cancer immunotherapy. *Immune Netw.* **13,** 177–83 (2013).
85. Irvine, D. J., Swartz, M. A. & Szeto, G. L. Engineering synthetic vaccines using cues from natural immunity. *Nat. Mater.* **12,** 978–990 (2013).
86. Gamvrellis, A. *et al.* Vaccines that facilitate antigen entry into dendritic cells. *Immunol. Cell Biol.* **82,** 506–516 (2004).
87. Rosalia, R. A. *et al.* CD40-targeted dendritic cell delivery of PLGA-nanoparticle vaccines

induce potent anti-tumor responses. *Biomaterials* **40,** 88–97 (2015).
88. Palucka, K. & Banchereau, J. Cancer immunotherapy via dendritic cells. *Nat. Rev. Cancer* **12,** 265–277 (2012).
89. Mody, N., Dubey, S., Sharma, R., Agrawal, U. & Vyas, S. P. Dendritic cell-based vaccine research against cancer. *Expert Rev. Clin. Immunol.* **11,** 213–232 (2015).
90. Sabado, R. L. & Bhardwaj, N. Dendritic-cell vaccines on the move. *Nature* **519,** 300–301 (2015).
91. Krishnamachari, Y., Geary, S. M., Lemke, C. D. & Salem, A. K. Nanoparticle delivery systems in cancer vaccines. *Pharm. Res.* **28,** 215–236 (2011).
92. van der Weijden, J., Paulis, L. E., Verdoes, M., van Hest, J. C. M. & Figdor, C. G. The right touch: design of artificial antigen-presenting cells to stimulate the immune system. *Chem. Sci.* **5,** 3355–3367 (2014).
93. Manolova, V. *et al.* Nanoparticles target distinct dendritic cell populations according to their size. *Eur. J. Immunol.* **38,** 1404–1413 (2008).
94. Brode, S. & MacAry, P. A. Cross-presentation: Dendritic cells and macrophages bite off more than they can chew! *Immunology* **112,** 345–351 (2004).
95. Chen, H. *et al.* The promotion of type 1 T helper cell responses to cationic polymers in vivo via toll-like receptor-4 mediated IL-12 secretion. *Biomaterials* **31,** 8172–8180 (2010).
96. Agarwal, R. *et al.* Mammalian cells preferentially internalize hydrogel nanodiscs over nanorods and use shape-specific uptake mechanisms. *Proc. Natl. Acad. Sci.* **110,** 17247–17252 (2013).
97. Kumar, S., Anselmo, A. C., Banerjee, A., Zakrewsky, M. & Mitragotri, S. Shape and size-dependent immune response to antigen-carrying nanoparticles. *J. Control. Release* **220,** 141–148 (2015).
98. Huang, W. C. *et al.* Engineering chimeric receptors to investigate the size- and rigidity-dependent interaction of pegylated nanoparticles with cells. *ACS Nano* **10,** 648–662 (2016).
99. Bullock, T. N. J., Colella, T. A. & Engelhard, V. H. The Density of Peptides Displayed by Dendritic Cells Affects Immune Responses to Human Tyrosinase and gp100 in HLA-A2 Transgenic Mice. *J. Immunol.* **164,** 2354–2361 (2000).
100. Bullock, T. N. J., Mullins, D. W. & Engelhard, V. H. Antigen density presented by dendritic cells in vivo differentially affects the number and avidity of primary, memory, and recall CD8+ T cells. *J. Immunol.* **170,** 1822–1829 (2003).
101. Henrickson, S. E. *et al.* T cell sensing of antigen dose governs interactive behavior with dendritic cells and sets a threshold for T cell activation. *Nat. Immunol.* **9,** 282–291 (2008).
102. Cheng, W. The Density Code for the Development of a Vaccine? *J. Pharm. Sci.* **105,** 3223–3232 (2016).
103. Caudle, A. S., Yang, W. T., Mittendorf, E. A. & Kuerer, H. M. The impact of nanoparticle ligand density on dendritic-cell targeted vaccines. *Biomaterials* **32,** 3094–3105 (2011).
104. Lin, A. Y. *et al.* High-density sub-100-nm peptide-gold nanoparticle complexes improve vaccine presentation by dendritic cells in vitro. *Nanoscale Res. Lett.* **8,** 72 (2013).
105. V, P. Homogeneous Conjugation of Peptides onto Gold Nanoparticles Enhances Macrophage Response. *ACS Nano* **3,** 1335 (2009).
106. Cho, N.-H. *et al.* A multifunctional core-shell nanoparticle for dendritic cell-based cancer immunotherapy. *Nat. Nanotechnol.* **6,** 675–82 (2011).
107. Sungsuwan, S., Yin, Z. & Huang, X. Lipopeptide-Coated Iron Oxide Nanoparticles as Potential Glycoconjugate-Based Synthetic Anticancer Vaccines. *ACS Appl. Mater. Interfaces* **7,** 17535–17544 (2015).
108. Kranz, L. M. *et al.* Systemic RNA delivery to dendritic cells exploits antiviral defence for

cancer immunotherapy. *Nature* **534,** 396–401 (2016).
109. Varypataki, E. M., van der Maaden, K., Bouwstra, J., Ossendorp, F. & Jiskoot, W. Cationic liposomes loaded with a synthetic long peptide and poly(I:C): a defined adjuvanted vaccine for induction of antigen-specific T cell cytotoxicity. *AAPS J.* **17,** 216–26 (2015).
110. Chen, W. & Huang, L. Induction of cytotoxic T-lymphocytes and antitumor activity by a liposomal lipopeptide vaccine. *Mol. Pharm.* **5,** 464–471 (2008).
111. Kuai, R., Ochyl, L. J., Bahjat, K. S., Schwendeman, A. & Moon, J. J. Designer vaccine nanodiscs for personalized cancer immunotherapy. *Nat. Mater.* **1,** (2016).
112. Hamdy, S., Haddadi, A., Hung, R. W. & Lavasanifar, A. Targeting dendritic cells with nano-particulate PLGA cancer vaccine formulations. *Adv. Drug Deliv. Rev.* **63,** 943–955 (2011).
113. Zeltins, A. Construction and characterization of virus-like particles: A review. *Mol. Biotechnol.* **53,** 92–107 (2013).
114. Chackerian, B. Virus-like particles: flexible platforms for vaccine development. *Expert Rev. Vaccines* **6,** 381–390 (2007).
115. Villa, L. L. *et al.* High sustained efficacy of a prophylactic quadrivalent human papillomavirus types 6/11/16/18 L1 virus-like particle vaccine through 5 years of follow-up. *Br. J. Cancer* **95,** 1459–1466 (2006).
116. Kirnbauer, R., Booyt, F., Chengt, N., Lowy, D. R. & Schiller, J. T. Papillomavirus Li major capsid protein self-assembles into virus-like particles that are highly immunogenic. *Med. Sci.* **89,** 12180–12184 (1992).

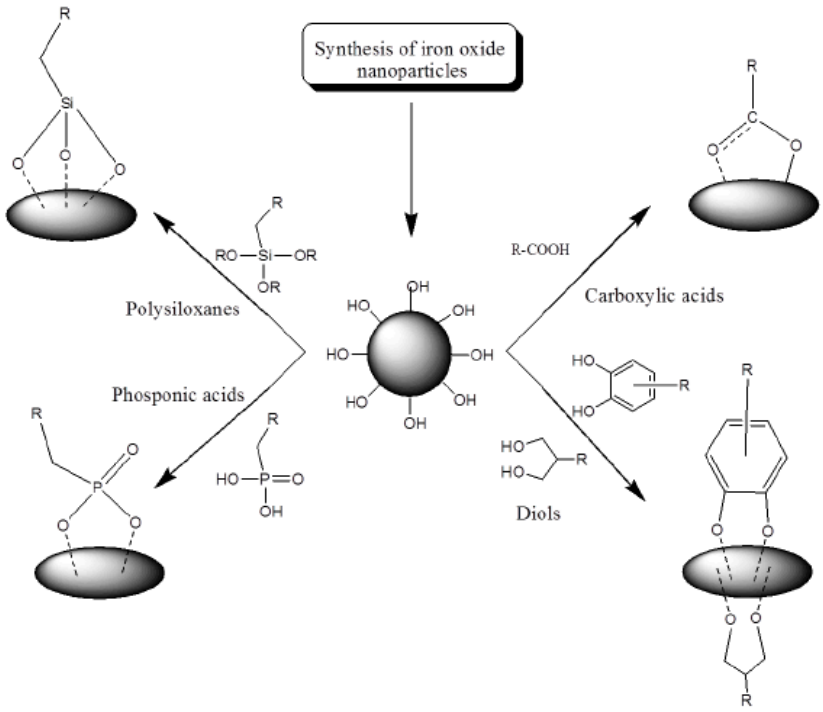

Figure 1.1 Surface functionalization of SPION. From ref.9

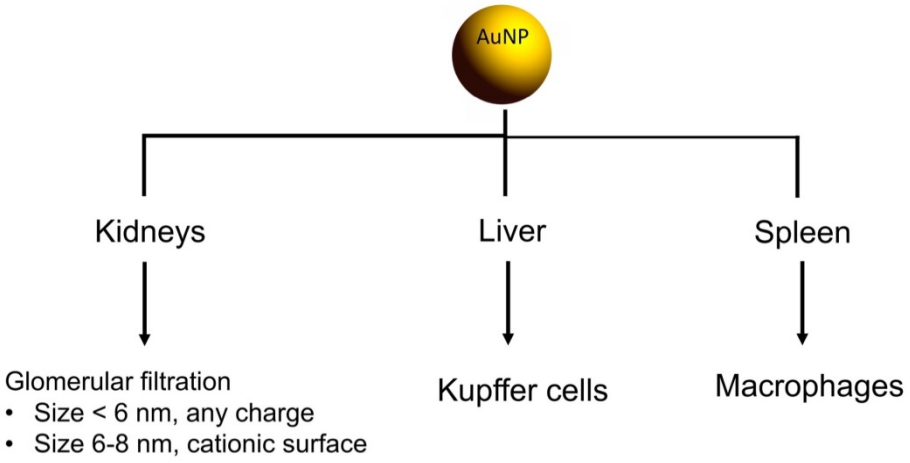

Figure 1.2. The diagram shows the excretion and elimination of AuNP

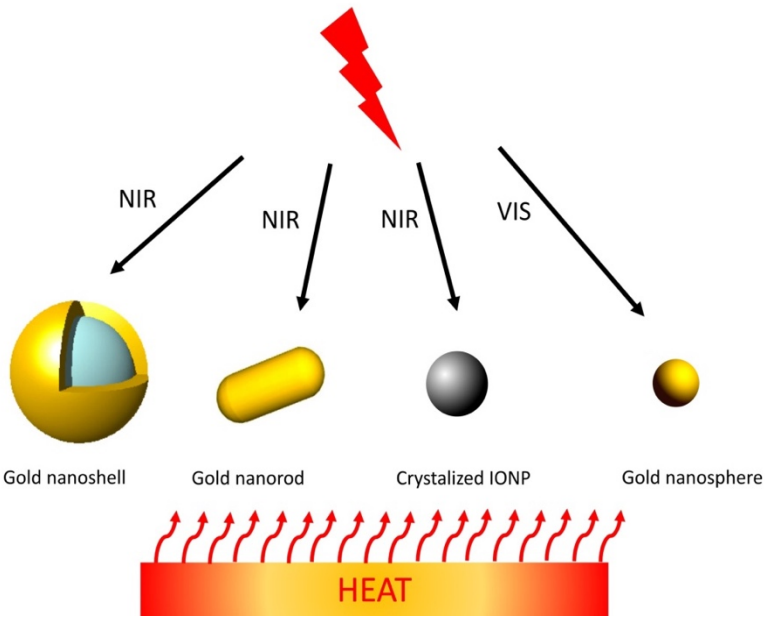

Figure 1.3. General nanoparticles that have photothermal effect after light irradiation at appropriate wavelength

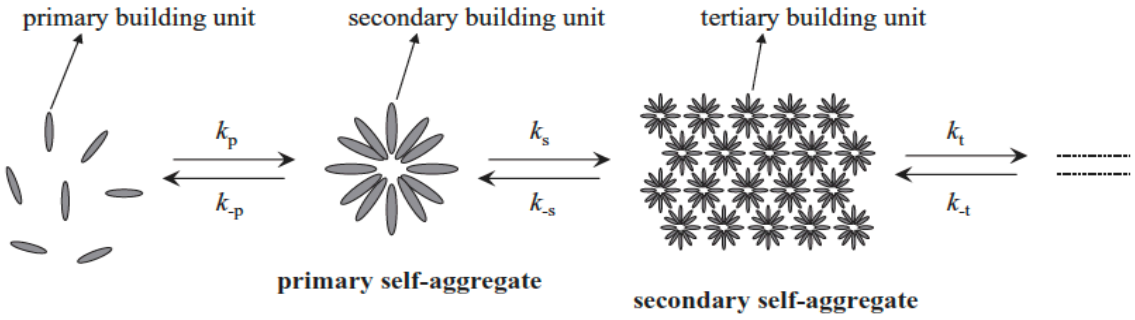

Figure 1.4. General scheme for self-assembly. (from ref 67)

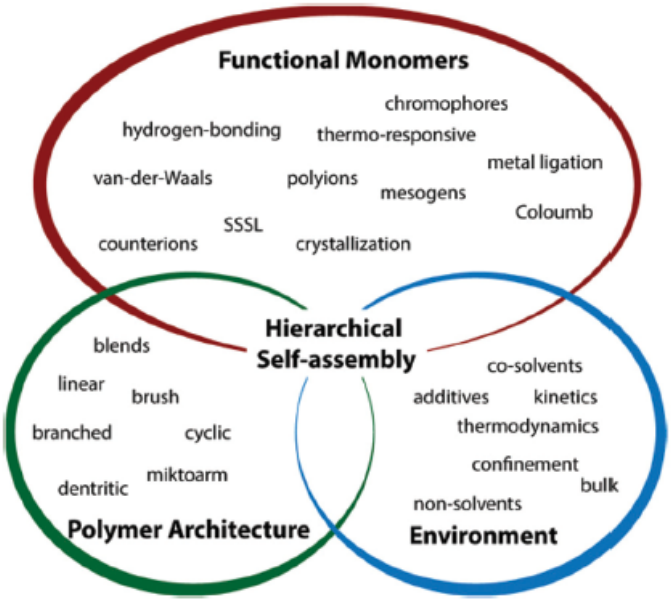

Figure 1.5. Factors influence hierarchical structure formations (from ref 71).

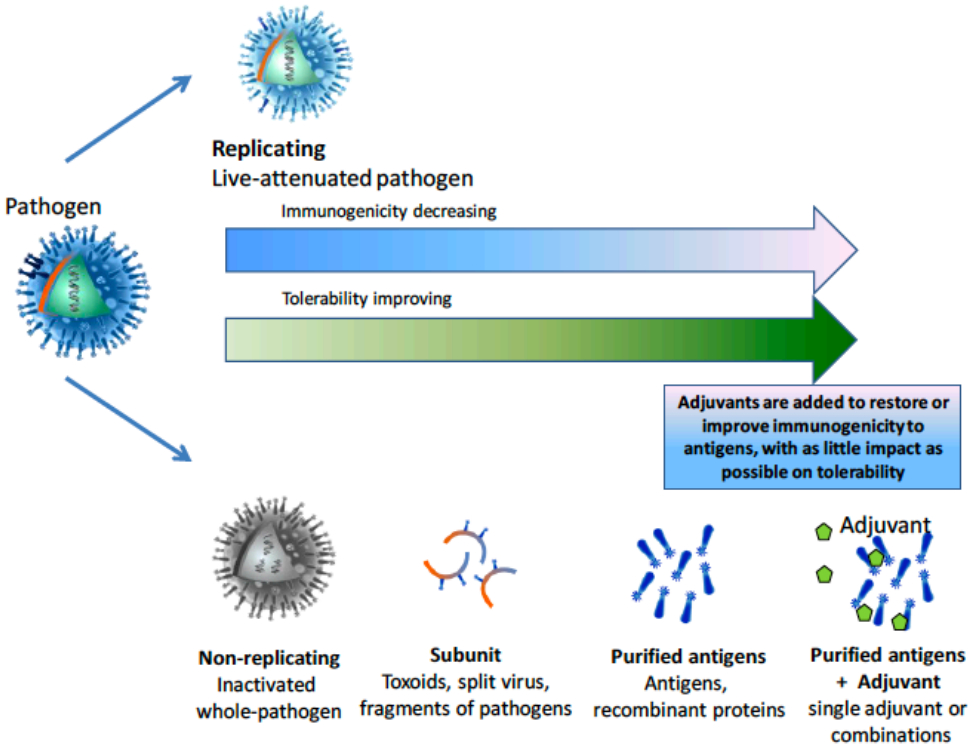

Figure 1.6. Types of vaccines, immunogenicity, and safety (ref 80)

CHAPTER 2

MULTI-BUILDING BLOCK JANUS SYNTHESIZED BY SEED-MEDIATED SELF-ASSEMBLY FOR ENHANCED PHOTOTHERMAL EFFECTS AND COLORED BROWNIAN MOTION IN AN OPTICAL TRAP

2.1 Abstract

The asymmetrical features and unique properties of multi-building block Janus nanostructures provide superior functions for biomedical applications. However, their production process is very challenging. This problem has hampered the progress of Janus nanostructure research and the exploration of their applications. In this study, we generated an asymmetrical multi-building block gold/iron oxide Janus nanostructure (JNS) to enhance photothermal effects and display colored Brownian motion in an optical trap. JNS are formed by seed-mediated self-assembly of nanoparticle-loaded thermo-cleavable micelles (NP-TCM), where the hydrophobic backbones of the polymer are disrupted at high temperatures, resulting in secondary self-assembly and structural rearrangement. The JNS significantly enhanced photothermal effects compared to their homogeneous counterpart after near infrared (NIR) light irradiation. The asymmetrical distribution of gold and iron oxide within JNS also generated uneven thermophoretic force to display active colored Brownian rotational motion in a single-beam gradient optical trap. These properties indicate that the asymmetrical JNS could be employed as

a strong photothermal therapy (PTT) mediator, and a fuel-free nanoscale Janus motor under NIR light

2.2 Introduction

Janus, anisotropic, or patchy particles have long been in an interest of various applications. Their asymmetrical structures make them appealing for diverse functions, such as surface-reducing agents, electronic devices, catalysts, molecular imaging, diagnostics, and drug delivery systems[1–4]. Recently, multi-building block Janus, composed of multiple nanoparticles arranged in an asymmetrical pattern in a single entity, have been used in imaging, theranostics, and cargo deliveries[5–7]. These complex Janus structures provide superior properties and have more effective responses to external stimuli compared to a single-domain Janus particle of the same size. The multi-building block Janus benefits from the high surface-to-volume ratio[8] and strong interaction among metal nanoparticle building blocks[9]. Despite the exceptional qualities of the multi-building block Janus particles, the approach and control process to produce these complex structures on a nano scale are very challenging[10]. They require a high degree of control to direct the aggregate process. Conventional approaches for Janus nanoparticle (JP) production, such as surface masking and phase separation, mostly yield single domain JPs on a micron scale, which have limited use for biomedical applications[11–14]. Those strategies are not suitable for fabricating nano-scale multi-building block JPs. The most promising strategy for multi-building block JP formation on a nanometer scale is to employ bottom up self-assembly to control the location of

nanoparticle distribution in block copolymers. Previous research has suggested that many factors significantly contribute to the location of nanoparticles inside micelles, such as affinities between nanoparticle-coating ligands and polymeric micelles[15], relative lengths of polymer and nanoparticle size[16,17], lengths of surface coating of nanoparticles[16], glass transition temperature of the polymer[18], and solvent effects[19,20]. These significant discoveries allow researchers to control the location of nanoparticles and form complex structures such as nanowires, nanosheets, cylinders and vesicles[21]. However, not much research has focused on utilizing controlled nanoparticle location and self-assembly to fabricate a nano-scale asymmetrical multi-building block Janus structure composed of two different inorganic nanoparticles.

Gold (AuNP) and iron oxide (IONP) nanoparticles are the most intensively studied inorganic nanoparticles. They show good safety profiles, biocompatibility, biodegradability, and efficacy in cancer theranostics[22,23]. Most importantly, AuNPs and IONPs have different photothermal conversion efficiencies. The temperature created by AuNP and IONP are different. As a result, the gold/iron oxide JNS experiences a thermophoretic force that causes the particle to rotate. Jiang et al. has shown that a micron-sized gold/silica Janus can generate a spin motion under 1064 nm laser irradiation due to self-thermophoresis of the microparticles, which can be visualized under microscope[24]. However, it is challenging to generate active motion in nano-sized Janus structures, and even more difficult to visualize that active rotational motion. While optical trapping of Janus Nanostructures (JNS) has been previously demonstrated, those experiments were not designed to detect the active

motion[25].Therefore, we intend to create an active spin motion from a nanoscale Janus, and use a modified optical trapping technique to detect the unique motion. An asymmetrical Janus structure has the potential to generate active motion for electrical and biomedical applications[24].

In this article, we report a novel fabrication of multi-building block Janus structures composed of two different inorganic nanoparticles, AuNP and IONP, using thermo-cleavable amphiphilic diblock copolymer to control the nanoparticle distribution and self-assembly of nanoparticles loaded in the thermo-cleavable micelles. To the best of our knowledge, this is, for the first time, using thermo-cleavable polymer to form asymmetrical Janus structures. The thermo-cleavable amphiphilic diblock copolymer, in which the hydrophobic backbone could be cleaved apart at high temperatures via retro Diels-Alder reaction, provides an unstable condition at high temperatures, which encourages AuNPs and IONPs to self-assemble into multi-building block JNS by micelle collision and fusion. We found that our JNS expressed strong photothermal efficiency after near infrared (NIR) light irradiation, much stronger than that of their homogeneous counterparts, due to the strong collective effect of their AuNPs. The NIR laser light irradiation also created a temperature imbalance between the two different sides of the JNS, which caused the particles to rotate, resulting in distinct frequencies of colored Brownian motion under an optical trap. These unique characteristic suggest that the Au/IONP JNS could potentially be employed as for both photothermal therapy and nanoscale Janus motors at the same time [26]. This is highly significant for the future research *in vivo*, where the penetration of nanoparticles in a tumor mass is limited at only the shallow layers of the tumor around blood vessels. Our JNS can possibly

overcome this problem as they can eradicate the cancer cells near the blood vessels and also simultaneously penetrate to the deeper layers of the tumor mass by self-propelled motor and mechanical sheer force[27–29].

2.3 Results and Discussion

2.3.1 Thermo-cleavable polymer synthesis

The JNS were fabricated via self-assembly of nanoparticles loaded into thermo-cleavable polymeric micelles. We first synthesized the thermo-cleavable hydrophobic backbone via Diels-Alder reaction at 70 °C[30,31]. Molecular weight of the hydrophobic backbone is 5,090 Da measured by GPC and then poly ethylene oxide (PEO) molecular weight 5,000 Da was added and reacted with the maleimide functional group of the hydrophobic backbone via Michael addition. The final amphiphilic diblock thermo-cleavable polymer (Da-*b*-PEO) has the molecular weight of 9,800 Da characterized by GPC and ^{1}H NMR (Figure 1a, S1, S2 and S3). This polymer acts not only as a key component to control hydrophobic interaction between nanoparticles and the polymer itself, but also mediates the micelle fusion. The cycloadducts in the hydrophobic backbones can be cleaved apart at or above 90 °C via retro Diels-Alder reaction[32], as proven by ^{1}H NMR (Figure 1b and c). The data suggest that 84% of the formed cycloadducts were cleaved after the polymer was treated at 100 °C for an hour (Figure 1d). The retro Diels-Alder causes hydrophobic backbone shortening and hydrophobic-hydrophilic imbalance, which critically affects the thermodynamic stability and triggers self-assembly of the thermo-cleavable micelles (TCM).

2.3.2 Multi-building block gold/iron oxide Janus nanostructure (JNS) formation

Gold and iron oxide nanoparticles were used to generate Janus nanostructures (JNS). Oleic acid-capped iron oxide nanoparticles (15 nm) (IONPs) and dodecanethiol capped gold nanoparticles (5 nm) (AuNPs) were encapsulated separately in the polymer to make IONP-loaded thermo-cleavable micelles (FeTCM) and AuNP-loaded thermo-cleavable micelles (AuTCM) respectively. Transmission electron microscopy (TEM) images clearly showed that nanoparticles aggregated at the center of the micelles' hydrophobic domain (Figure 2a, 2b) due to strong interparticle Van Der Waals attractions. TEM data suggest that FeTCMs and AuTCMs have average core diameters of 39.6 nm and 56.6 nm respectively (Figure S4). The hydrodynamic diameters of these two micelles are 78.82 nm and 94.88 nm, which are larger than the core diameters measured by TEM because of the interaction between polymer and the aqueous media (Table S1). Next, the excess molar concentrations of AuTCM were mixed with FeTCM, subsequently mixed together with the free thermo-cleavable micelle (TCM) seeds. This was followed by heat treatment (94 °C) to generate asymmetrical Au/IONP JNS. The excess molar concentration of AuTCM was used to ensure that all FeTCMs were fused with AuTCMs. This completed solution was purified by a magnetic separator to remove the unreacted AuTCMs. The amount of AuNPs and IONPs in JNS could be controlled by the concentration ratios between AuTCMs and FeTCMs (Figure S5). Percent yield of JNS is 97.16% calculated from the feeding amount of Fe in FeTCM. Transmission electron microcopy (TEM) (Figure 2c, d, and S6a) and scanning transmission electron microscope high angle annular dark-field (STEM-HAADF) (Figure 2e, and S6b) images illustrate that AuNPs and IONPs are combined together in a new single entity with a

well-defined asymmetrical nanostructure. The average core diameter of the JNS measured by TEM is 86.5 nm (Figure S4) and hydrodynamic diameter measured by dynamic light scattering (DLS) is 100.3 nm. It is important to note that JNS formed by the self-assembly approach have a relatively small size, compared to Janus particles made by other conventional methods, which mostly yield particles in micron-scale single domains[33]. We performed X-ray energy dispersive spectroscopy (XEDS) element mapping to confirm that the JNS are composed of multiple AuNPs and IONPs in an asymmetrical pattern (Figure 2f). The formed JNS are stable over a period of 6 months after being stored at 4 °C. Dynamic light scattering data indicate no large aggregation in the solution (Figure S7). To prove that the thermo-cleavable polymer is a critical factor in the formation of our JNS, we used Polystyrene-*b*-polyethylene oxide (PS-*b*-PEO, Mw 10,300 Da) as a control for non-thermo-cleavable micelles (non-TCM) to encapsulate 15 nm IONPs and 5 nm AuNPs separately. This polymer cannot trigger self-assembly to form JNS after adding PS-*b*-PEO seeds at high temperature. These two types of nanoparticle-loaded micelles remained separate (Figure S8). We further ruled out the possibility that different capping ligands of AuNPs and IONPs cause a non-specific asymmetrical structure inside of TCM in an independent manner of polymer properties and self-assembly process. First, we mixed AuNPs and IONPs together homogeneously, then loaded them into the thermo-cleavable polymer to form micelles. TEM, STEM-HAADF imaging, and XEDS element mapping show that no well-organized asymmetrical JNS formation occurred (Figure 2g, h, and i). Under these conditions, AuNPs and IONPs mixed together in micelles randomly, forming a homogeneous

gold/iron oxide micelle (GMC) without any specific pattern. These data suggest that the thermo-cleavable polymer is critical for the self-assembly and self-reorganization processes that form our asymmetrical JNS.

2.3.3 Ball-like and patchy secondary nanostructure formation

We further studied seed-mediated self-assembly by following similar procedures to those for JNS formation, but using only one species of metal nanoparticles, either iron oxide or gold, mixed with the TCM seeds. TEM images clearly show the self-assembly process forming iron oxide ball-like nanostructures (FeBL) with diameter *ca.* 74.1 nm (Figure 3a and S4). This transformed structure was also confirmed by STEM-HAADF (Figure 3b and c). The images and density profiles of FeBL (Figure 3d) clearly indicate that the electron density was higher at the edges and lower inside the cores because nanoparticles aligned at the interface between hydrophilic PEG and hydrophobic residues after self-assembly. Notably, the self-assembly and transformation of nanoparticle-loaded TCM occurs regardless of nanoparticle type. We observed that self-assembly and transformation also took place with AuTCM. TEM and STEM-HAADF images clearly show gold patchy nanostructures (AuPS) (Figure 3e, f, and g). The density profile also confirmed an internal void volume of AuPS with a larger diameter than FeBL, 281.0 nm (Figure 3h). These data suggest that the self-assembly and self-reorganization process has transformed cluster nanoparticle micelles into secondary nanostructures. It is important to note that we did not observe self-reorganization and

transformation using the IONP-loaded in PS-*b*-PEO micelles with the non thermo-cleavable polymer (PS-*b*-PEO) seed (Figure S9).

2.3.4 Seed-mediated self-assembly process

We further investigated the mechanism of JNS and secondary structure formation. It is clear that self-assembly and transformation are driven by thermodynamic force. Luo and Eisenberg previously demonstrated that an increased amount of an aqueous phase in micelle system could induce thermodynamic instability, leading to micelle fusion. Smaller micelles fused together and formed larger micelles in order to mitigate their interfacial energy penalty[34,35]. Nevertheless, micelle fusion is quite unlikely in the case of nanoparticle-loaded micelles. The fusion of micelles is highly dependent on the polymer's properties and the nanoparticle diameters[36,37]. These NP-TCMs are stable, because the hydrophobic nanoparticles have a strong hydrophobic interaction within the hydrophobic polymer backbone. They are very rigid and less flexible, which makes micelle fusion and self-assembly of these NP-TCMs unusual. The hydrophobic attraction between the polymer backbone itself and the nanoparticles needs to be diminished in order to create an unstable state and to initiate the self-assembly process for micelle fusion of these FeTCMs and AuTCMs. We examined the mechanism of nanoparticle self-assembly by using only one species of metal nanoparticles and the free TCM seeds to reduce complexity. A series of TEM images confirms that AuTCM fused together until they were stable, then underwent phase separation and structural rearrangement. Samples for TEM were taken at the beginning of heat treatment (Figure

4a) and two hours after the heat treatment began (Figure 4b-e). When the mixture of NP-TCMs and free TCM seeds in aqueous media was exposed to the high temperature (94 °C), the hydrophobic backbones in all micelle species subsequently cleaved apart via retro Diels-Alder reaction, resulting in a reduction of the hydrophobic attraction between the backbone and nanoparticles. At this stage, NP-TCMs become unstable and relatively flexible. As a consequence, these unstable NP-TCMs fused with free TCM seeds in the aqueous media. While one NP-TCM collides with the seed, a second NP-TCM can also fuse with the same seed from the opposite side (Figure 4f). The free TCM not only acts as a seed to mediate the self-assembly, but also enhances a depletion force between two NP-TCMs[38,39]. This leads to structural transformation and self-assembly, forming the JNS. If only one species of NP-TCM (either AuTCMs or FeTCMs) is mixed with free TCM seeds in the system, ball-like or patchy nanostructures will be formed instead of JNS. Although the self-assembly process is challenging to control, we were able to regulate JNS formation by varying the ratio between AuNPs and IONPs. In contrast, the system without free TCM seeds failed to transform into secondary nanostructures at a high temperature. It was observed that the hydrophobic nanoparticles were released into the aqueous media, where they precipitated (Figure S10). Without free TCM seeds, there is neither a template for NP-TCMs to anchor onto nor a depletant to attract NP-TCMs; consequently, the fusion process is not possible.

The hydrophobic chain's changes in length under high temperature conditions are critical for JNS formation via the self-assembly process. It has been reported that the relation between lengths of polymeric micelles and nanoparticle diameters is a significant factor for controlling the location of nanoparticles inside micelles[16,17]. In

general, the energy penalty increases with the increasing ratio between nanoparticle size and the coil dimension of the polymer. Since the nanoparticles' radius of gyration is larger than the polymer's radius of gyration after backbone cleavage, the nanoparticles are expelled from the matrix, and large-scale phase separation occurs[40–42].

2.3.5 Janus nanostructure enhances photothermal effect

We further explored how our multi-building block Janus nanostructures interact with photothermal effect. Intriguingly, Au/IONP JNS significantly enhance temperatures when undergoing 885 nm NIR laser light irradiation at low laser power, 0.45W, with low concentrations of iron (40 μg/ml) and gold (170 μg/ml). Upon 10 minutes of NIR light irradiation, JNS gradually increased the temperature by 20.9 °C from the initial temperature in the cell culture media, while other controls, such as their homogeneous gold-iron oxide micelle counterparts (GMC), gold cluster micelles (AuTCM), iron oxide cluster micelles (FeTCM), a solution mixture of gold micelle and iron oxide cluster micelles, and cell culture media alone, increased only 15.0°C, 12.7°C, 7.3°C, 13.4°C, and 6.1°C from the initial temperature respectively (Figure 5a). Concentrations of gold and/or iron in all samples were fixed to the same or close to their concentration in the JNS. In addition, we further tested the enhanced photothermal effect on cancer cell. We monitored cell viability using an Alamar Blue assay when triple negative breast cancer cells (SUM159 cells) were treated with JNS under 885 nm NIR laser light. The high temperature created by the JNS resulted in lower cell viability compared to other treatments and the media control group. The cell viability of the group treated with JNS

under NIR laser light irradiation was 62.76%, while treatment using only the JNS, without NIR laser light irradiation, displayed no toxicity, with cell viability of 92.74% (Figure 5b).

In order to induce cell death by photothermal therapy (PTT), the temperature must be higher than 41°C to unfold proteins and trigger cell death signaling[43,44]. Therefore, good photothermal contrast agents with high photo-conversion efficiency are necessary. These agents must be able to significantly increase the temperature of the surrounding environment under low NIR laser power [45,46]. This is very important for ideal *in vivo* PTT, since low laser power has a minimal effect on surrounding normal tissues but effectively kills the cancer cells. It is noteworthy that the surface of JNS are covered by hydrophilic poly ethylene oxide (PEO) polymer. Though the hydrophobic backbone cleavage, the PEO remains intact. This makes JNS become stealthy and prevents protein absorption on the surface of JNS resulting in the reduction of phagocytosis by macrophages *in vivo*. Notably, our JNS demonstrate high photothermal efficiency at low laser power compared to their homogeneous counterparts. JNS clearly demonstrate overall higher absorption from 400 -900 nm (Figure S11). JNS may have “collective effects” by presence of multiple AuNPs in close proximity for higher PTT as described in literature[47]. Specifically, there are two mechanisms of interactions between AuNPs for the heating process: (1) accumulative effect of AuNP confined in JNS. The accumulative effect in AuNPs has been reported by Gorotov, et al (Nanoscale Res Lett, 2006) resulting in the strong temperature enhancement[48]. This effect stems from the addition of heat fluxes of multiple AuNPs. Our JNS show absorption at λ_{max} 1.61-fold

stronger than the gold-iron oxide homogeneous micelles counterparts (GMC) at the same concentration of Au and Fe. (2). The Coulomb effect is generated from the interaction among AuNPs in the JNS, which is also supported by literature reported by Zhang et al (Optic express, 2012)[49]. As a result, we observed a red shift from 504 nm to 520 nm of JNS compared to GMC. The insertion of IONPs between AuNPs in GMC hinders the accumulative and the Coulomb effect of AuNPs. Therefore, GMC could not fully take advantage of the collective effect. These data suggest that the structural arrangement of nanoparticles plays a crucial role in photothermal effect of secondary structures.

2.3.6 Janus nanostructures display colored Brownian motions under a single-beam gradient optical trap

Since our JNS's structure is asymmetrical, with AuNPs on one side and IONPs the other, the two sides have different photothermal efficiencies as well[22,23]. The absorption of laser light by AuNPs and IONPs on the surface of the JNS creates an uneven temperature gradient. Therefore, the JNS experiences a thermophoretic force that causes the structure to rotate (Figure 6a). To validate this behavior and quantitate the rotation frequency, we employed an optical trap to monitor individual JNS for this active rotational motion at the focus of a NIR laser (λ = 830 nm). Incorporating back-focal-plane interferometry (BFPI), this technique permits ultra-sensitive tracking and characterization of trapped sub-micron particles as recently applied to HIV-1 virions in culture media[50].

Power spectra from individually trapped particles are analyzed such that the laser alone is used as a baseline control (Figure 6b). Our data reveals that optically trapped JNS particles (N = 209) show a distinct peak at 0.5-3 kHz in their power spectra (Figure 6c and d). The presence of these peaks, i.e., apparent 'colors' in the thermal noise[51], is in sharp contrast to the power spectra displayed by homogeneous polystyrene or silica nanoparticles when they were trapped under identical conditions[52]. As a consequence, a typical Lorentzian fitting for these power spectra yielded bad fits, as indicated by the systematic deviations between the power spectra and the best fitted curves overlaid on the spectra. As a matter of fact, these peaks are absent in all symmetric nanostructure controls including AuTCMs (N = 50) (Figure 6e) and FeTCMs (N = 75) (Figure 6f), respectively. For these power spectra, the Lorentzian fitting provides an adequate description for the data over the entire frequency range that we have investigated (1- 30 kHz). Because these power spectra were recorded in the plane that is perpendicular to the laser beam axis (z-axis in Figure 6a), the presence of the peaks along both x- and y-axis in this plane indicate that a population of JNS displays periodic rotational motions in the focal plane at a frequency between 0.5-3 kHz, which deviate from the typical Brownian motions, but consistent with the rotation of these particles with a major frequency between 0.5-3 kHz as driven by the local temperature gradient. The colors of thermal noise in Brownian motions has been demonstrated previously for microscopic particles under strong trapping conditions[53], which results from the correlated motions between a trapped particle and the surrounding solvent molecules[54], or the so-called hydrodynamic memory effects. The apparent colors in thermal noise that we observed here for the JNS particles must have a different origin. First of all, these JNS are more

than tenfold smaller in diameter than microspheres used by Franosch et al[53]. Particles of this size are very weakly trapped, as we showed previously[50,52], and as a result, the effect of hydrodynamic memory is small. The absence of these peaks in the symmetric particles we used as a control further supports this notion, and argues that it is the asymmetry within the JNS particles that gives rise to this phenomenon.

While optical trapping of JNS has been previously demonstrated, those experiments were not designed to detect active motion[25]. Our observation, however, is supported by work from Jiang et al. examining self-thermophoresis of gold/silica Janus microparticles under 1064 nm laser irradiation[24]. It is worth noting that these asymmetrical JNS nanoparticles are more challenging to trap than symmetrical nanoparticles, due to the active spin motion. Although a portion of the current JNS sample exhibited a peak in the power spectra, the data are reproducible over multiple experiments. Moreover, the frequency for this periodic motion is also reasonable for a particle of this size in a single-beam gradient optical trap[55]. Previous studies using polystyrene and gold nanoparticles subjected to circularly polarized light were able to achieve speeds up to 6 Hz and several kHz, respectively, the latter at a laser power of <50 mW and λ = 830 nm [56,57]. Furthermore, at these rotation speeds corresponding to high thermophoretic forces, it was predicted that the ability to optically trap JNS becomes strongly inhibited, leading to particle escape[58]. This is a common occurrence during current trapping experiments, which suggests that a larger population of JNS may actually exhibit active rotational motion than what we were able to stably trap and measure here.

2.4 Conclusions

We have generated an asymmetrical multi-building block Janus nanostructure (JNS) by employing a novel self-assembly approach that utilizes a thermo-cleavable polymer to control the location and self-assembly of nanoparticles. The data suggest that the asymmetrical JNS enhance photothermal effect and provide uneven thermophoretic force under NIR light, which generates active colored Brownian spin motion. These properties of the asymmetrical JNS could be used as both a strong photothermal mediator and a fuel-free nanoscale Janus motor under NIR light, which provides superior functions in the future compared to particles that have only either photothermal properties or rotational motion alone. JNS can simultaneously induce cancer cells death by increasing local temperature and potentially penetrate deeper in a tumor mass by the active rotational motion. These two properties make our JNS unique and possible to use in the future for cell manipulations, tissue penetration enhancement, and cargo deliveries[59–61].

2.5 Materials and methods

I. *Synthesis of difurfuryl adipate (DFA)*: Difurfuryl adipate was synthesized using the previously published method[62]. Briefly, 5.5 mmol adipoyl chloride was added dropwise to 11 mmol furfuryl alcohol with a few drops of triethanolamine (TEA) in dichloromethane. The reaction was carried out at 0 °C for 3 hours under nitrogen atmosphere. The product was purified by silica gel column chromatography eluted with petroleum ether and ethyl acetate (2:1). The final product was brown viscous liquid. The

chemical structure was confirmed by ^{1}H NMR spectroscopy (Varian 400 MHz) in dichloromethane (DCM)-d_4 and tetrachloro ethane (TCE)-d_2.

Synthesis of cleavable hydrophobic backbone polymer, Diels-Alder polymer (DA): The DA polymer was synthesized from difufuryl adipate (DFA) and bismaleimido diphenyl methane (BMD) monomers following previous literature[63,64]. An equimolar of DFA and BMD was mixed in TCE and the reaction was carried out at 70 °C for 7 days. The viscous yellow liquid was precipitated by excess petroleum ether and pale yellow powder was obtained. The powder was dried out under vacuum conditions. The final product was characterized by ^{1}HNMR spectroscopy in TCE-d_2. Molecular weight of DA was measured by gel permeation chromatography (GPC).

Cycloadduct conversion: In order to determine the percentage of cycloadduct conversion, DFA and BMD were reacted at 70 °C for 48 hours to induce Diel-Alder reaction. Retro Diels-Alder occurred at 100 °C and lead to the cycloadduct cleavage. The percentage of cycloadduct conversion was calculated from the area under the peaks appearing in ^{1}H NMR at 5.32 ppm and 7.43 ppm respectively. They indicated cycloadducts in the hydrophobic backbone and furan rings in the starting material respectively.

% Conversion = {AUC at 5.32ppm / [AUC at 5.32 ppm + AUC at 7.43 ppm]} x 100

Synthesis of thermo-cleavable polymer (DA-b-PEO) via Michael addition: The excess molar concentration of thiol-methoxy polyethylene oxide, molecular weight 5,000 Da (SH-mPEO), was added into the solution of DA polymer (1.5:1 molar ratio) in DCM

with a few drops of TEA. The solution was kept under stirring for one night and the product was precipitated into petroleum ether. The polymer structure was confirmed by ^{1}H NMR spectroscopy. Molecular weight was determined by GPC.

Synthesis of IONPs: 15 nm IONPs were synthesized using a previously reported method[65]. Briefly, a mixture of 0.890 g FeO(OH),19.8 g oleic acid and 25.0 g 1-octadecene in a three-neck flask were heated under stirring to 200 °C under N_2. 30 minutes later the temperature was set at 220 °C for 1 h, then the temperature was increased gradually to 310 °C (20 °C/5 minutes) and kept at this temperature for 1 h. The solution became black when the temperature was increased to 320 °C and kept at this temperature for 1 h. After the reaction was completed, the reaction mixture was cooled and the nanocrystals were precipitated by adding chloroform and acetone.

Au/IONP Janus nanostructure (JNS) formation: FeTCM (2.7 nM), AuTCM (0.2 μM), and DA-*b*-PEO (10.0 μM) were mixed together at room temperature. The solution was subsequently heated at 94 °C for 3 hours in a dry bath. The obtained JNS were centrifuged twice to remove free polymer seeds. The JNS solution was kept at 4 °C in the magnet separator (EasySep, USA) for one night to remove unreacted AuTCM.

Synthesis of FeBL and AuPS secondary nanostructures: To form iron oxide ball-like nanostructures (FeBL), FeTCM (0.54 nM) were homogeneously mixed with TCM seeds (0.2 μM) at room temperature. The formation of the ball-like structures was carried out at 95 °C for 2 hours in a dry bath. Then the solution was centrifuged to remove free TCM seeds and the pallets of ball-like nanostructures were redispersed in

Milli Q water. To form gold patchy nanostructures (AuPS), AuTCM (0.4 μM) was mixed with free TCM seeds (10.0 μM). The solution was heated at 94 °C for 3 hours in a heat block and purified by centrifugation. The final products were stored at 4 °C.

Synthesis of homogeneous Au/IONP micelles (GMC): Oleic acid coated-IONPs (1mg) and dodecanethiol AuNPs (1 mg) were dissolved together in THF and subsequently added into 20 mg of DA-*b*-PEO solution in THF under stirring. The resulting solution was slowly dropped into water under vigorous agitation. The product was purified twice by weight-separated centrifugation.

Characterization of nanoparticle: NP-loaded TCM, secondary structures, and JNS samples for TEM imaging were prepared by the solvent evaporation method. Briefly, the solution (5 μL) of each sample were dropped onto carbon-coated copper TEM grids and allowed to dry overnight. TEM images were acquired on a transmission electron microscope (TEM, Phillips CM-100, 60 kV). Scanning transmission electron microscopy (STEM) and X-ray energy dispersive spectroscopy (XEDS) were performed using Jeol JEM-2010F, operating at 200 kV with a double tilt holder. Images and size distributions were analyzed by *ImageJ* software from NIH and Gatan digital micrograph software. Hydrodynamic diameters were measured by using Malvern Zeta Sizer Nano S-90. Concentrations of Fe and Au were quantified by Inductively Coupled Plasma - Optical Emission Spectroscopy (ICP-OES) (Perkin-Elmer Optima 2000 DV). The samples were digested in aqua regia overnight before measurement. Percent yield of JNS was calculated by the equation shown below.

% yield of JNS = [Amount of Fe in JNS x 100]/ Amount of Fe in FeTCM

Photothermal effect and cell viability assay in triple negative breast cancer cells (SUM-159): The cells were cultured in a 5% CO_2 environment in F12 media (Invitrogen, Carlsbad, CA) supplemented with 5% fetal bovine serum (Fisher Scientific, Pittsburgh, PA), 1% antibiotic– antimycotic (Invitrogen, Carlsbad, CA), 5 µg/ml insulin (Sigma-Aldrich, St Louis, MO), 1 µg/ml hydrocortisone (Sigma-Aldrich, St Louis, MO), and 4 µg/ml gentamicin (Invitrogen, Carlsbad, CA). $3x10^3$cells were seeded in 96 well-plates overnight. The cells were incubated with JNS (0.17 mg/ml of gold and 0.04 mg/ml of iron), AuTCM (0.17 mg/ml of gold), FeTCM (0.04 mg/ml of iron), GMC (0.17 mg/ml of gold and 0.03 mg/ml of iron), solution mixture of AuTCM (0.17 mg/ml of gold) and FeTCM (0.04 mg/ml of iron), or cell culture media alone for 2 hours. The cells were irradiated using a NIR laser (885 nm, 0.45 W, spot size 5x8 mm^2, MDL-III- 885, OPTO Engine LLC, Midvale, UT) for 10 minutes. The temperature of the solutions was measured using a thermal camera (FLIR, Boston, MA). Nanoparticles were removed immediately after PTT and the cells were incubated overnight. Alamar blue (BIO-RAD, Raleigh, NC) was added to each well and incubated for 4 hours before fluorescent cell viability measurement at *Excitation:* 540 nm and *Emission:* 590nm.

Optical trapping of JNS: A custom-built optical tweezers instrument incorporating a tapered amplifier diode laser at 830 nm (SYS-420-830-1000, Sacher LaserTechnik LLC, Germany) was used for trapping AuTCM, FeTCM, and JNS samples. Briefly, the trapping laser was focused to a diffraction-limited spot using a 60X water-immersion

objective (Nikon, Melville, NY) with a numerical aperture of 1.2. The laser power was 130.8 mW at focus throughout the experiments, which were conducted at 20 ± 0.2 °C. Samples were diluted 10-fold in distilled water and separately injected into a microfluidic chamber of our construction. The optical trap is initially stationary, allowing individual, diffusing nanoparticles to be passively captured. Brownian motion of trapped particles was recorded with BFPI at 62.5 kHz for 10 s for the two axes that are perpendicular to the z-axis, i.e., the laser beam axis along the direction of beam propagation. This scan was repeated four times. Fitting of the corresponding power spectra in MATLAB (The Mathworks, Natick, MA) was done as previously described[50]. If the particle still remained in the optical trap after all scans were completed, it was released and a new particle was trapped after sufficient time had elapsed.

2.6 Acknowledgements

This work has originally published in *SMALL*,2016, DOI:10.1002/smll.201602569. Other authors contributing to this work include Michael C. DeSantis[1], Hongwei Chen[1], Wei Cheng[1], Kai Sun[2], Bo Wen[1], and Duxin Sun[1]. Kanokwan Sansanaphongpricha was sponsored by the Thai Government Scholarship Council. We also thank Microscopy & Image Analysis Laboratory (MIL) and The Michigan Center for Materials Characterization for imaging facilities.

1 Department of Pharmaceutical Sciences, University of Michigan, Ann Arbor, Michigan, 48109, United States

2 Department of Material Sciences and Engineering, University of Michigan, Ann Arbor, Michigan, 48109, United Stat

2.7 References

1. Kaewsaneha, C., Tangboriboonrat, P., Polpanich, D., Eissa, M. & Elaissari, A. Janus colloidal particles: preparation, properties, and biomedical applications. *ACS Appl. Mater. Interfaces* **5,** 1857–69 (2013).
2. Perro, A., Reculusa, S., Ravaine, S., Bourgeat-Lami, E. & Duguet, E. Design and synthesis of Janus micro- and nanoparticles. *J. Mater. Chem.* **15,** 3745 (2005).
3. Tran, L.-T.-C., Lesieur, S. & Faivre, V. Janus nanoparticles: materials, preparation and recent advances in drug delivery. *Expert Opin. Drug Deliv.* **11,** 1061–74 (2014).
4. Bhaskar, S. *et al.* Engineering, characterization and directional self-assembly of anisotropically modified nanocolloids. *Small* **7,** 812–9 (2011).
5. Du, J. & O'Reilly, R. K. Anisotropic particles with patchy, multicompartment and Janus architectures: preparation and application. *Chem. Soc. Rev.* **40,** 2402–2416 (2011).
6. Hu, S.-H. & Gao, X. Nanocomposites with spatially separated functionalities for combined imaging and magnetolytic therapy. *J. Am. Chem. Soc.* **132,** 7234–7 (2010).
7. Gao, W., Pei, A., Feng, X., Hennessy, C. & Wang, J. Organized self-assembly of janus micromotors with hydrophobic hemispheres. *J. Am. Chem. Soc.* **135,** 998–1001 (2013).
8. Reguera, J., Kim, H. & Stellacci, F. Advances in Janus nanoparticles. *Chimia (Aarau).* **67,** 811–8 (2013).
9. Ghosh, S. K. & Pal, T. Interparticle coupling effect on the surface plasmon resonance of gold nanoparticles: From theory to applications. *Chemical Reviews* **107,** 4797–4862 (2007).
10. Yan, L., Popp, N., Ghosh, S. & Boker, A. Self-assembly of Janus nanoparticles in diblock copolymers. *ACS Nano* **4,** 913–920 (2010).
11. Jiang, S. *et al.* Janus particle synthesis and assembly. *Adv. Mater.* **22,** 1060–71 (2010).
12. Lattuada, M. & Hatton, T. A. Synthesis, properties and applications of Janus nanoparticles. *Nano Today* **6,** 286–308 (2011).
13. Lattuada, M. & Hatton, T. A. Preparation and Controlled Self-Assembly of Janus Magnetic Nanoparticles. *J. Am. Chem. Soc.* **129,** 12878–12889 (2007).
14. Wurm, F. & Kilbinger, A. F. M. Polymeric janus particles. *Angew. Chem. Int. Ed. Engl.* **48,** 8412–21 (2009).
15. Hickey, R. J. *et al.* Size-controlled self-assembly of superparamagnetic polymersomes. *ACS Nano* **8,** 495–502 (2014).
16. Lamarre, S. S., Lemay, C., Labrecque, C. & Ritcey, A. M. Controlled 2D organization of gold nanoparticles in block copolymer monolayers. *Langmuir* **29,** 10891–8 (2013).
17. He, J. *et al.* Self-assembly of amphiphilic plasmonic micelle-like nanoparticles in selective solvents. *J. Am. Chem. Soc.* **135,** 7974–84 (2013).
18. Kanahara, M., Shimomura, M. & Yabu, H. Fabrication of gold nanoparticle-polymer composite particles with raspberry, core-shell and amorphous morphologies at room temperature via electrostatic interactions and diffusion. *Soft Matter* **10,** 275–80 (2014).
19. Hickey, R. J., Meng, X., Zhang, P. & Park, S.-J. Low-dimensional nanoparticle clustering in polymer micelles and their transverse relaxivity rates. *ACS Nano* **7,** 5824–33 (2013).
20. Zubarev, E. R., Xu, J., Sayyad, A. & Gibson, J. D. Amphiphilicity-driven organization of nanoparticles into discrete assemblies. *J. Am. Chem. Soc.* **128,** 15098–9 (2006).
21. Zhang, Z., Horsch, M. a., Lamm, M. H. & Glotzer, S. C. Tethered Nano Building Blocks: Toward a Conceptual Framework for Nanoparticle Self-Assembly. *Nano Lett.* **3,** 1341–1346 (2003).
22. Huang, X. & El-Sayed, M. A. Gold nanoparticles: Optical properties and implementations in cancer diagnosis and photothermal therapy. *J. Adv. Res.* **1,** 13–28 (2010).
23. Shen, S. *et al.* Magnetic nanoparticle clusters for photothermal therapy with near-infrared irradiation. *Biomaterials* **39,** 67–74 (2015).
24. Jiang, H. R., Yoshinaga, N. & Sano, M. Active motion of a Janus particle by self-thermophoresis in

a defocused laser beam. *Phys. Rev. Lett.* **105,** 1–4 (2010).
25. Nedev, S. *et al.* An optically controlled microscale elevator using plasmonic janus particles. *ACS Photonics* **2,** 491–496 (2015).
26. Wu, Z., Lin, X., Si, T. & He, Q. Recent Progress on Bioinspired Self-Propelled Micro/Nanomotors via Controlled Molecular Self-Assembly. *Small* **12,** 3080–93 (2016).
27. Wu, Y., Wu, Z., Lin, X., He, Q. & Li, J. Autonomous movement of controllable assembled Janus capsule motors. *ACS Nano* **6,** 10910–10916 (2012).
28. Wu, Z. *et al.* Near-infrared light-triggered on/off motion of polymer multilayer rockets. *ACS Nano* **8,** 6097–6105 (2014).
29. Wu, Z., Lin, X., Si, T. & He, Q. Recent Progress on Bioinspired Self-Propelled Micro/Nanomotors via Controlled Molecular Self-Assembly. *Small* **12,** 3080–3093 (2016).
30. Goussé, C. & Gandini, A. Diels–Alder polymerization of difurans with bismaleimides. *Polym. Int.* **48,** 723–731 (1999).
31. Gandini, A. The furan/maleimide Diels–Alder reaction: A versatile click–unclick tool in macromolecular synthesis. *Prog. Polym. Sci.* **38,** 1–29 (2013).
32. Hall, D. J., Van Den Berghe, H. M. & Dove, A. P. Synthesis and post-polymerization modification of maleimide-containing polymers by 'thiol-ene' click and Diels-Alder chemistries. *Polym. Int.* **60,** 1149–1157 (2011).
33. Grzelczak, M., Vermant, J., Furst, E. M. & Liz-marza, L. M. Directed Self-Assembly of Nanoparticles. *ACS Nano* **4,** 3591–3605 (2010).
34. Luo, L. & Eisenberg, A. Thermodynamic Size Control of Block Copolymer Vesicles in Solution. *Langmuir* **17,** 6804–6811 (2001).
35. Owen, S. C., Chan, D. P. Y. & Shoichet, M. S. Polymeric micelle stability. *Nano Today* **7,** 53–65 (2012).
36. Deng, H., Dai, F., Ma, G. & Zhang, X. Theranostic Gold Nanomicelles made from Biocompatible Comb-like Polymers for Thermochemotherapy and Multifunctional Imaging with Rapid Clearance. *Adv. Mater.* **27,** 3645–3653 (2015).
37. Deng, H. *et al.* Theranostic self-assembly structure of gold nanoparticles for NIR photothermal therapy and X-Ray computed tomography imaging. *Theranostics* **4,** 904–918 (2014).
38. Liu, Y. *et al.* Entropy-driven pattern formation of hybrid vesicular assemblies made from molecular and nanoparticle amphiphiles. *J. Am. Chem. Soc.* **136,** 2602–2610 (2014).
39. Nikolic, M. S. *et al.* Micelle and vesicle formation of amphiphilic nanopartieles. *Angew. Chemie - Int. Ed.* **48,** 2752–2754 (2009).
40. Mackay, M. E. *et al.* REPORTS General Strategies for Nanoparticle Dispersion. *Science* **311,** 1740–1744 (2006).
41. Thompson, R. B., Ginzburg, V. V., Matsen, M. W. & Balazs, A. C. Predicting the Mesophases of Composites. *Science* **292,** 2469–2473 (2001).
42. Walther, A., Matussek, K. & Muller, A. H. E. Engineering Nanostructured Polymer Blends with Controlled Nanoparticle Location using Janus Particles. *ACS Nano* **2,** 1167–1178 (2008).
43. Jaque, D. *et al.* Nanoparticles for photothermal therapies. *Nanoscale* **6,** 9494–530 (2014).
44. Melamed, J. R., Edelstein, R. S. & Day, E. S. Elucidating the Fundamental Mechanisms of Cell Death Triggered by Photothermal Therapy. *ACS Nano* **9,** 6–11 (2015).
45. Huang, X. & El-Sayed, M. A. Plasmonic photo-thermal therapy (PPTT). *Alexandria J. Med.* **47,** 1–9 (2011).
46. Huang, X., El-Sayed, I. H., Qian, W. & El-Sayed, M. a. Cancer cell imaging and photothermal therapy in the near-infrared region by using gold nanorods. *J. Am. Chem. Soc.* **128,** 2115–20 (2006).
47. Govorov, A. O. & Richardson, H. H. Generating heat with metal nanoparticles. *Nano Today* **2,** 30–38 (2007).
48. Govorov, A. O. *et al.* Gold nanoparticle ensembles as heaters and actuators: Melting and collective plasmon resonances. *Nanoscale Res. Lett.* **1,** 84–90 (2006).
49. Zhang, W., Li, Q. & Qiu, M. A plasmon ruler based on nanoscale photothermal effect. *Opt. Express* **21,** 172–181 (2013).
50. Pang, Y., Song, H., Kim, J. H., Hou, X. & Cheng, W. Optical trapping of individual human

immunodeficiency viruses in culture fluid reveals heterogeneity with single-molecule resolution. *Nat. Nanotechnol.* **9,** 624–630 (2014).
51. Hänggi, P. & Jung, P. in *Advances in Chemical Physics* **89,** 239–326 (1994).
52. Pang, Y., Song, H. & Cheng, W. Using optical trap to measure the refractive index of a single animal virus in culture fluid with high precision. *Biomed. Opt. Express* **7,** 1672 (2016).
53. Franosch, T. *et al.* Resonances arising from hydrodynamic memory in Brownian motion - The colour of thermal noise. *Nature* **478,** 8–11 (2011).
54. Berg-Sorensen, K. & Flyvbjerg, H. The colour of thermal noise in classical Brownian motion: A feasibility study of direct experimental observation. *New J. Phys.* **7,** (2005).
55. Friese, M. E. J., Nieminen, T. A., Heckenberg, N. R. & Rubinsztein-Dunlop, H. Optical alignment and spinning of laser-trapped microscopic particles. *Nature* **394,** 348–350 (1998).
56. Wang, K., Schonbrun, E., Steinvurzel, P. & Crozier, K. B. Trapping and rotating nanoparticles using a plasmonic nano-tweezer with an integrated heat sink. *Nat. Commun.* **2,** 469 (2011).
57. Lehmuskero, A., Ogier, R., Gschneidtner, T., Johansson, P. & Käll, M. Ultrafast spinning of gold nanoparticles in water using circularly polarized light. *Nano Lett.* **13,** 3129–3134 (2013).
58. Schermer, R. T., Olson, C. C., Coleman, J. P. & Bucholtz, F. Laser-induced thermophoresis of individual particles in a viscous liquid. *Opt. Express* **19,** 10571–10586 (2011).
59. Gao, W. *et al.* Arti fi cial Micromotors in the Mouse ' s Stomach : A Step toward in Vivo Use of. *ACS Nano* **9,** 117–123 (2014).
60. Baraban, L. *et al.* Catalytic Janus motors on microfluidic chip: Deterministic motion for targeted cargo delivery. *ACS Nano* **6,** 3383–3389 (2012).
61. Baraban, L. *et al.* Transport of cargo by catalytic Janus micro-motors. *Soft Matter* **8,** 48 (2012).
62. Kuramoto, N., Hayashi, K. & Nagai, K. Thermoreversible reaction of diels—alder polymer composed of difurufuryladipate with bismaleimidodiphenylmethane. *Polym. Sci.* 2501–2504 (1994).
63. Gandini, A., Coelho, D., Gomes, M., Reis, B. & Silvestre, A. Materials from renewable resources based on furan monomers and furan chemistry: work in progress. *J. Mater. Chem.* **19,** 8656 (2009).
64. Gandini, A., Coelho, D. & Silvestre, A. J. D. Reversible click chemistry at the service of macromolecular materials. Part 1: Kinetics of the Diels–Alder reaction applied to furan–maleimide model compounds and linear polymerizations. *Eur. Polym. J.* **44,** 4029–4036 (2008).
65. Chen, H. *et al.* 'Living' PEGylation on gold nanoparticles to optimize cancer cell uptake by controlling targeting ligand and charge densities. *Nanotechnology* **24,** 355101 (2013).
66. Sansanaphongpricha, K. *et al.* Multibuilding Block Janus Synthesized by Seed-Mediated Self-Assembly for Enhanced Photothermal Effects and Colored Brownian Motion in an Optical Trap. *Small* **1602569,** 1–11 (2016).

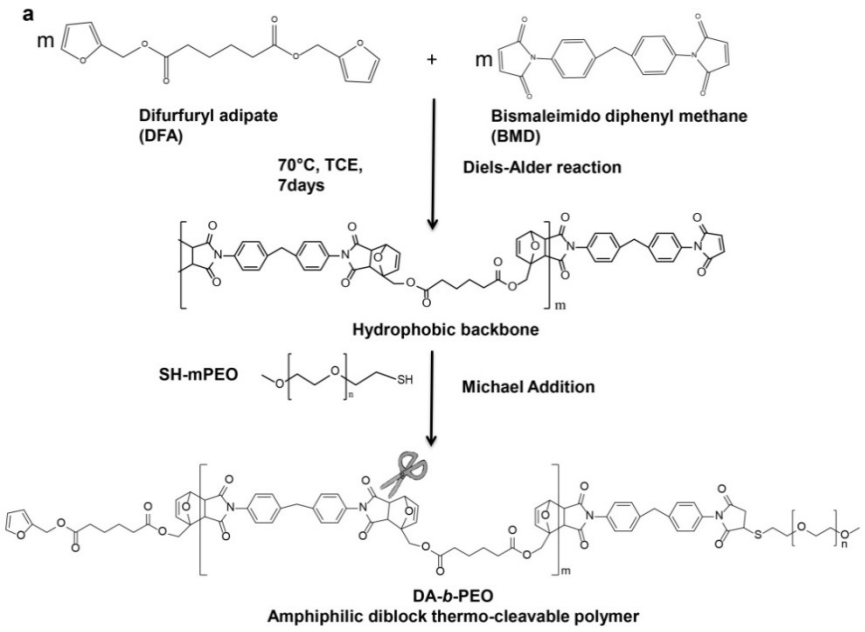
a
m
Difurfuryl adipate
(DFA)
+
m
Bismaleimido diphenyl methane
(BMD)
70°C, TCE,
7days
Diels-Alder reaction
Hydrophobic backbone
SH-mPEO
SH
Michael Addition
DA-b-PEO
Amphiphilic diblock thermo-cleavable polymer

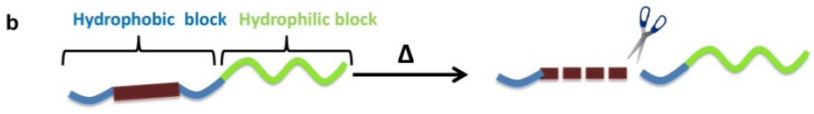
b
Hydrophobic block
Hydrophilic block
Δ

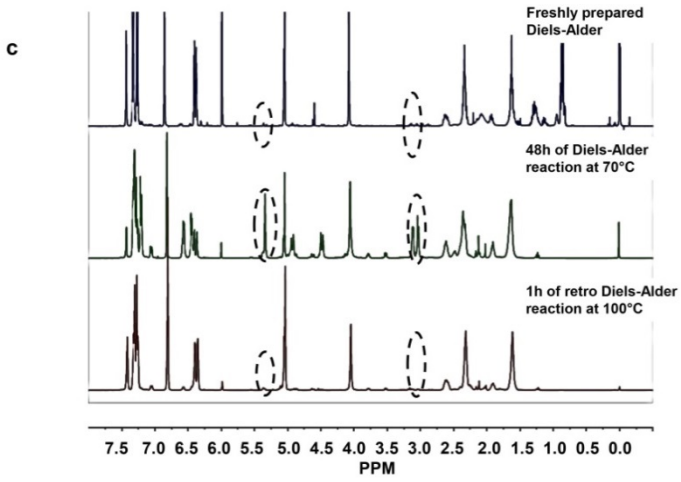
c
Freshly prepared
Diels-Alder
48h of Diels-Alder
reaction at 70°C
1h of retro Diels-Alder
reaction at 100°C
7.5 7.0 6.5 6.0 5.5 5.0 4.5 4.0 3.5 3.0 2.5 2.0 1.5 1.0 0.5 0.0
PPM

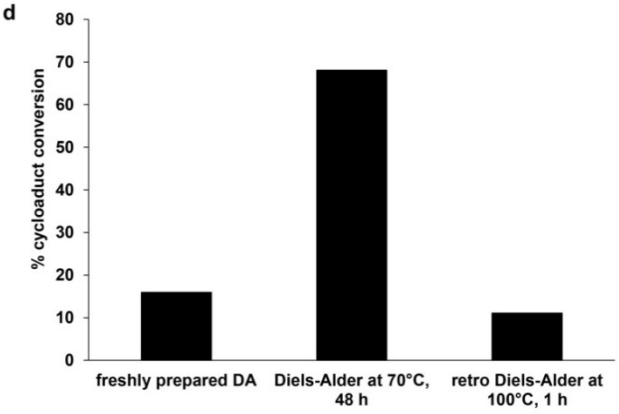
d
% cycloaduct conversion
80
70
60
50
40
30
20
10
0
freshly prepared DA
Diels-Alder at 70°C,
48 h
retro Diels-Alder at
100°C, 1 h

Figure 2.1. a) A synthesis scheme of DA-*b*-PEO amphiphilic diblock thermo-cleavable copolymer. An equimolar of DFA and BMD was mixed in tetrachloro ethane and the reaction was carried out at 70 °C for 7 days. The molecular weight of the polymer was 5,090 Da. Then SH-mPEG was conjugated with the maleimide terminus of the hydrophobic backbone via Michael addition and yielded the final product with the molecular weight of 9,800 Da. b) A cartoon picture representing the thermo-cleavable polymer and the hydrophobic backbone cleavage after high temperature exposure. c) ^{1}H NMR of the hydrophobic backbone at different time points and temperatures: freshly prepared (top), 48 hours after 70 °C heat treatment (middle), and 1 hour after 100 °C heat treatment. It clearly shows that the cycloadducts peak at 3.09 and 5.32 ppm increase after polymerization via Diels-Alder reaction at 70 °C for 48 hours. However, these peaks disappear after the temperature increases to 100 °C for an hour. This indicates the cycloadduct disruption via retro Diels-Alder. d) 84% of the cycloadducts were cleaved after being treated at 100 °C for an hour. The data suggest that the backbone cleavage is very efficient after one hour of high temperature exposure.

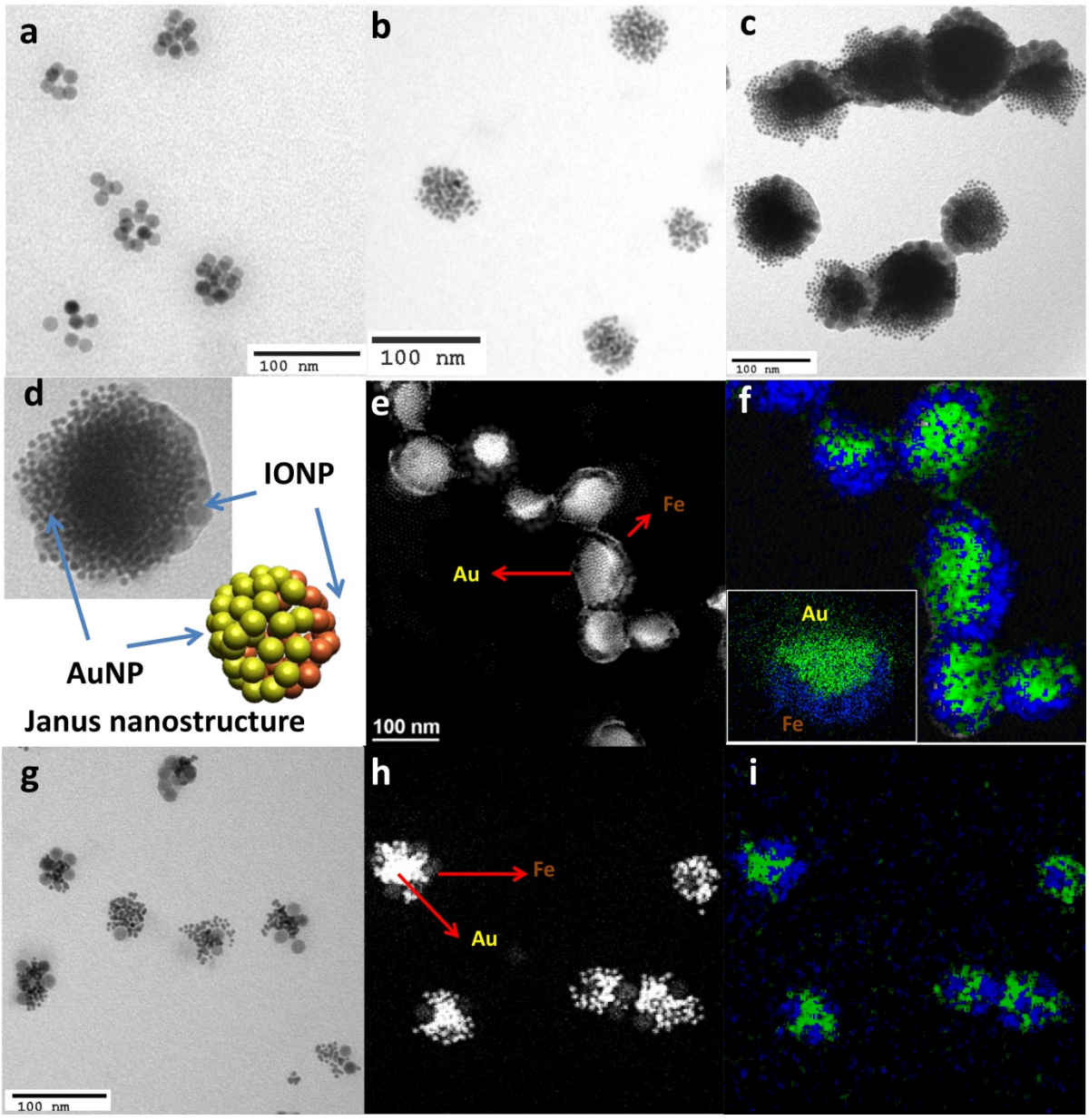

Figure 2.2. TEM images of Janus Nanostructures (JNS). a) The TEM images of the original FeTCM and b) AuTCM before heat treatment. c) A TEM image of multi-building block Au/IONP JNS after self-assembly process. d) A high magnification TEM image and a cartoon picture show an asymmetrical structure of JNS. e) A STEM-HADDF image of JNS and f) XEDS element maps of JNS confirm an asymmetrical pattern of JNS. g) TEM, h) STEM, and i) XEDS images of homogeneous dodecenethiol-coated AuNPs and oleic-coated IONPs loaded in TCM show a random pattern of Au/IONP mixture in micelles (GMC)

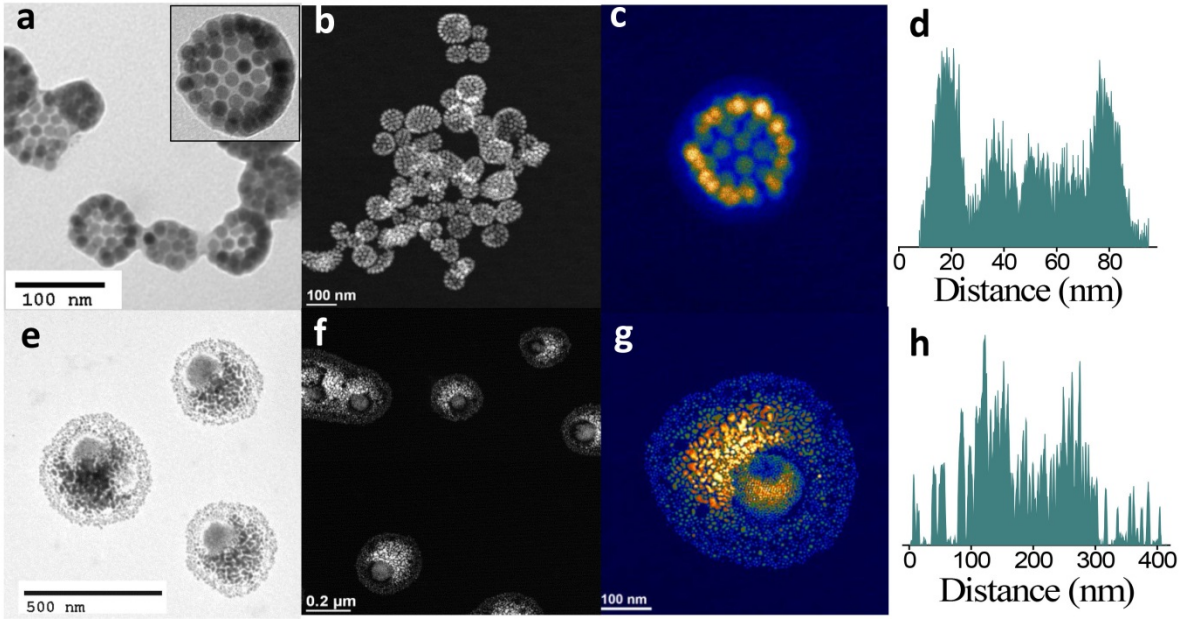

Figure 2.3. The TEM images of secondary structures. a) and e) represent TEM images of FeBL and AuPS after self-assembly of FeTCM and AuTCM respectively. b) and f) demonstrate STEM-HADDF images of FeBL and AuPS at low magnifications. c) and g) are STEM-HADDF images of FeBL and AuPS at high magnifications with a color heat map. d) and h) show density profiles of FeBL and AuPS, implying that nanoparticles aligning at the polymer interface rather than inside the core.

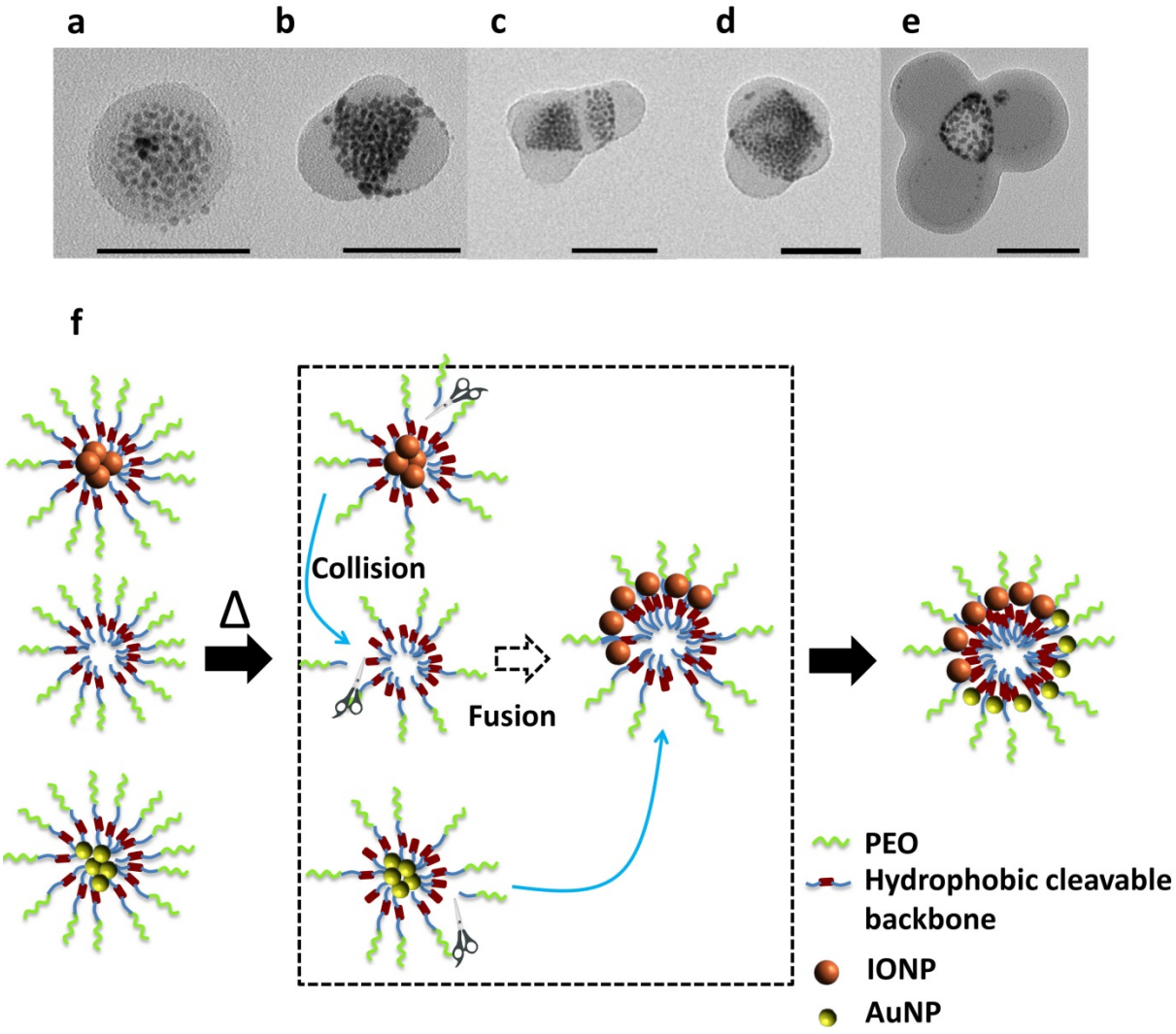

Figure 2.4. TEM images and scheme of self-assembly process. a) TEM image of AuTCM at high magnification. The sample was taken at the beginning of heat treatment. b) - d) Series of TEM images showing multiple AuTCMs fusion process. e) TEM image demonstrating internal phase separation and structural rearrangement to form secondary structures. Scale bars from (a-e) are 100 nm. f) Schematic diagram demonstrates the transformation mechanism from cluster micelles to multi-building block Janus or ball-like nanostructures. First, a FeTCM collides with free TCM seed. Simultaneously, another AuTCM can also collide with the same seed from the opposite direction and subsequently fuse together, resulting in self-reorganization to form JNS. If only one kind of NP-TCMs is used, ball-like or patchy structures will be formed instead of JNS.

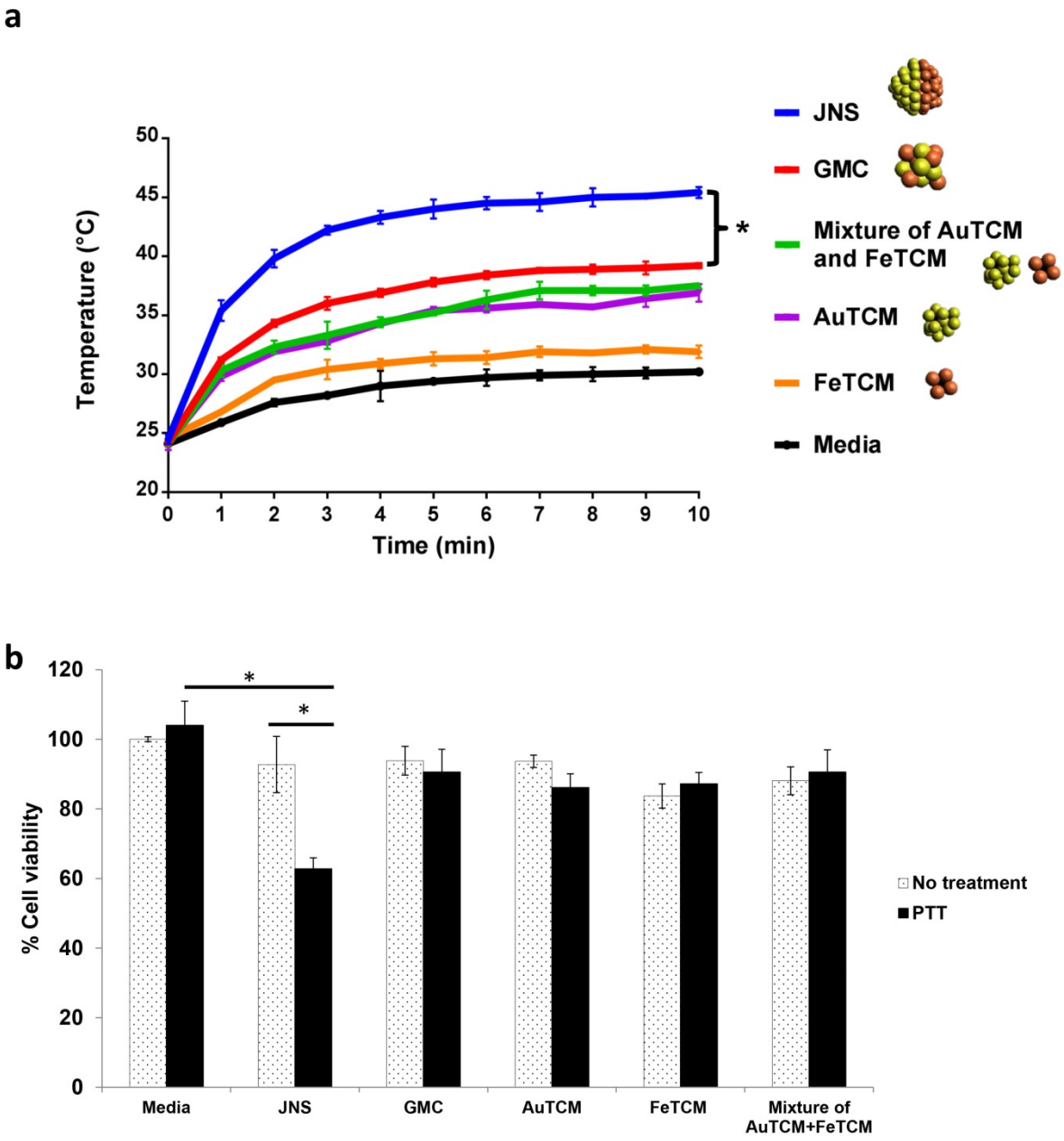

Figure 2.5. JNS enhances photothermal effect. a) Graph shows photothermal effect of different types of nanoparticles. JNS significantly enhances the temperature after NIR laser light irradiation at 885 nm for 10 minutes comparing to other structures. The asterisk shows significant difference, P-value < 0.05. b) Percentage of SUM-159 cell viability with and without photothermal treatment in different types of nanoparticles. The asterisks show P-value < 0.05.

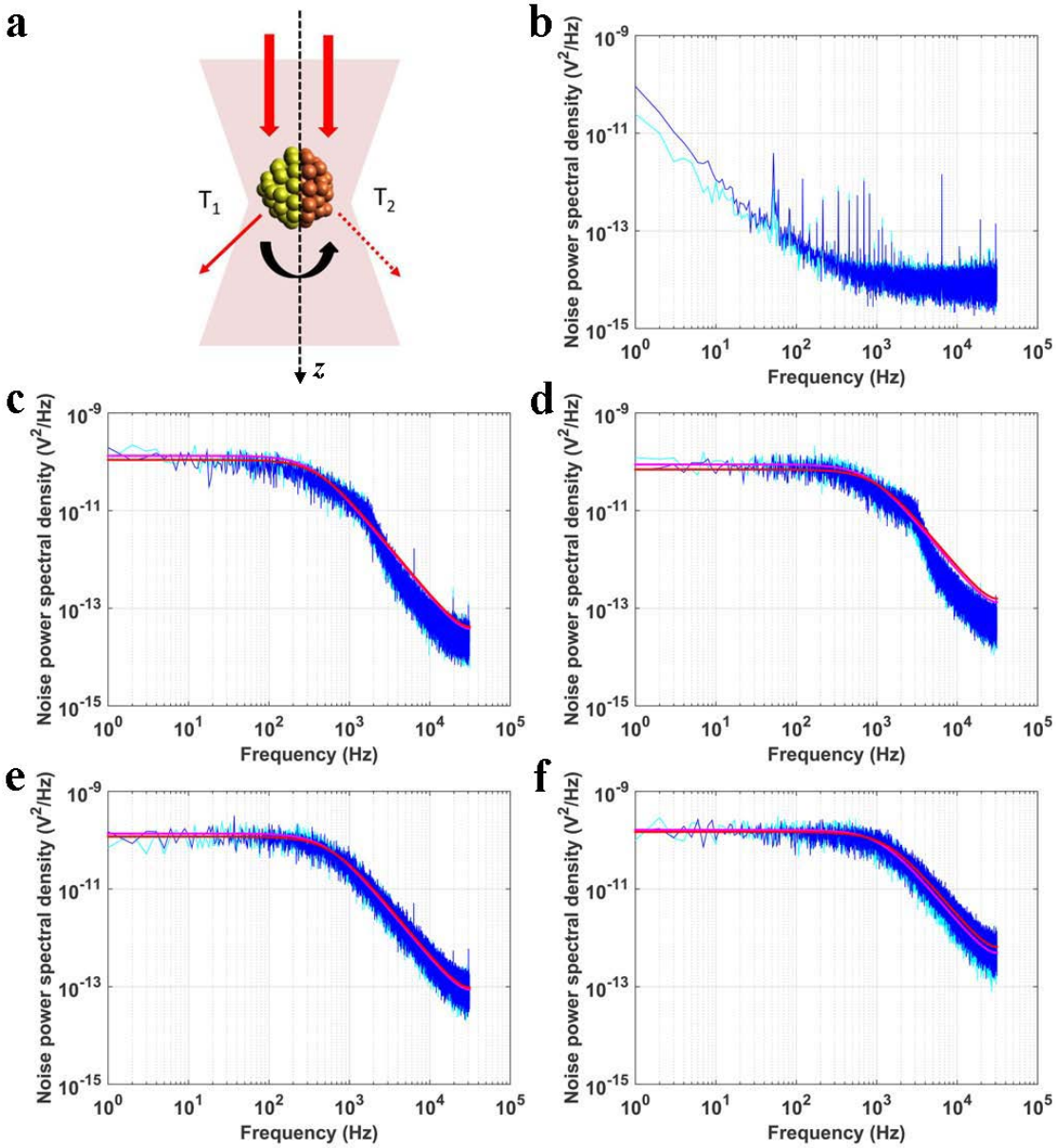

Figure 2.6. JNS displays colored Brownian motions in a single-beam gradient optical trap. a) A hypothetical cartoon to illustrate the local temperature imbalance around a single JNS particle, which drives the rotation of the particle at the focal plane. b) Power spectra for laser-only collected along x- and y-axis. c-d) Representative power spectra for JNS particles displaying rotational motion in the optical trap. The best Lorentzian fits for each spectrum are overlaid, resulting in reduced χ^2values of 1.31 (red in c), 1.33 (purple in c), 1.21 (red in d) and 1.20 (purple in d), respectively. e-f) Representative power spectra for AuTCMs and FeTCMs in the optical trap, respectively. The best Lorentzian fits for each spectrum are overlaid, resulting in reduced χ^2 values of 1.11 (red in e), 1.11 (purple in e), 1.10 (red in f) and 1.11 (purple in f), respectively. For panels b-f, the power spectra along x-axis are shown in cyan while the power spectra along y-axis are shown in blue. The fits for spectra along x-axis are shown in red while the fits for spectra along y-axis are shown in purple. The xy plane is the focal plane that is perpendicular to beam axis z.

2.8 Supporting information

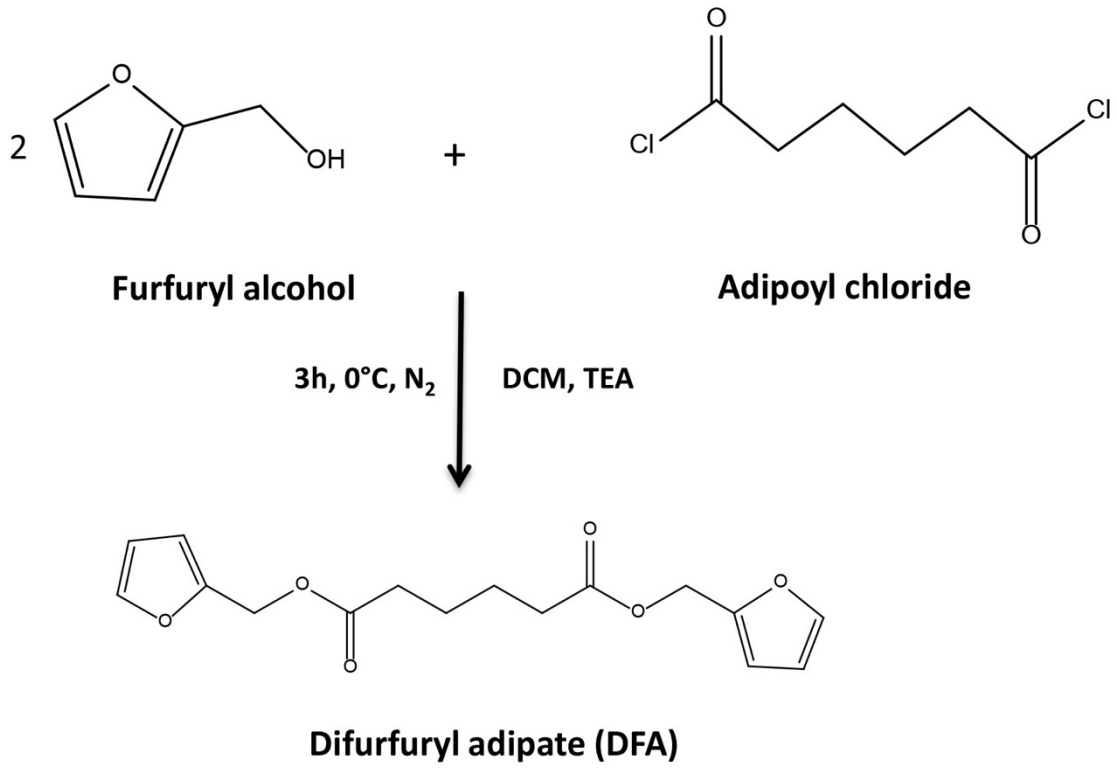

Figure 2.S1. A synthesis scheme of DFA monomer. DFA was synthesized from furfuryl alcohol and adipoyl chloride in DCM with a few drops of TEA under nitrogen atmosphere at 0°C for 3 hours. DFA was characterized by ^{1}H NMR (400 MHz, TCE-d_2) δ 7.43 (d, J = 2.0 Hz, 2H), δ 6.41 (d, J = 2.8Hz, 2H), δ 6.37 (dd, J_1 = 3.6Hz, J_2 = 2.0Hz, 2H), 5.04 (s, 4H), 2.34 (p, J_1 = 7.2 Hz, J_2 = 3.2Hz, 4H), 1.63 (t, J = 3.4 Hz, 4H).

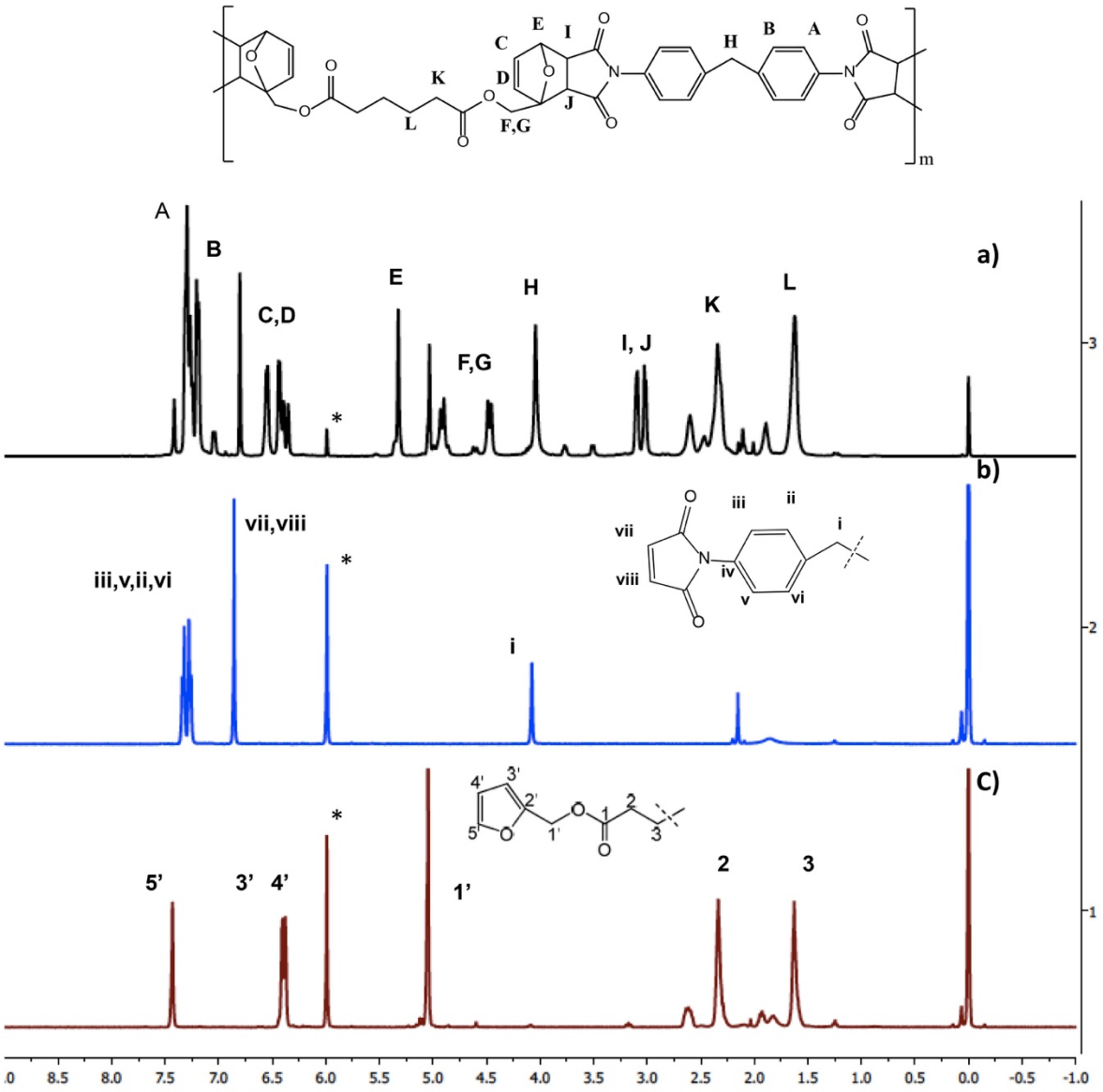

Figure 2.S2. ^{1}H NMR of hydrophobic backbone Diel-Alder polymer (a), bismaleimido diphenyl methane (BMD) (b), and difurfuryl adipate (DFA) (c). BMD and DFA covalently form cycloadducts as shown in ^{1}H NMR at δ 7.30 (d, J = 8 Hz, 4H), δ 7.19 (d, J = 8 Hz, 4H), δ 6.55 (d, J = 6.4 Hz, 2H), δ 6.43 (d, J = 5.6 Hz, 2H), δ 5.32 (s, 2H), δ 4.91 (d, J = 13.2 Hz, 2H), δ 4.47 (d, J = 13.2 Hz, 2H), δ 4.04 (s, 2H), δ 3.09 (d, J = 5.6 Hz, 2H), δ 3.02 (d, J = 6.4 Hz, 2H), δ 2.34 (m, 4H), δ 1.63 (m, 4H). The asterisk (*) indicates a solvent peak.

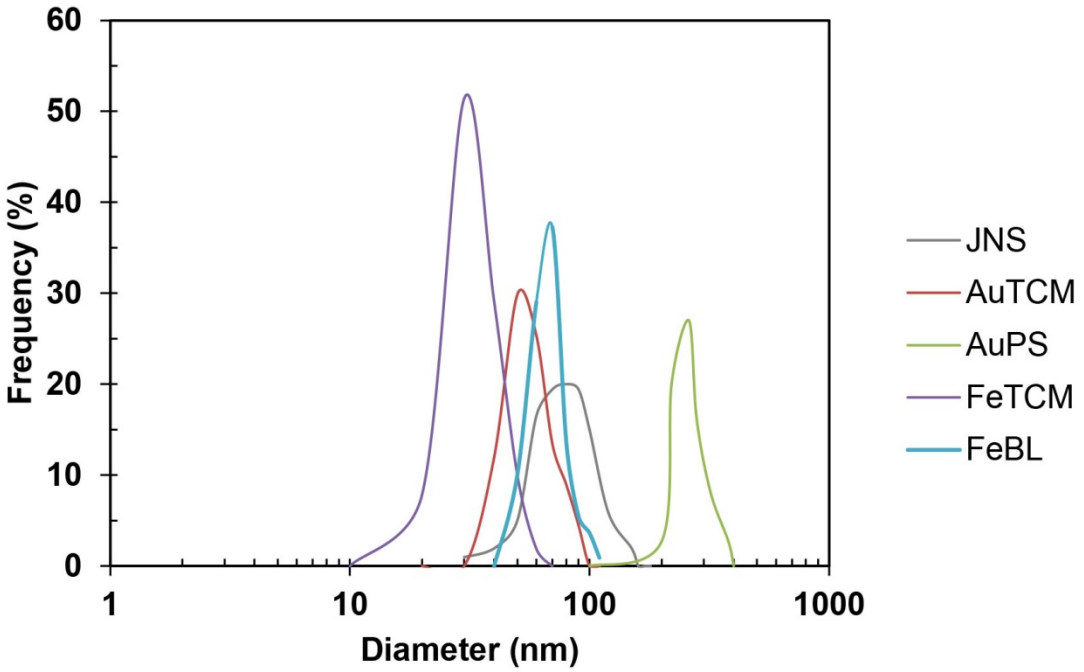

Figure 2.S3. Core diameters and size distributions of JNS, AuTCM, AuPS, FeTCM and FeBL measured by TEM and analyzing by Image J.

	Hydrodynamic Diameter (nm)	Polydispersity index (PDI)
TCM	93.82	0.35
FeTCM	78.82	0.22
AuTCM	94.88	0.24
JNS	100.30	0.12

Table 2.S1. The table shows hydrodynamic diameters and polydispersesity index of TCM seed, FeTCM, AuTCM, and JNS. Each sample was measure in triplicate by using Malvern Zeta sizer with disposable cuvettes. The core diameters of micelles measured by DLS are larger than the diameter of micelles measured by TEM because of the interaction between the media and the polymer coating nanoparticles.

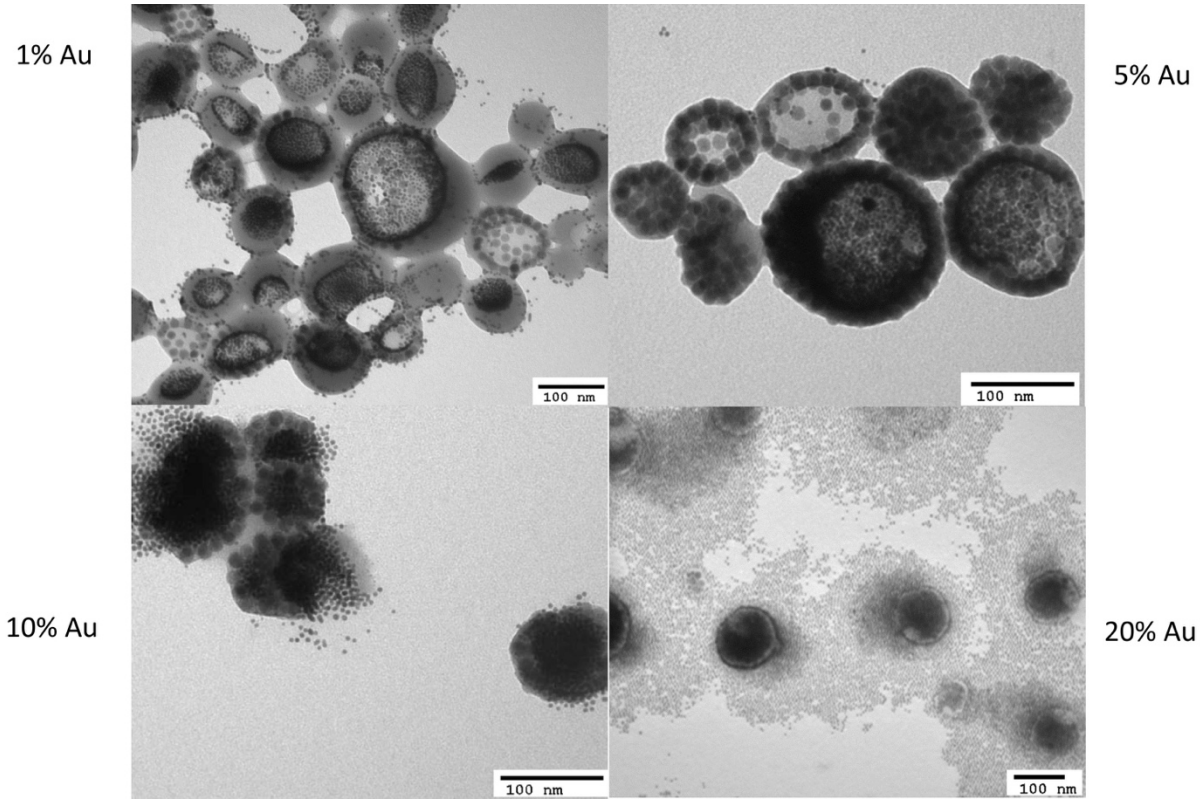

Figure 2.S4. TEM images show the different number of AuNP and IONP and structural differences of JNS formed from different ratios of AuTCM and FeTCM. The percentage of AuNP in AuTCM was varied as indicated in the Figure ures. 1% and 5% of AuTCM yielded uncompleted JNS and FeBL were found in the product after purification. While 20% AuNP in AuTCM show over excessive AuNP that are unreacted to FeTCM and free TCM resulting in releasing single AuNPs and cause precipitation. 10% AuNP in AuTCM represent the optimal JNS nanostructures as there is neither unreacted AuNP nor FeBL appearing in TEM images.

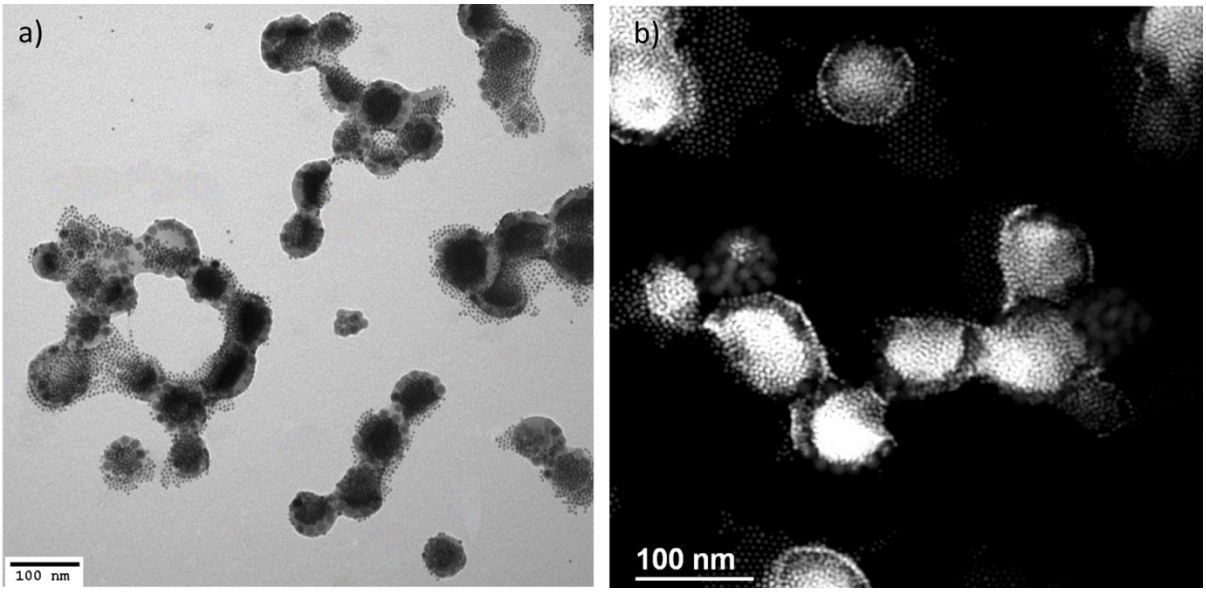

Figure 2.S5. a) and b) represent a TEM and STEM-HADDF image of JNS showing that multiple AuNP and IONP are combined together as a single entity regardless of their orientation under the TEM and STEM. Darker tiny dots under TEM image and brighter spots under STEM image indicates AuNPs. The big grey spheres under TEM image and dark sphere under STEM represent IONPs.

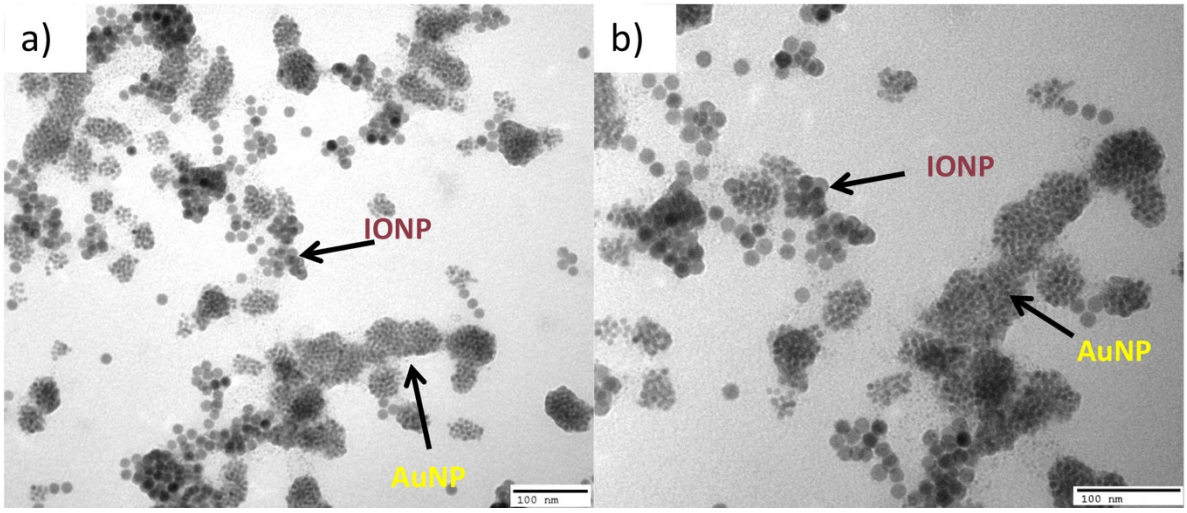

Figure 2.S6. TEM images of the mixture of 5 nm AuNPs encapsulated in non-TCM (PS-*b*-PEO) and 15 nm IONPs loaded in non-TCM before (a) and after (b) 3 hours of high temperature treatment with free non-TCM seeds. The data suggest that there was no JNS formation. These two types of NP-TCMs remained separated in the solution. Scale bars are 100 nm.

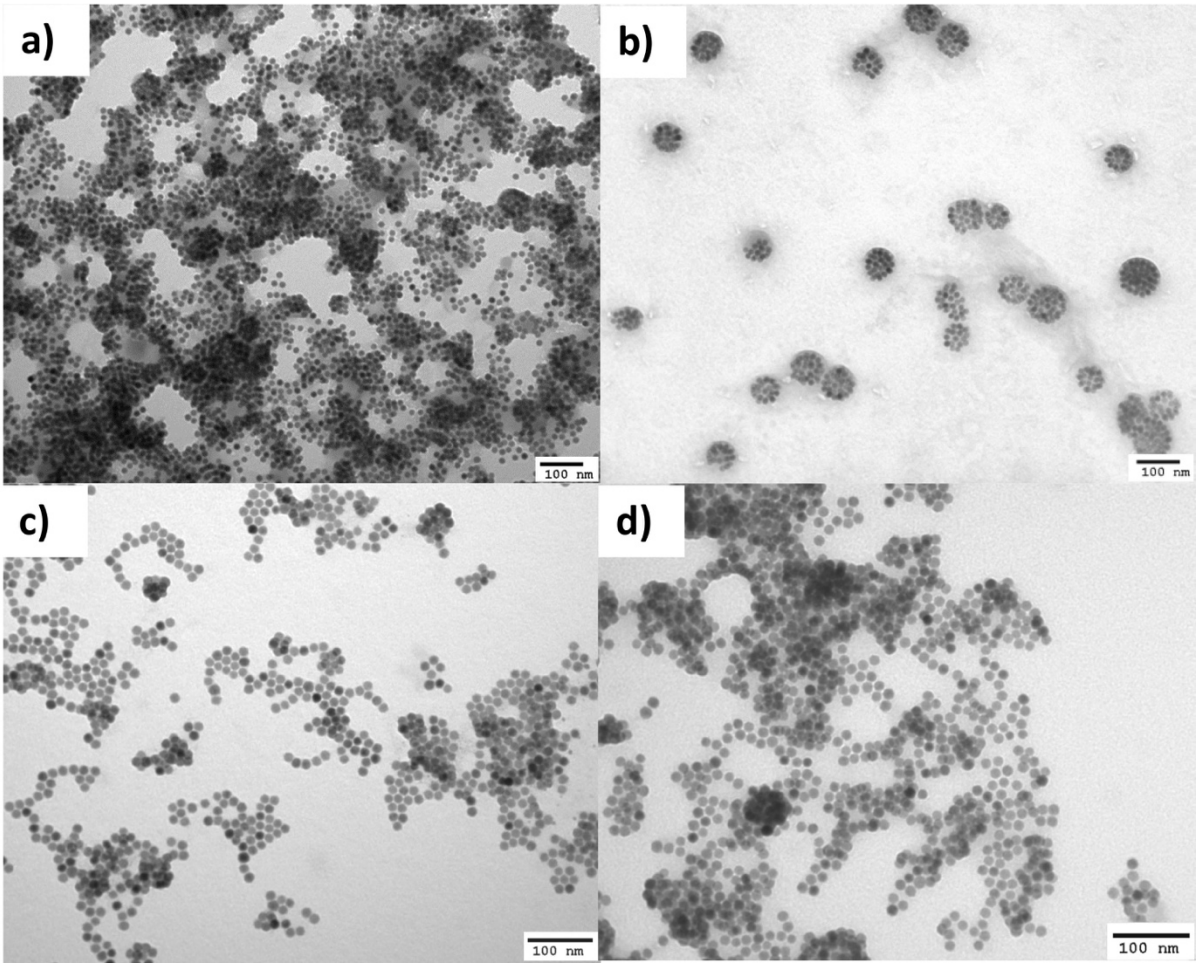

Figure 2.S7. TEM images of FeTCMs before (a) and after (b) heat trigger. Morphological transformation of FeTCM is clearly observed under TEM. The cluster FeTCMs can undergo self-assembly and form FeBL. (c) and (d) show TEM images of nonFeTCMs before and after heat trigger respectively. No structural transformation was observed.

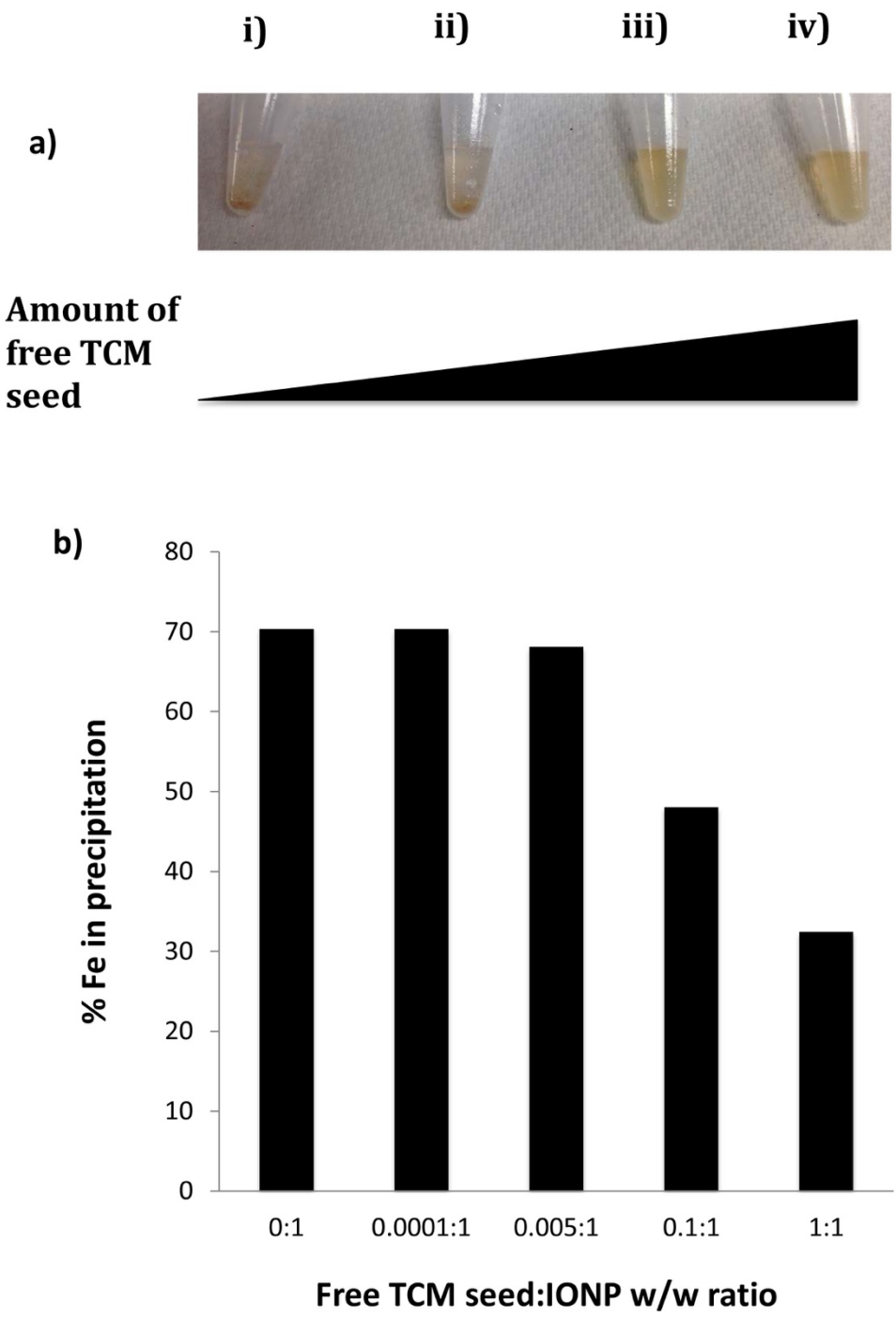

Figure 2.S8. (a)Top panel shows that IONPs were released from the micelles and precipitated in the aqueous media. The amount of precipitation is inversely proportional to the amount of free TCM seeds. (b)The bottom chart shows percentage of iron precipitation released from the micelles at different weight ratios of the TCM seed with the fixing amount of IONPs (1mg).

CHAPTER 3

THERMO-CLEAVABLE POLYMERIC MICELLES FOR NIR-TRIGGERED DRUG AND NANOPARTICLE DELIVERY

3.1 Abstract

A novel thermo-cleavable polymer, difurfuryl adipate-bismaleimido diphenyl methane-*b*-polyethylene oxide (DA-*b*-PEO), was developed for NIR-triggered drug release and nanoparticle delivery. The hydrophobic polymer backbone, difurfuryl adipate-bismaleimido diphenyl methane (DA), is dissociated after being exposed to high temperature (80°C) or near-infrared light (NIR) via retro Diels-Alder reaction. The polymer was characterized by ^{1}H nuclear magnetic resonance (^{1}H NMR) and gel permeation chromatography (GPC). Iron oxides nanoparticles (IONPs) and Doxorubicin (Dox) were simultaneously encapsulated in thermos-cleavable polymeric micelles. IONPs are used as a photothermal mediator and Dox is used as a model drug. IONP can convert from NIR light to heat, which induces polymer backbone cleavage that releases both IONPs and Dox from micelles. The amount of Dox release was determined by UV-visible spectrophotometer. We also observed and confirmed by transmission electron microscopy (TEM) the transformation process from clustered IONP micelles to single-dispersed IONP micelles. The transformation occurs

simultaneously with the release of the payload. After the polymer backbone cleavage, the cleaved polymer interacts with the released IONPs and transforms them into single-dispersed IONP micelles. These IONP-Dox thermo-cleavable micelles can be used for non-invasive and light-triggering control drug release.

3.2 Introduction

Polymeric micelles have long been studied for decades yet still gain a lot of interest for drug delivery for a number of reasons. They improve not only physicochemical properties of the loaded-drug but also control drug release over a period of time at a particular area[1]. Several kinds of polymer have been investigated such as PLGA and PCL because of their biodegradability. However, the ability to control over the drug release triggered by external stimuli needs to be improved. Triggered-responsive materials have recently attracted a great deal of attention from researchers[2,3]. These materials better control over drug release at specific targets to maximize therapeutic outcomes and minimize adverse drug reactions from non-specific release. One of the most common methods to trigger drug release is to use temperature[4]. Most traditional thermal sensitive polymers can undergo the structural change between hydrophilic and hydrophobic parts of the polymer. Some polymers have a lower critical solution temperature (LCST) such as Poly (*N*-isopropylacrylamide, P-NIPAAM). They can undergo phase changes when heated above LCST leading to structural shrinkage and squeezing out a small molecule drug. Whereas polymers that possess an upper critical solution temperature (UCST) can swell and become more hydrophilic when the

temperature is above their UCST[2,5,6,7,8]. However, the polymer backbones of these traditional thermal sensitive polymers fail to cleave resulting in incapability of releasing nanoparticles loaded inside the micelles. The nanoparticles remain in big clusters, ≥ 100 nm in size and may obstruct deep tumor penetration[9,10,11]. To overcome high interstitial pressure and dense collagen matrix in tumor, nanoparticles with the size smaller than 50 nm are necessary[12]. As a consequence, cleavable polymeric backbone could be a promising approach to release these nanoparticles. One of the most well-known reversible chemical reactions between furan and maleimide called Diels-Alder reaction and retro Diels-Alder (rDA), was discovered in year 1928 in Germany by Professor Otto Diels and his student, Kurt Alder. This discovery results in receipt of the Nobel Prize in Chemistry in 1950[13]. In year 1994, Kuramoto et al synthesized a hydrophobic polymer by using this reaction. They used difurfuryl adipate (DFA) for the furan source and bismaleimido-diphenyl-methane (BMD) for the maleimide source[14]. After that DA reaction has been intensive studied by using different structures of furan and maleimide molecules[15]. However, Diels-Alder reaction has limited application because it requires a relatively high temperature to induce the reversible reaction. McElhanon et al, 2004 synthesized an easily removed surfactant by using 2-*N*-dodecyl hydrophobic furan and *N*-(4-hydroxyphynyl) hydrophilic maleimide[16]. This surfactant was proved useful as removable templates for the construction of microporous materials. Yamashita, 2011 made use of the maleimide-modified polyethylene glycol (Mw 20,000) to conjugate with furfuryl disulfide-gold nanorods. The high temperature induces rDA resulting in the release of polyethylene glycol from gold nanorod surface[17]. Nevertheless, to our knowledge, there is no any Diels-Alder amphiphilic block copolymer previously

synthesized before. Our group modifies the method previously published by Kuramoto to make the hydrophobic polymer backbone (DA-polymer) and we subsequently have another additional step to conjugate thiol polyethylene glycol (SH-mPEG, Mw 5,000) by using Michael addition to the hydrophobic DA polymer. After the conjugation, the thermocleavable amphiphilic block copolymer was obtained and can be self-assembly as thermocleavable micelles. This amphiphilic block copolymer has different properties from the hydrophobic Diels-Alder polymer synthesized by Kuramoto and more suitable for biomedical applications.

Iron oxide nanoparticles (IONPs) have long been used for magnetic resonance imaging (MRI), hyperthermia, and photothermal therapy (PTT)[18,19] because of their unique properties and safety. IONPs can reduce T_2 relaxation providing contrast images for the tumor areas and also generate high temperature under alternating magnetic field or NIR light treatment[20]. With these properties, IONPs could be used as diagnostic and PTT agents for cancer treatment.

We report herein the Diels-Alder amphiphilic block copolymer synthesis and its applications for controlled drug and nanoparticle release. With this novel amphiphilic block copolymer, we are able to transform the cluster nanoparticles encapsulated in the micelles to single-dispersed nanoparticles and control drug release simultaneously. The single-dispersed nanoparticles benefit deep tumor penetration. In this report, iron oxide nanoparticles (IONPs) are used as a photothermal mediator to convert near-infrared light (NIR) to heat[21,19]. The heat subsequently breaks apart the polymer backbone via retro Diels-Alder reaction (rDA)[22,23] resulting in the release of both the nanoparticles and a small molecule drug. Doxorubicin (Dox) is encapsulated into the thermo-cleavable

micelles together with IONPs. Dox was chosen as a model drug because it has been used in clinic for cancer treatment. During the process of transformation, Dox can also be released out of the micelles. This demonstrates that our thermo-cleavable polymeric micelles can generate both single-dispersed nanoparticles and control drug release at the same time leading to deeper tumor penetration and better therapeutic outcomes.

3.3 Results

3.3.1 Doxorubicin loaded in DA-b-PEO thermo-cleavable micelles.

The thermo-cleavable polymer was synthesis as previously reported in the chapter one. The molecular weight of the copolymer 8,900 Da determined by GPC. Dox and IONP (5 and 15 nm) were loaded into the polymeric micelles by a solvent evaporation method (figure 3.1). Dox was first deprotonated by trimethylamine (TEA) in DMSO. The color of the solution immediately changed. Oleic acid coated IONP (15 nm) were also co-loaded into the thermo-cleavable micelles (TCM) at the same time. The hydrophobic Dox and IONP were successfully loaded into the micelles. Loading efficiencies of Dox and IONP 15 nm are 1.7% and 3.3% respectively. Encapsulation efficiencies of Dox and IONP 15 nm are 16.7% and 32.7% respectively (Table 3.1). Hydrodynamic diameter of Dox-IO-TCM is 123.3 nm with polydispersity in (PDI) 0.518 measured by a dynamic light scattering method, and zeta potential 0.228 mV. Transmission electron microscope (TEM) images confirm the DOX-IO-TCM formation (figure 3.2). The diameter from TEM is in general smaller than the diameter measured by DLS because DLS will be affected by the interaction between the media and the

particle coated by polymer. The size of Dox-IO-TCM is very promising for passive particle delivery due to the leaky blood vessels in tumor called enhanced permeability and retention effect (EPR). EPR allows the nanoparticles with size less than 200 nm to accumulate in the tumor. The Polystyrene polyethylene oxide diblock copolymer (PS-*b*-PEO) with molecular weight 10.3 KDa was used as a non-thermo- cleavable control micelles. Both Dox and IONP (15nm) were encapsulated in the non-thermo-cleavable micelles (non-TCM) by using the similar method.

3.3.2. Photothermal induction of DOX-IO-TCM and Dox release after near infrared (NIR) laser irradiation/ high temperature treatment

We first proved that DOX-IO-TCM have a great photothermal efficiency. Dox encapsulation and polymer coating both TCM and non-TCM do not negatively impact the photothermal ability of IONP. 10 minutes after NIR laser irradiation, the surface temperature of the Dox-IO-TCM and Dox-IO-non-TCM in aqueous solution is 82.3 °C and 87.4 °C respectively, while the temperature of phosphate buffer saline (PBS) control is only 36.5 °C. The initial temperature of all samples is 29 °C. The temperatures significantly increase in both Dox-IO-TCM and Dox-IO-non-TCM compared to PBS control group (figure 3.3). We further investigated the Dox release from the micelles. After 24 minutes of NIR laser irradiation at 2.5 watts, the amount of Dox release from Dox-IO-TCM is 4-fold higher than the amount of Dox release from the TCM without NIR laser irradiation. Moreover, the amount of Dox release from the non-TCM remains no different between with and without NIR laser irradiation, which is 4-fold lower than Dox released from the TCM (figure 3.4a). The data suggest that Dox released from the non-

TCM and TCM without NIR laser irradiation results from premature release, which is very common in micelles because hydrophobic molecule can sometimes non-specifically attach to the outer layer of the micelles. This phenomenon has been observed in many kinds of polymeric particles and micelles[24–26]. We also used a dry bath as a direct heat source to trigger the TCM cleavage and Dox release. The result of the Dox-IO-TCM and Dox-IO-non-TCM exposed to the direct heat at different time points demonstrates that after Dox-IO-TCM was heat at 80 °C, 60 minutes, the amount of Dox release into the media is 3-fold higher than Dox released from non-TCM (figure 3.4b). The amount of Dox released from the non-TCM was consistent, 3-5%, and did not increase significantly over the time 0 to 60 minutes at 80 °C. In contrast, the amount of Dox released from TCM was slightly increasing from 3.79 to 7.09% after 10 and 30 minutes after the heat treatment. After the TCM were continued exposing to the heat at 80 °C, we observed the burst of the TCM and hydrophobic precipitants in the media. The amount of Dox released at 60 minutes of the heat treatment is 15.2%. It was noticed that Dox form solid aggregates with IONP in the media, whichwas difficult to extract the Dox for UV measurement; although, we used chloroform to extract the Dox from the solid complex. This observation implied that the amount of Dox release would be higher than our measurement. It is interesting that time to induce the TCM burst release is significantly shorter than using the dry bath. This observation suggests that NIR laser irradiation is more efficient to raise up the temperature and induce the retro Diel-Alders reaction of the hydrophobic backbone of the polymer. This is due to the fact that IONP can generate very high temperature on their surface and the heat

subsequently dissipate to the hydrophobic backbones of the polymer, which stay adjacent from the IONP. Therefore, the temperature at the surface of IONP is expected to be a lot higher than the temperature we observed in the media[27]. In contrast, the dry bath heats up the whole media and is not specific to the IONP so the temperatures at the surface of IONP and the media are not significantly different.

3.3.3. NIR laser irradiation induces the release of IONP from DOX-IO-TCM

We investigated whether NIR laser irradiation and high temperature treatment can induce the release of IONP from the TCM. The Dox-IO-TCM and Dox-IO-non-TCM were placed into a dry bath at 80 °C and 37 °C for 2 hours. There was no aggregate formation from both Dox-IO-TCM and Dox-IO-non-TCM after 2 hours of 37 °C treatment. This indicates that both micelles were stable at 37 °C and no IONP released to the aqueous media. However, after 2 hours of 80 °C treatment of Dox-IO-TCM, IONP and DOX aggregates were clearly formed. The Dox-IO-non-TCM still remained the same and there was no aggregate formed (figure 3.5a). We also observed the similar phenomenon when the NIR laser was used to triggered IONP release (figure 3.5b). TEM images confirmed the release of IONP from the TCM. The IONP became single nanoparticles after 2 hours of 80 °C treatment or 24 minutes after NIR laser irradiation. These data imply that the high temperature or NIR laser irradiation triggers the thermo-cleavable polymer disruption and subsequently the burst of the TCM resulting in the release of IONP at the same time with Dox. In contrast, the IONP loaded in non-TCM remained in micelle clusters after the high temperature or NIR trigger as shown in the TEM images (figure 3.6). The released IONP from the Dox-IO-TCM became single

suspended nanoparticles because the cleaved thermo-cleavable polymer, which still had the short hydrophobic part and hydrophilic PEO, can react with the released hydrophobic IONP making some of the single hydrophobic IONP suspended in the media. However, some IONP that were not coated with the cleaved polymer formed big aggregates and precipitated from the solution. The amount of the released IONP over exceeded the amount of the polymer in the system; therefore, only some of the released IONP could react with the cleaved polymer. This is the reason we observed both solid aggregates and single IONP dispersion in the solution after high temperature or NIR laser treatment.

The release of single IONP may facilitate the tumor penetration of the nanoparticles as the single IONP can penetrate deeper in the tumor mass. Huo and coworker demonstrated that gold nanoparticles with 50 nm diameters can penetrate deeper in a tumor spheroid model and accumulated more effectively in a tumor xenograft mouse model. While the gold nanoparticles with 100 nm diameter stayed around blood vessels[10]. Therefore, the released IONP from the micelle cluster may be able to penetrate deeper in the tumor mass resulting in better *in vivo* photothermal therapy.

3.4 Conclusion

The DA-*b*-PEO could be used as a thermo-cleavable polymer for triggered-drug and nanoparticle release simultaneously after triggering by NIR laser irradiation or high temperature treatment. The IONP convert the NIR laser light into heat and the heat subsequently cleaves apart the hydrophobic backbone of the thermo-cleavable polymer

by inducing the retro Diel-Alders reaction leading to the burst of the micelles. Dox and IONP release from the micelles at the same time. This could be used as a double therapy. The photothermal effect can induce cell apoptosis due to high temperature and Dox is a chemotherapeutic agent, which has been used in clinical practice. Therefore, our discovery could be useful for cancer therapy in the future. However, more detailed studies are required such as in a mouse xenograft model.

3.5 Materials and methods

Materials: furfuryl alcohol (98%), triethanolamine (TEA,99%), dioxane (99.5%, extra dry), and1,1,2,2 tetrachloro ethane (TCE,98.5%) were purchased from Acros Organics. Petroleum ether (certified ACS grade), and dichloromehane (certified ACS grade) were purchased from Fisher Scientific. Ethyl acetate (anhydrous, 99.8%), tetrahydrofuran (THF, anhydrous 99.8%), adipoyl chloride, bismaleimido diphynyl methane (BMD), and dimethyl sulfoxide (DMSO, 99.5%) were purchased from Sigma-Aldrich. Thiol methoxy polyethylene oxide 5KDa was purchased from NanoCS. Doxorubicin HCl (99.5%) was purchased from Polymed therapeutics. Polystyrene-*b*-polyethylene oxide (Ps-*b*-PEO), Mw 10,300 Da used for the control micelles was purchased from Polymer Source.

Synthesis of IONPs: 15nm IONPs were synthesized by using previously reported in the literature[19]. Briefly, a mixture of 0.890 g FeO(OH),19.8 g oleic acid and 25.0 g 1-octadecene in a three-neck flask was heated under stirring to 200°C under N_2, 30 minutes later the temperature was set at 220°C for 1 h, then the temperature was increased gradually to 310°C (20°C/5 minutes) and kept at this temperature for 1 h. The

solution became black when the temperature was increased to 320°C and kept at this temperature for 1 h. After the reaction was completed, the reaction mixture was cooled and the nanocrystals were precipitated by adding chloroform and acetone.

Synthesis of difurfuryl adipate (DFA): difurfuryl adipate was synthesized by using the previously published method by Kuramoto, 1994[14]. Briefly, adipoyl chloride was added dropwise to furfuryl alcohol in cold dioxane. The reaction continues at 0°C for 3 hours. The product was purified by column chromatography using petroleum ether and ethyl acetate (2:1) as a mobile phase. The final product was viscous brown liquid and the structure was confirmed by using H^1NMR spectroscopy.

Synthesis of cleavable hydrophobic backbone polymer, Diels-Alder polymer (DA): the DA polymer was synthesized from difufuryl adipate (DFA) and bismaleimido diphenyl methane (BMD) monomer as reported by Gandini, 2009[28]. An equimolar of DFA and BMD was mix in TCE and the reaction continued at 70°C for 9 days. The final product was precipitated in petroleum ether and characterized by using H^1NMR spectroscopy.

Synthesis thermo-cleavable polymer (DA-b-PEO) via Michael addition: the excess molar concentration of thiol-methoxy polyethylene oxide, molecular weight 5,000 Da (SH-mPEO), was added into the solution of DA polymer in DCM with a few drops of TEA. The reaction continued overnight and the product was precipitated in petroleum ether. The polymer structure was confirmed by using H^1NMR spectroscopy and molecular weight was determined by using GPC.

IONPs-loaded and Dox-IONPs loaded micelles formation: for IONPs-loaded micelles, 4mg of 15nm IONPs were mixed with 40mg of DA-*b*-PEO in 4ml THF. Then the solution was transferred dropwise into 40ml water under vigorous agitation. The solution was open to the air overnight to evaporate THF. IONP-loaded micelles were purified by centrifugation twice to get rid of free micelles. For Dox-IONPs loaded micelles, Dox.HCl was deprotonated overnight with TEA (1:2 molar ratio) in DMSO to get the hydrophobic Dox[29]. Then 4mg of hydrophobic Dox was mixed with IONPs and DA-*b*-PEO respectively in THF. The similar method with making IONP-loaded micelles and purification were used for formulating Dox-IONP loaded micelles. Polystyrene-*b*-polyethylene oxide (PS-*b*-PEO) was used for making non-thermocleavable control micelles. Encapsulation and loading efficiency of IONPs and Dox were determined by UV spectrophotometry.

Photothermal effect determination: 0.2mg/ml 15nm IONPs were used for generation of the photothermal effect from both thermo-cleavable micelles and the control micelles. 200ul of each sample were put on 96-well plate and were exposed to the NIR laser 885nm, 2.5W/cm^{2}with 5x8mm spot size. Phosphate buffer saline was used as a control. The temperature was measured by thermal camera.

Dox release determination: After the samples were either heated at 80°C or exposed to NIR light, the released Dox was extracted by using 200ul of chloroform. Subsequently, the chloroform layer was taken and evaporated overnight. Dox powder was

reconstituted in DMSO and the amount of released Dox was measured by UV spectroscopy.

3.6 Acknowledgements

Other people who contribute in this work include Dr. Hongwei Chen and Dr. Duxin Sun.

We acknowledge Molecular Imaging Laboratory for transmission electron microscope.

We also thank Dr. Jinsang Kim lab for GPC.

This work has been submitted for U.S. provisional application Ser. No. 62/043,648.

3.7 Reference:

1. Rösler, A., Vandermeulen, G. W. M. & Klok, H.-A. Advanced drug delivery devices via self-assembly of amphiphilic block copolymers. *Adv. Drug Deliv. Rev.* **64,** 270–279 (2012).
2. Fitzpatrick, S. D., Fitzpatrick, L. E., Thakur, A., Mazumder, M. a J. & Sheardown, H. Temperature-sensitive polymers for drug delivery. *Expert Rev. Med. Devices* **9,** 339–51 (2012).
3. Wei, H., Zhuo, R.-X. & Zhang, X.-Z. Design and development of polymeric micelles with cleavable links for intracellular drug delivery. *Prog. Polym. Sci.* **38,** 503–535 (2013).
4. Cellesi, F. Mini Review Thermoresponsive hydrogels for cellular delivery. *Ther. Deliv.* **3,** 1395–1407 (2012).
5. Ward, M. a. & Georgiou, T. K. Thermoresponsive Polymers for Biomedical Applications. *Polymers (Basel).* **3,** 1215–1242 (2011).
6. Blanco, E., Kessinger, C. W., Sumer, B. D. & Gao, J. Multifunctional micellar nanomedicine for cancer therapy. *Exp. Biol. Med. (Maywood).* **234,** 123–31 (2009).
7. Wei, H.-L., Yang, Z., Zheng, L.-M. & Shen, Y.-M. Thermosensitive hydrogels synthesized by fast Diels–Alder reaction in water. *Polymer (Guildf).* **50,** 2836–2840 (2009).
8. Strong, L. E. & West, J. L. Thermally responsive polymer-nanoparticle composites for biomedical applications. *Wiley Interdiscip. Rev. Nanomed. Nanobiotechnol.* **3,** 307–17 (2011).
9. Minchinton, A. I. & Tannock, I. F. Drug penetration in solid tumours. *Nat. Rev. Cancer* **6,** 583–92 (2006).
10. Huo, S. *et al.* Superior penetration and retention behavior of 50 nm gold nanoparticles in tumors. *Cancer Res.* **73,** 319–30 (2013).
11. Cabral, H. *et al.* Accumulation of sub-100 nm polymeric micelles in poorly permeable tumours depends on size. *Nat. Nanotechnol.* **6,** 815–23 (2011).
12. Wong, C. *et al.* Multistage nanoparticle delivery system for deep penetration into tumor tissue. *Proc. Natl. Acad. Sci.* **108,** 2426–2431 (2011).
13. Nicolaou, K. C., Snyder, S. a, Montagnon, T. & Vassilikogiannakis, G. The Diels--Alder reaction in total synthesis. *Angew. Chem. Int. Ed. Engl.* **41,** 1668–98 (2002).
14. Kuramoto, N., Hayashi, K. & Nagai, K. Thermoreversible reaction of diels—alder polymer composed of difurufuryladipate with bismaleimidodiphenylmethane. *Polym. Sci.* 2501–2504 (1994). at <http://onlinelibrary.wiley.com/doi/10.1002/pola.1994.080321312/abstract>
15. Gandini, A. The furan/maleimide Diels–Alder reaction: A versatile click–unclick tool in macromolecular synthesis. *Prog. Polym. Sci.* **38,** 1–29 (2013).

16. McElhanon, J. R. *et al.* Thermally cleavable surfactants based on furan-maleimide Diels-Alder adducts. *Langmuir* **21,** 3259–66 (2005).
17. Yamashita, S. *et al.* Controlled-release system mediated by a retro Diels-Alder reaction induced by the photothermal effect of gold nanorods. *Langmuir* **27,** 14621–6 (2011).
18. Gupta, A. K. & Gupta, M. Synthesis and surface engineering of iron oxide nanoparticles for biomedical applications. *Biomaterials* **26,** 3995–4021 (2005).
19. Chen, H. *et al.* Highly crystallized iron oxide nanoparticles as effective and biodegradable mediators for photothermal cancer therapy. *J. Mater. Chem. B* **2,** 757 (2014).
20. Tian, Q. *et al.* Multifunctional polypyrrole@fe3 o4 nanoparticles for dual-modal imaging and in vivo photothermal cancer therapy. *Small* **10,** 1063–8 (2014).
21. Chu, M. *et al.* Near-infrared laser light mediated cancer therapy by photothermal effect of Fe3O4 magnetic nanoparticles. *Biomaterials* **34,** 4078–88 (2013).
22. Gandini, A. Progress in Polymer Science The furan / maleimide Diels – Alder reaction : A versatile click – unclick tool in macromolecular synthesis. *Prog. Polym. Sci.* **38,** 1–29 (2013).
23. Gandini, A., Coelho, D. & Silvestre, A. J. D. Reversible click chemistry at the service of macromolecular materials. Part 1: Kinetics of the Diels–Alder reaction applied to furan–maleimide model compounds and linear polymerizations. *Eur. Polym. J.* **44,** 4029–4036 (2008).
24. Chen, H. *et al.* Release of hydrophobic molecules from polymer micelles into cell membranes revealed by Forster resonance energy transfer imaging. *Proc. Natl. Acad. Sci. U. S. A.* **105,** 6596–6601 (2008).
25. Hyeon, T. & Rotello, V. Nanomedicine themed issue and therapy w. *Chem. Soc. Rev.* **41,** 2545–2561 (2012).
26. Oerlemans, C. *et al.* Polymeric micelles in anticancer therapy: Targeting, imaging and triggered release. *Pharm. Res.* **27,** 2569–2589 (2010).
27. Horiguchi, Y., Honda, K., Kato, Y., Nakashima, N. & Niidome, Y. Photothermal reshaping of gold nanorods depends on the passivating layers of the nanorod surfaces. *Langmuir* **24,** 12026–12031 (2008).
28. Gandini, A., Coelho, D., Gomes, M., Reis, B. & Silvestre, A. Materials from renewable resources based on furan monomers and furan chemistry: work in progress. *J. Mater. Chem.* **19,** 8656 (2009).
29. Kim, D., Lee, E. S., Park, K., Kwon, I. C. & Bae, Y. H. Doxorubicin loaded pH-sensitive micelle: antitumoral efficacy against ovarian A2780/DOXR tumor. *Pharm. Res.* **25,** 2074–82 (2008).

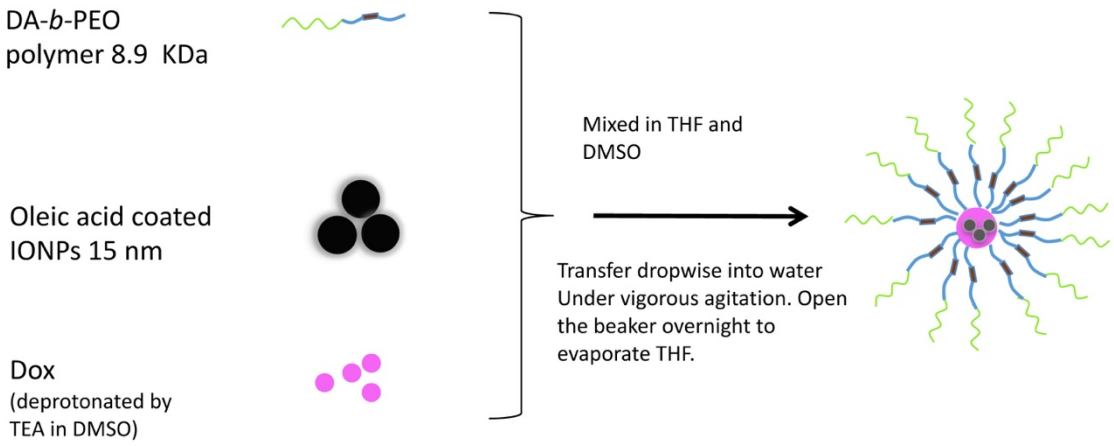

Figure 3.1. A The schematic picture demonstrates the DOX-IO-TCM formation. The hydrophobic part of the thermo-cleavable polymer entraps hydrophobic molecules such as Dox and IONPs, The hydrophilic one assembly as shells, which helps increase solubility and prolongs blood circulation time in the body. Both IONPs and Dox are spontaneously encapsulated into the hydrophobic core of the micelles. Dox- IONP loaded non thermo-cleavable micelles (Dox-IO non TCM) was produced with the similar method to Dox-IONP loaded TCM; however, PS-*b*-PEO was used instead of DA-*b*-PEO.

SAMPLES	DOX-IO-TCM (%)	DOX-IO-NON-TCM (%)
EE of Dox	14.4	7.3
LE of Dox	1.4	0.7
EE of IONPs	32.7	43.5
LE of IONPs	3.3	4.3

Table 3.1. The table shows encapsulation and loading efficiency of DOX-IO-TCM and DOX-IO-NON-TCM.

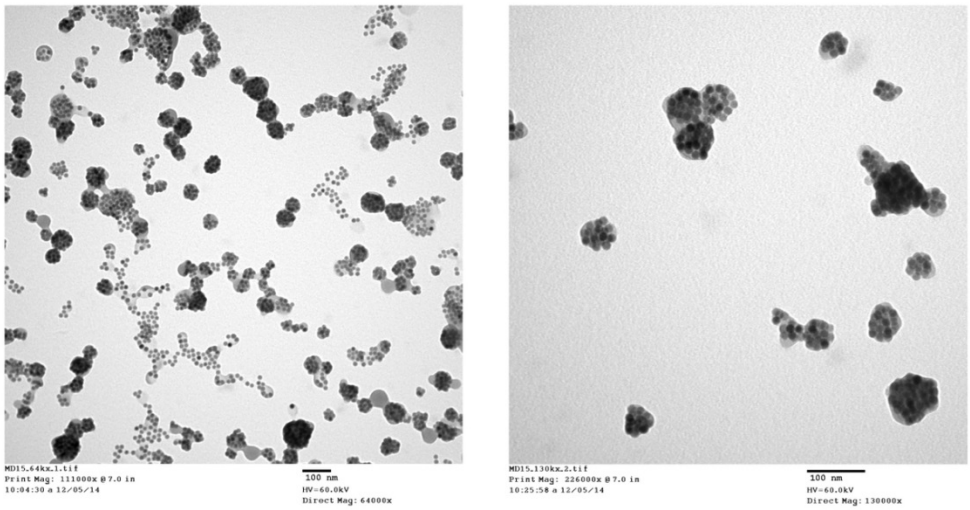

Figure 3.2. TEM images of DOX-IO-TCM at low magnification and high magnification confirms that Dox and IONP were successfully encapsulated in the micelles.

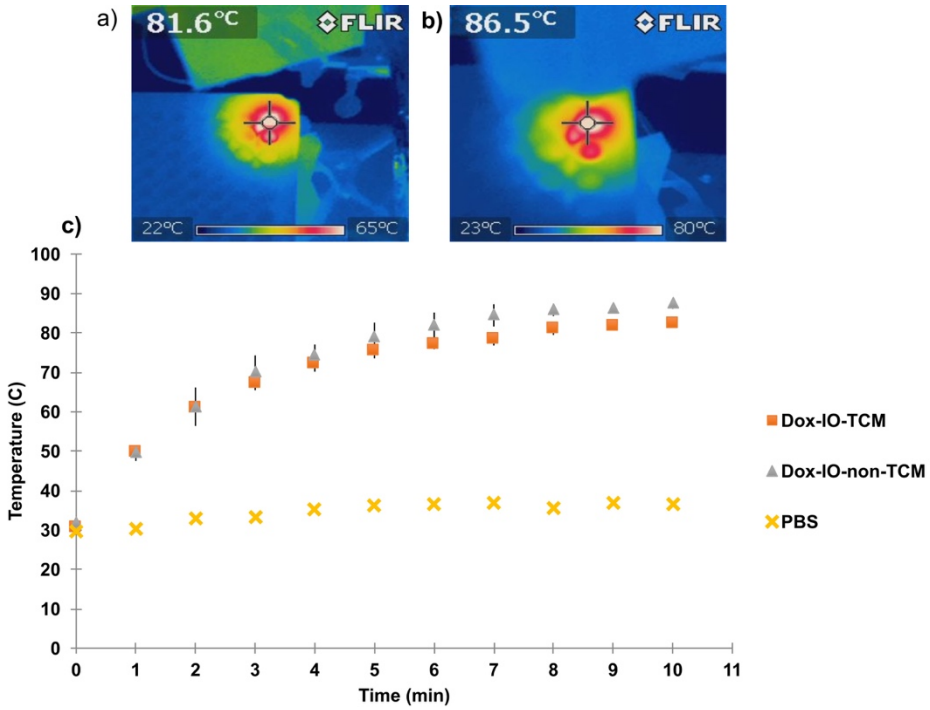

Figure 3.3. a) and b) the images show the final temperatures of the Dox-IO-TCM and Dox-IO-non-TCM in PBS solution. The temperatures were measured by a thermal camera. c) The graph shows the temperature increases of Dox-IO-TCM, Dox-IO-non-TCM, and PBS control. The initial temperatures of all samples are 29 °C. 10 minutes after NIR laser irradiation 2.5W , the temperatures of Dox-IO-TCM and Doc-IO-non-TCM increase to 82.3 °C and 87.4 °C respectively, while the final temperature of PBS control increases to only 36.5 °C. The data suggest that the polymer used for micelle encapsulation and Dox do not affect the photothermal efficiency of IONP. The experiments were done in triplicates.

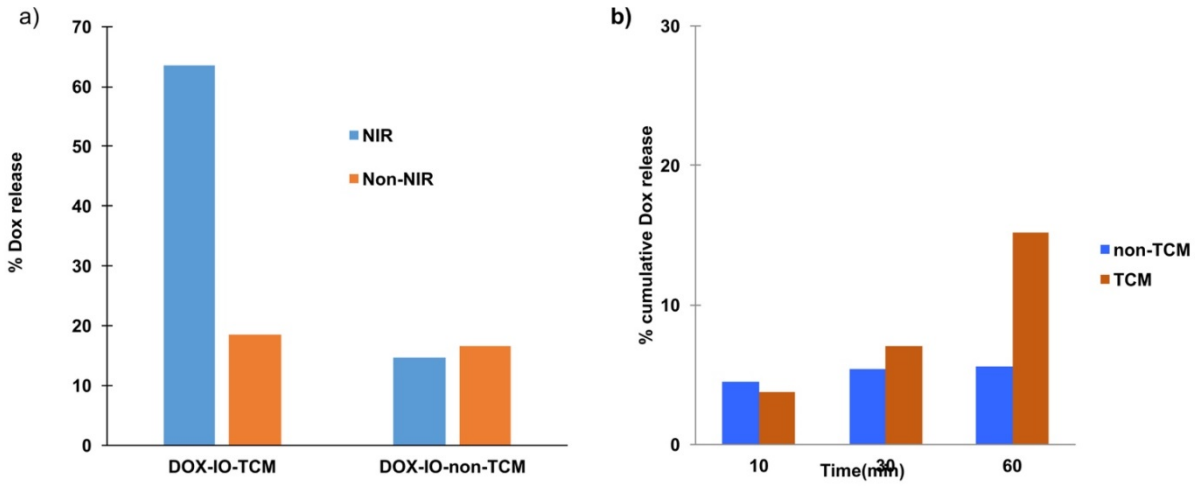

Figure 3.4 a) The chart demonstrates the percent of Dox released from Dox-IO-TCM and the control micelles, Dox-IO-non-TCM with and without 24 minutes of NIR laser trigger (2.5 W), 885 nm. NIR laser can trigger the Dox release from TCM and Dox was released 4-fold higher than NIR laser trigger for the non-TCM and 3.43 fold higher than TCM without laser trigger. There is no difference in non-TCM between with and without NIR laser irradiation. b) The percent of cumulative Dox release at different time points after the TCM and non-TCM were exposed to the high temperature at 80 °C. Dox- from TCM has a burst release at one hour after being treated at 80 °C, while non-TCM still have low Dox release.

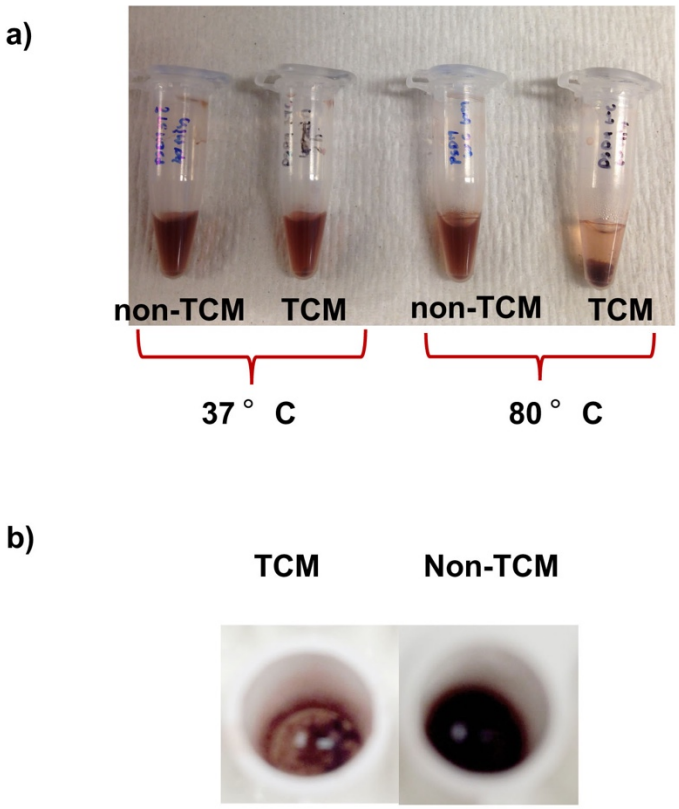

Figure 3.5 External triggers induce micelles dissociation for controlled drug release application. Both Dox-IONP loaded TCM and non-TCM are stable at 37°C. There is no aggregate formed after 2 hours of 37°C exposure (a, left). In contrast, after 2 hours of 80°C treatment, Dox-IONP loaded TCM are ruptured and release the payload as the big aggregates are obviously formed. The aggregates are the hydrophobic residues of the thermo-cleavable polymer, Dox, and unencapsulated IONPs. There is no aggregates formed from non-TCM; even thought, they are exposed to the same temperature with the TCM (a, right). Both Dox-IONP loaded TCM and non-TCM are also exposed to NIR laser for 24 minutes to examine the NIR-induced drug release (b). After NIR laser trigger, Dox-IONP loaded TCM form big aggregates similar to the heat treatment at 80°C, while there is no significant change in Dox-IONP loaded non-TCM. This indicates the non-TCM are insensitive to the high temperature and NIR laser triggers as well as incapability of releasing the payload. It is explained that the TCM release Dox and IONPs by temperature-induced Diels-Alder reaction resulting in the cleavage of the cycloadduct in the hydrophobic backbone of the polymer. Moreover, this also indicates that both high temperature and NIR light can be used as external stimuli for controlled drug release from our TCM.

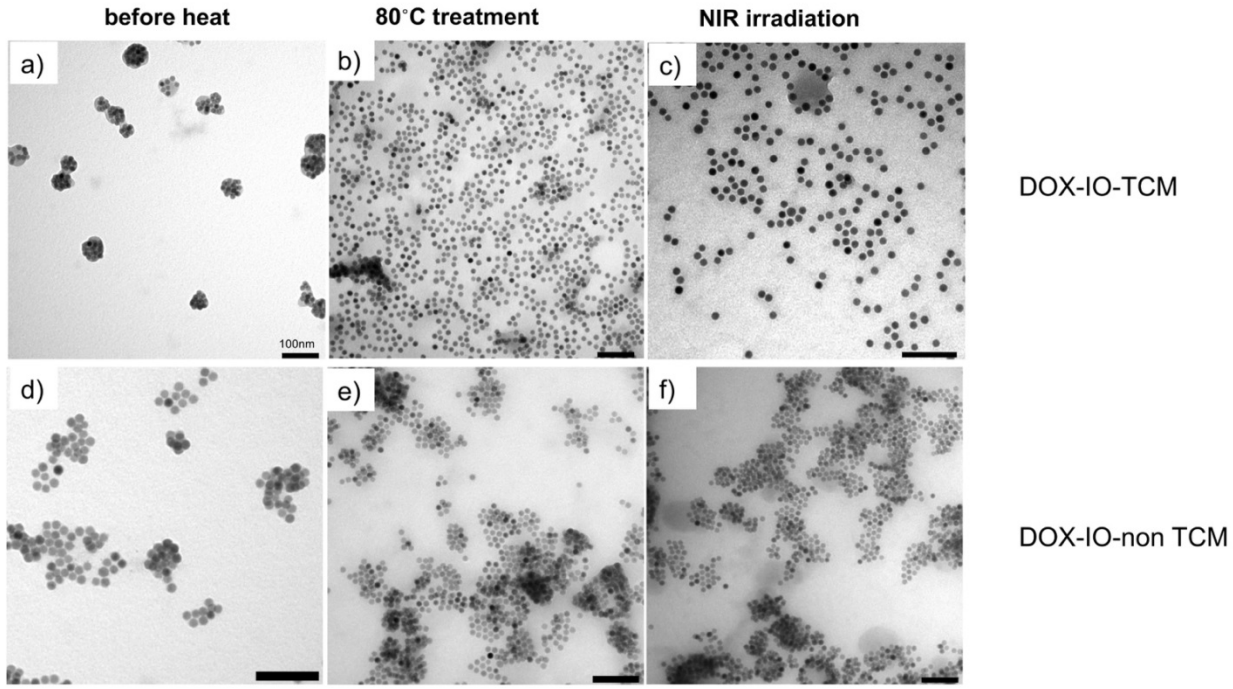

Figure 3.6. TEM image of the Dox-IONPs loaded thermo-cleavable micelles before (A), after temperature trigger at 80°C (B), and NIR laser irradiation (C). Figure A shows that IONPs form micelle-like clusters. In contrast, after 80°C or NIR laser exposure, Dox-IONPs loaded thermo-cleavable micelles loss the micelle-like structure and become single-dispersed IONPs as shown in figure B and C. (D) shows Dox-IONPs loaded non-thermocleavable micelles, control micelles. However, non-TCM remain their micelle-like structure after 80°C (E) or NIR laser exposure (F). This confirms that our TCM can be cleaved and reattach back to make the single-dispersed IONP micelles.

CHAPTER 4

ENGINEERING HPV ANTIGENIC-PEPTIDES AND ADJUVANT CONJUGATED NANOSATELLITE VACCINE FOR HEAD AND NECK CANCER TREATMENT

4.1 Abstract

Head and neck squamous cell carcinoma (HNSCC) is one of the most common cancers worldwide. Previously, the main cause of HNSCC had been smoking and alcohol consumption but in recent years there has been a shift towards initiation by HPV infection in the last decade due to changes in sexual behavior. While there are vaccinations for cervical HPV cancers, there are no specific treatments for the HPV-positive HNSCC. Current treatment regimens are identical for HPV-positive and HPV-negative HNSCC. Although anti-PD-L1 antibody was approved for this indication, the clinical response rate of HNSCC to immunotherapy is generally below 20%. A strategy for treating hypoimmunogenic tumors is lacking. Thus, new strategies are needed for treating hypoimmunogenic tumors. We propose to boost anti-tumor immunity against the HPV-positive HNSCC using an inorganic nanoparticle-based vaccine to deliver E7 and E6 HPV antigenic peptides and cGAMP, a small molecular adjuvant, to professional antigen presenting cells. The nanosatellite particles enhance the peptide density, promote the cellular uptake, and prevent rapid in vivo clearance of the antigenic peptide

and adjuvant. We found that our nanosatellite vaccine induces IFN-I production and promotes tumor antigen-specific CD8+ T cells that led to reduced tumor burden.

4.2 Introduction

Head and neck cancer is a type of malignant tumors that develop in or around head and neck areas such as the throat, larynx, oral cavity, nasal cavity, and oropharyngeal area[1]. 90% of the head and neck cancer have been considered as squamous cell carcinomas[2]. Head and neck squamous cell carcinoma (HNSCC) is one of the most common cancers worldwide and in the United States 5% of all cancer patients have been diagnosed as HNSCC. There are 11.9% new case arising globally in year 2012 with 4.5% death rate in all cancers[2–4]. Classic risk factors of HNSCC development are tobacco and alcohol consumption; however, the trend of pathogenesis of HNSCC is shifting from the classic risk factor to human papiloma virus (HPV) infection due to altered sexual behavior[5]. HPV has become a major underlining cause of HNSCC in men, accounting for 2/3 of the HNSCC patients. The current incident rate of HPV^+ HNSCC is highest among young white male population. Interestingly, according to Center for Disease Control and Prevention (CDC), the incident rate of HPV16/18 positive HNSCC in men is as high as the incident rate of HPV 16/18 positive cervical cancer in women. Moreover, it is predicted that, by year 2020, the incident rate of HPV-positive HNSCC will surpass the incident rate of HPV-positive cervical cancer[6,7]. Regardless of the underlining causes of HNSCC, the same standard of care are used, such as surgery, ionizing radiation, chemotherapy, or adjuvant therapy[8].

Immunotherapy has been recently entered clinical used for HNSCC treatment. Food and Drug Administration (FDA) has approved anti-PD-L1 antibody used for HNSCC treatments in United State in 2016 after clinical trials demonstrated the better prognosis and higher survival rate than the standard therapy without the anti-PD-L1 combination[9–11]. Nevertheless, only 20% of HNSCC patients respond to the immunotherapy treatment[9–12]. This implies that only the checkpoint blockade against T cell exhaustion is not sufficient for HNSCC treatments. HNSCC is considered a hypoimmunogenic tumor, which is more resistant to effector immune cells and often fails to elicit tumor antigen (TA)-specific cytotoxic T lymphocytes (CTLs). Unfortunately, current HPV vaccines used for HPV16/18 cervical cancer prophylaxis have been neither approved for HPV16/18 HNSCC nor cervical cancer treatment by FDA. Therefore, the need of HPV-positive HNSCC treatment is still unmet. One of the most promising strategies to treat this disease is to boost hosts' anti-tumor immunity and to generate a T cell-inflamed tumor microenvironment. Type I interferon (IFN-I) has been known to be a key player of innate immunity to elicit antigen presenting cells (APC) and maintain an effective anti-tumor immune response[13].

There are several approaches to promote type I IFN against tumors. Cyclic dinucleotides (CDNs) such as cyclic GMP-AMP (cGAMP) have been known to activate the adaptor protein stimulator of interferon genes (STING), which promotes IFN-I induction[14–16]. It is promising to utilize the cGAMP as a potent adjuvant in HNSCC vaccine to promote T cell inflamed tumor microenvironments. CDNs have demonstrated profound tumor regression in melanoma after intratumoral injection to

immunocompetent mice[17,18]. However, intratumoral delivery is not favorable in clinical applications. The fact that cGAMP is a hydrophilic small molecule, which has rapid clearance from the body before they reach the targets, hampers it from being used in clinics. Nanotechnology can offer solution to solve this problem. Similar to the cGAMP adjuvant, HPV antigenic peptides also require an effective delivery system to reach the targets for antigen cross-presentation to T cells in lymph nodes. E6 and E7 protein have been well reported as HPV oncoproteins, which impair the function of tumor suppressor proteins such as p53 and pRB[19,20]. These two oncoproteins have become great targets of the vaccine to boost specific T cell activity against HPV-positive HNSCC because they are absent in normal host cells. E6 and E7 epitopes are soluble peptides, which have rapid diffusion and degradation in physiological conditions. Therefore, they are not suitable to use alone as a synthetic peptide vaccine. A peptide conjugation with nanoparticles can help minimize the clearance and degradation of the soluble peptides. Importantly, both adjuvant and the antigenic peptides need to be able to escape from the lysosome and go to cytosol in order to stimulate downstream cascades for type I IFN production and loaded onto major histocompatibity complex (MHC) class I[21,22].

One of the alternatives is to deliver tumor antigenic peptides and adjuvants to stimulate APC resulting in T cell cross-priming. To effectively deliver the antigenic peptides and adjuvants to APC *in vivo*, nanocarriers must be properly designed. Size, shape and surface area are critical factors for engineering vaccine carriers[23]. It has been well-known that nanoparticles deliver antigens more effectively than microparticles due to the limitation of APC uptake[24]. Previous reports show that dendritic cells prefer to

uptake nanoparticles, which have around the same size with virus (< 200 nm) and the optimal size for cell uptake is around 50 nm [25–27]. Moreover, nanocarriers at this size can travel to lymph nodes directly or take advantage of APC-facilitated trafficking to lymph nodes, where APC can cross-present the antigen to T cells and consequently activate specific immune response against the tumors[28,29]. Ligand density on the nanoparticles is also another important aspect needed to be considered for vaccine design. Higher ligand density conjugated on the surface of nanoparticles elicits stronger immune response and cytokine release[30,31]. These aspects prompt us to engineer nanosatellite particles used for delivering the E6/E7 antigenic peptides and cGAMP adjuvant to the APC to promote type I IFN production and activate specific T cell immune response against HPV-positive HNSCC.

The nanosatellite particles are composed of two types of inorganic materials with iron oxide nanoparticles as a core surrounded by small gold nanoparticle satellites[32]. This core-satellites system enhances overall surface area of the particles for the peptides conjugation resulting in the higher local peptide density. The externally conjugated peptides on the surface of the particles promote B cell activation better compared to the antigen trapped inside the polymeric or liposomal nanoparticles. Moreover, nanosatellite particles are biodegradable and biocompatible. The iron oxide core can be degraded in the lysosome of splenic and hepatic macrophages to become ferric and ferrous, which are endogenous substances and then recycled in a form of hemoglobin[33,34]. While, gold nanoparticles with the diameter less than 6 nm regardless of surface charge can be excreted out of the body through the renal clearance[35,36].

These physicochemical properties offer advantages for the vaccine carriers. We consequently engineered the nanosatellite vaccine carrying E6/E7 oncogenic peptides and a small molecule adjuvant, cGAMP and investigated the efficacy of the nanosatellite vaccine to promote innate immunity and specific T cell activation for HPV-positive HNSCC treatments both *in vitro* and *in vivo*.

4.3 Results and discussion

4.3.1 Nanoparticle synthesis and characterizations

Nanosatellite particles were synthesized as previous reported[37]. Briefly, iron oxide nanoparticles coated with poly (γ- methacryloxypropyl trimethoxysilane) -*b*- poly (ethylene oxide) polymer (MPS-*b*-PEO) were homogeneously mixed with gold sulfide nanoparticles (AuS) at different ratios. Average diameter of AuS nanoparticles is *ca* 2-4 nm measured by transmission electron microscopy (TEM). Silane functional group of the MPS-*b*-PEO polymer strongly anchors on the surface of iron oxide nanoparticle, while thiol functional group on the polymer can covalently bind to the surface of gold nanoparticles. The number of gold nanoparticles on an iron oxide core is adjustable by molar ratios of gold and iron oxide nanoparticles (figure 4.1a-f). The number of AuNP is proportionally increasing when the higher volume of AuNP solution was added (figure 4.1 g-i). However, the higher ratios of AuNP/IONP core compromise the stability of the nanosatellite particle overall because the excessive amount of AuNP causes the crosslinking between nanosatellite particles, resulting in precipitation. Our data suggest that the ratio of Fe 1 mg: AuNP 3 ml provides the decent numbers of AuNP/IONP core, which are approximately 10 AuNP/IONP. From a mathematic calculation, the distance

between each AuNP is 10 nm. The solution remains stable over a month at 4°C (figure 4.2 a and b).

We further conjugate modified E7 and E6 oncogenic peptides on the surface of the nanosatellite particles via maleimide-thiol chemistry called Michael addition (scheme 1). Acetylthio-PEG5K-Maleimide was used to conjugate with thiol-modified E7 R9F or E7 Q19D peptide. The formed thioether bonds are stable and non-reversible, which is suitable for peptide delivery. The acetyl-PEG-E7 was deacetylated to yield free thiol functional groups before further conjugation with the nanosatellite particles. The E7 conjugated nanosatellites were purified by a magnet separator to eliminate the unbound peptide and PEG linkers. The supernatant was collected and used for determining E7 conjugation efficiency. We performed similar work for the modified E6 peptide. The conjugation efficiency is 92% measured by Lavapep (figure 4.2 c). There are approximately 1,000 peptide/Au satellite and 10,000 peptide/whole structure. The peptide-conjugated nanosatellites were next loaded with cyclic guanosine monophosphate- adenosine monophosphate (cyclic GMP-AMP, cGAMP) as a potent adjuvant. cGAMP was spontaneously associated with the peptide-conjugated nanosatellites in phosphate buffered saline solution (PBS) due to the electrostatic interaction between highly positive charged peptides and negative charged cGAMP. Hydrodynamic diameter of the nanosatellites increases from 64.49 nm to 83.79 nm after the E7 and E6 peptide conjugations and 99.31 nm after being loaded with cGAMP (figure 4.2 d). Zeta potentials were also dramatically changed after peptide and cGAMP conjugation. The nanosatellites carry negative charges due to the AuNP. The zeta

potential of nanosatellites was -30.8 mV and became 10.6 mV and -4.2 mV after peptide conjugation and cGAMP loading respectively (figure 4.2 e). These data also confirmed the successful peptides and cGAMP loaded on the nanosatellites.

4.3.2 Nanosatellite vaccine enhances antigen uptake, induces ISRE promoter activity and upregulation of type I IFN-related genes *in vitro.*

We first explored whether the nanosatellite can enhance the uptake of the antigenic peptide to APC *in vitro*. The E7 R9F peptides were labeled with a fluorescent dye FAM. The E7-FAM conjugated with the nanosatellites, free E7-FAM and PBS control were incubated with bone marrow-derived macrophages (BMM) for 2 and 6 hours. The data clearly show that nanosatellites increase the BMM uptake of the E7 antigenic peptides compared to the free peptides (figure 4.3a). The higher APC uptake positively impacts interferon (IFN) promoter activity and upregulation of type I IFN related genes in immune cells. We performed IFN-stimulated response element (ISRE) assay using interferon reporter human monocytes (THP1-Blue), which are able to produce alkaline phosphatase in a proportion to the amount of IFN stimulation received from external triggers. The level of IFN promoter activity was then determined by a colorimetric enzyme assay of alkaline phosphatase (Quanti-Blue). 10μg/ml cGAMP with or without the nanosatellite vaccine conjugation and other controls were incubated with THP1-Blue cells for 16 hours and the supernatants were collected to quantify the interferon regulatory factor (IRF)-inducible alkaline phosphatase. Data shows that the nanosatellite vaccine effectively induced ISRE promoter activity in monocytes (26.4-

fold) compared to cGAMP alone (18.9-fold) higher than PBS. Nanosatellite particles themselves did not show the stimulation of ISRE promoter activity (figure 4.3b). The effective intracellular delivery of cGAMP was also confirmed by the dose-dependent higher mRNA levels of type 1-IFN –related genes such as *IFNA4, IFNB1, ISG15, ISG54, CXCL9*, and *CXCL10* compared to cGAMP alone. The nanosatellite vaccine at the dose of 10μg/ml cGAMP enhances the level of mRNA of *IFNA4* (105-fold), *IFNB1*(74-fold), *ISG15* (8-fold), *ISG54* (39-fold), *CXCL9* (2,245-fold), and *CXCL10* (20,177-fold), while cGAMP alone at the same dose increases the level of mRNA only 16, 37, 5, 22, 488, and 2,160-fold respectively (figure 4.3 c-h). This implies that our nanosatellites facilitate the intracellular delivery of cGAMP adjuvant. Our discovery agrees with previous report that nanoparticles can promote small molecules internalization[38,39]. To stimulate the mRNA production of the IFN-related genes in nucleus, cGAMP must first be delivered to cytosol and bind to STING ligand in the endoplasmic reticulum (ER). This suggested that cGAMP can escape from endo-lysosome to cytosol and bind to the STING ligand in endoplasmic reticulum (ER)[14,16]. cGAMP can dissociate from the peptide-conjugated nanosatellites due to pH change. cGAMP is negatively charged at pH 7.4 but switches to a net positive charge under the acidic pH in endo-lysosome resulting in dissociation from the peptide-conjugated nanosatellites complex and endosomal escape[40].

4.3.3 Nanosatellite vaccine promotes dendritic cell maturation and IFNβ secretion from APC *in vitro*.

We next investigated the ability of our nanosatellite vaccine on the promotion of dendritic cells (DC) maturation, which is a key step for T cell activation. The nanosatellite vaccine, cGAMP alone, peptide alone, nanosatellite particles alone were incubated with bone marrow derived dendritic cells (BMDC) for 48 hours. The cells were harvested and then stained with the maturation markers, CD86 and MHC-II and analyzed by flow cytometry. Data show that the nanosatellite vaccine better promoted the DC maturation compared to other controls (figure 4.4 a-d). It is possible that the nanosatellites delivered cGAMP to BMDC better than cGAMP alone. Although the mechanism of cGAMP cellular uptake remains unknown, cGAMP itself is a small molecule with negative charges, which is not preferable for the cell to uptake. DC maturation is a key step in the generation of potent immune responses because the mature DC will become more functional and release many inflammatory cytokines to trigger immune cascade to cope with antigens. Mature DC can efficiently process antigenic peptides and cross-present the peptide epitope onto MHC-I for further priming the $CD8^+$ T cell response[21,25].

We also examined the IFNβ production in murine bone-marrow derived macrophages using ELISA. The data also confirm the efficacy of the nanosatellite vaccine on type-I IFN production in a dose-dependence (figure 4.4 e).

4.3.4 Nanosatellite vaccine travels to lymph nodes in *in vivo* model

It is crucial for the vaccine to efficiently travel to lymph node where the DC present the antigenic peptides and activate CD8+ T cells [41]. We took the advantage of the present of iron oxide nanoparticles in our vaccine to visualize vaccine biodistribution in lymph nodes. It is well-documented that iron oxide nanoparticles can lower T_2 relaxation time and darken the magnetic resonance (MR) images[42,43]. MR images clearly show that 4 hours post subcutaneous injection of the nanosatellite vaccine at tail base of C57BL/6 mice, the inguinal and popliteal lymph nodes became darker and the vaccine remained in the lymph nodes longer than 24 hours after injection (figure 4.5). Our nanosatellite vaccine can accumulate in the lymph node within 4 hours after S.C injection implying that the vaccine enters the lymphatic system directly rather than be uptaken by APC initially because it generally takes approximately 24 hours for APC to arrive lymph nodes[21,44]. Moreover, the longer the resident time of the vaccine in the lymph node, the higher the chance for naïve T cells to come to contact with the DC, which would result in more robust T cell activation[45]. This perspective justifies the use of nanoparticle for antigenic peptide and small molecule adjuvant delivery. The nanosatellite vaccine can carry the peptides to the lymph nodes and promote the T cell activation, while soluble peptides may not be able to reach the lymphatic system or rapidly eliminated out of the body resulting in low immune response.

4.3.5 Nanosatellite vaccine suppressed tumor growth and boost E7-specific anti-tumor immunity in a mouse xenograph model

After the nanosatellite vaccine demonstrated a great efficacy *in vitro*, we continued investigating the efficacy of the vaccine for tumor suppression *in vivo*. 0.4 x 10^6 cells of MOC2, mouse oral cancer cell line, were subcutaneously implanted into the neck of C57B/6 mice on day zero. The mice were treated with PBS, cGAMP alone, or the nanosatellite vaccine (vaccine R9F), 3 weekly doses (figure 4.6a). The mice treated with the nanosatellite vaccine R9F on day 25 show significant smaller tumor burden than the mock and other control treatments (figure 4.6b). The tumors were harvested for type I IFN-related genes and E7- specific T cell activation studies. The nanosatellite vaccine R9F potently promoted the production of *ifna4* and *ifnb1* (figure 4.6c), which is in a good agreement with our *in vitro* assay. cGAMP showed some weak effect on the type I IFN and tumor suppression due to the rapid degradation. To investigate the E7-specific T cell response, tumor infiltrating lymphocytes (TIL) were isolated from the tumors using ficoll gradient centrifugation[46]. TIL were then stained with a tetramer recognizing H-2D^b-restricted HPV16 E7 epitope RAHYNIVTF and analyzed by flow cytometry. Interestingly, the vaccine dramatically improved the percentage of E7-specific CD8$^+$ T cells compared to the PBS and cGAMP treated groups (figure 4.6d).

To improve the efficacy of the nanosatellite vaccine in tumor suppression, we further replaced the E7 R9F peptide with E7 Q19D (Vaccine Q19D), which has longer sequence of amino acids. The mice were vaccinated, or received E7 Q19D/E6 peptides alone, cGAMP alone, anti PD-L1 antibody alone or a mock treatment. The treatments

were started 3 days after tumor implantation and the mice received vaccine Q19D, cGAMP, peptides, PBS once a week for 3 weeks or received anti PD-L1 intraperitoneally twice a week for 3 weeks (figure 4.7a). The data show that vaccine strongly suppressed tumor growth compared to other treated groups. It was observed that after the second vaccination, the tumor burden started to diminish, while the tumors in other groups progress quickly (figure 4.7 b and d). The tumor volumes of the vaccinated mice were 6.3 times smaller than the mice that received the mock treatment and 3.6 times smaller than those received the cGAMP as an adjuvant alone on day 21. Anti PD-L1 antibody and E7/E6 peptides failed to suppress the tumor growth (figure 4.7 b and d). Moreover, the vaccinated mice showed the better survival rate compared to other control groups. The medians of survival were 31, 28, and 21 days in the vaccinated, cGAMP-treated, and other groups respectively (figure 4.7c).

We also performed real-time PCR and FACs from tumor tissues and TILs to prove the effect of the nanosatellite vaccine Q19D. Similar to our previous data, the nanosatellite vaccine Q19D exhibited the strongest type I IFN production compared to other group of treatments (figure 4.8 a-b). Flow cytometry analysis of TILs demonstrated that the nanosatellites vaccine Q19D robustly activated E7-specific $CD8^+$ T cells (figure 4.8 c-d). This confirms that the nanosatellite vaccine successfully delivered the E7/E6 antigenic peptides and cGAMP to the APC. It is assumed that E7/E6 peptides bound with the gold satellites by Au-thiol covalent bonding could be cleaved by glutathione inside the lysosomes and escape to the cytosol after the cell uptake[47]. These APC

subsequently cross-presented the peptides to $CD8^+$ T cells. These primed cytotoxic T lymphocytes (CTL), which can eliminate the E7/E6 overexpressed tumors robustly.

We further investigated the effect of the nanosatellite vaccine on a resistant mouse oral cancer cell line overexpressing SOX2 oncogenic protein, which dampens the type I interferon by increasing the degradation of STING protein. The treatment schedule remains the same with the previous study (figure 4.9 a). The data show that the combination therapy between the nanosatellite vaccine (Q19D) and anti PD-L1 antibody is very effective on SOX2 overexpressed tumor inhibition compared to other groups of treatments (figure 4.9 b-c). The combination treatment can strongly suppress tumor growth because of the dual mechanism. The nanosatellite vaccine promotes T cell inflamed microenvironment and directs more T cell and APC to the tumor bed, while the anti- PD-L1 antibody prevents T cell from exhaustion. The vaccine alone and anti PD-L1 antibody alone can also suppress the tumor growth at a certain level. Interestingly, the anti PD-L1 antibody seems to be more effective on SOX2 overexpressed tumor than SOX2 negative tumor in the previous experiment. It may be because the SOX2 tumor has higher level of PD-L1 than SOX2 negative tumor.

4.3.6 Nanosatellite vaccine stimulates type I IFN innate immunity to attack cancer cells *in vivo*.

We continued to explore the mechanism underlining anti-tumor effect of the vaccine. Tumor tissues were harvested for real-time qPCR assay investigating for type I

IFN-related gene regulations and for western blot analysis for proteins. It is clear that vaccine promoted the up-regulation of type I IFN mRNA levels such as *Ifnα4*, *Ifnβ1* and *Cxcl10*, which was in a good agreement with our *in vitro* study. Furthermore, western blots demonstrated that the vaccine crucially promoted the phosphorylation of tank binding kinase1 (TBK1), which is a key player in STING pathway (figure 4.10). It has been well known that cyclic di-nucleotides (CDN) bind to STING ligands and activate STING signaling through the TBK1/IRF-3 axis and subsequently induce the expression of IFN-β[14,48,49]. Our real-time PCR and western blot data suggest that the nanosatellite vaccine was uptaken by immune cells and cGAMP activated the STING/TBK1/IRF3 pathway as mentioned previously. The complex trafficked to nucleus and activated the type I IFN-related gene transcription. In contrast, cGAMP alone showed low level of mRNA and weak phosphorylated TBK1 due to mild activation on STING pathway. Because the tumor tissues were harvested two weeks after the last injection, cGAMP may already been degraded or eliminated from the body. Additionally, cGAMP is a water soluble small molecule and carries negative charges at physiological pH, which is difficult to pass lipid bilayer of plasma membrane. Moreover, the highly soluble small molecule cGAMP can diffuse from the site of administration easily and go to blood stream without entering the lymphatic system. With these characteristics, it is not feasible to use cGAMP alone as an adjuvant without effective delivery system *in vivo* regardless of their strong potency to activate STING ligand.

4.4 Conclusions

We successfully developed a potent nanosatellite vaccine composed of E7/E6 oncogenic peptides and cGAMP for HPV^+ HNSCC treatment. The peptides were conjugated on the surface of the nanosatellites with high density. *In vitro* results show that the nanosatellite vaccine promotes DC maturation determining by the expression of CD86, MHC-II, and the upregulation of type I IFN signature genes, which are required for further T cell activation. Nanosatellite particles also enhance the uptake of peptides in BMM. The nanosatellite vaccine can travel to lymph nodes after S.C injection in mice and activate immune responses to suppress the tumor growth significantly. The immunized mice showed higher type I IFN mRNA level and E7 specific T cell in tumor tissues. Therefore, this nanosatellite vaccine is a promising candidate for future HPV^+ HNSCC treatments

4.5 Materials and methods

Iron oxide(III) (FeO(OH), hydrated, catalyst grade) oleic acid (technical grade, 90%), 1-octadecene (technical grade, 90%), anhydrous tetrahydrofuran (THF, 99.8%), ammonium iron(II) sulfate hexahydrate ($Fe(NH_4)_2(SO_4)_2.6H_2O$, ACS reagent, 99%), sodium sulfide (Na_2S), Gold (III) Chloride solution (HAuCl4 in HCl), nitric acid (ACS reagent, 70%), and hydrochloric acid (ACS reagent, 37%), were purchased from Aldrich. Modified E7 (R9F) peptide (CSKKK-RAHYNIVTF), and modified E6 (Q15L) peptide (CSKKK-QLLRREVYDFAFRDL) 95% purity were purchased from Elim biopharm (USA). Acetylthio-PEG5k-Maleimide was purchased from NANOCS (USA). 2'3' cGAMP (cyclic [G(2',5')pA(3',5')p]) was purchased from Invivogen (USA).

Synthesis of nanosatellites particles

The iron oxide (IONP) core particles of the nanosatellites were synthesized by thermal decomposition as previously report[49]. The core particles were subsequently coated by a diblock copolymer (PEO-*b*-γMPS). The coating method has been previously report[50]. The coated IONP were characterized by transmission electron microscope (TEM) (Jeol 1400 plus). Gold sulfide nanoparticles (Au_2SNP) were synthesized by using sodium sulfide (Na_2S) and chloroauric acid ($HAuCl_4$) solution as a previous report[32] with slightly modifications. 2 mM $HAuCl_4$ solution was rapidly mixed with 1mM of aged Na_2S solution at the volume ratio of 7:12. The color of mixed solution immediately turned from yellow to brownish. Au_2SNP were kept in 4 °C. The Au_2SNP were characterized by TEM. To

fabricate the nanosatellite particles (NS), 1mg Fe of IONP (15nm) were added into 3 ml of Au_2SNP (2nm) solution and mixed homogenously incubated on a rocking platform for 30 minutes and stored at 4 °C. The nanosatellite solution was filtered by 0.45 μm syringe filter before used.

Gold and iron concentration measurement

The nanosatellites were digested in aqua regia solution (Hydrochloric acid and Nitric acid 3:1) overnight. The digested nanosatellites were diluted in Milli Q water. The gold and iron concentrations were measured by using Inductively Coupled Plasma–Optical Emission Spectroscopy (ICP-OES) (Perkin-Elmer Optima 2000 DV). Standard gold and iron elements were used to generate calibration curves.

Nanosatellite vaccine synthesis (E7, r9f and E6 peptide, and cGAMP adjuvant stepwise conjugations with NS) for in vitro experiment

Modified E7, r9f, peptide (0.5mM, 1ml) was incubated with Acetylthio-PEG5k-Maleimide (0.2mM, 1ml) for 2 hours in endotoxin-free water. A drop of 3% HCl solution was added into the solution to activate the thiol functional group. The active solution (200μl) was homogeneously mixed with the NS (Fe 0.05 mg/ml) and incubated at room temperature for 2 hours. The modified E7 peptides conjugated with NS were purified using a magnet separator. The supernatant was taken to quantified the concentration of the peptide by using LavaPep (Gel company, USA). The modified E6 peptide (0.5mM, 1ml) was reacted with Acetylthio-PEG5k-Maleimide (0.2mM, 1ml) for 2 hours and subsequently deprotected the thiol functional group. The E7-NS were further conjugated with

deprotected E6 peptide (10μl) using the same procedure with the modified E7 peptide. The final product was purified overnight using a magnet separator (Nanosep). The unbound E6 in the supernatant was quantified by using LavaPep.

2'3' cGAMP was added into the peptides-conjugated NS at different concentrations.

Nanosatellite vaccine synthesis (E7, q19d and E6 peptide, and cGAMP adjuvant stepwise conjugations with NS) for in vivo experiment

Modified E7, q19d, peptide (0.36 μmol) was incubated with Acetylthio-PEG5k-Maleimide (0.2μmol) for 2 hours in PBS. 2 μl HCL (1.2 mM) was added into the solution to activate the thiol functional group. The active solution was homogeneously mixed with the NS (Fe 0.28 mg/ml) and incubated at room temperature for 2 hours. The modified E7 peptides conjugated with NS were purified using a magnet separator overnight. The supernatant solution was taken to quantify the concentration of the peptide by using LavaPep (Gel company, USA). The modified E6 peptide (0.4μmol) was reacted with Acetylthio-PEG5k-Maleimide (0.2μmol) for 2 hours and subsequently deprotected the thiol functional group. The E7-NS were further conjugated with deprotected E6 peptide (10μl) using the same procedure with the modified E7 peptide. The final product was purified overnight using a magnet separator (Nanosep). The unbound E6 in the supernatant was quantified by using LavaPep. 2'3' cGAMP (0.7μmol in PBS) was added into the peptides-conjugated NS. The final E7 and E6 peptide concentration were

18 nmol and 0.5 nmol respectively. The final product was used without further purification.

Nanoparticle characterizations

Nanoparticles were characterized by TEM. TEM imaging were prepared by the solvent evaporation method. Briefly, the solution (5 μL) of each sample were dropped onto carbon-coated copper TEM grids and allowed to dry overnight. TEM images were acquired on a transmission electron microscope (TEM, Jeol 1400 plus, 80 kV). Hydrodynamic diameters and zeta potential of nanoparticles were measured by Zeta Sizer (Malvern).

ISRE experiments

THP1- blue cells were purchased from Invivogen (USA), and were cultured in RPMI media supplemented with 10% FBS, 1% penicillin and streptomycin antibiotics, Normocin and Zeocin according to the company protocol. The $0.1x10^6$ cells were seeded into each 96 well-plate with the 180μl of the completed media and 20μl of media control, cGAMP (1μg/ml or 10μg/ml final concentration), nanosatellites particles, or the vaccine were added. The cGAMP in the vaccine had the same final concentration with the cGAMP control groups. The cells were incubated with the treatment for 16 hours. The supernatants were taken out and incubated with Quanti-Blue according to the company protocol and measured the absorption at 655nm.

Quantitative Real-time PCR

THP1-blue cells were seeded at one million cells/well in a 6-well plate. The cells were treated 16 hours with media alone, nanosatellites alone, cGAMP (1μg/ml or 10μg/ml final concentration), or the vaccine with cGAMP (1μg/ml or 10μg/ml final concentration). The RNA were isolated and purified using the Qiashredder kit and RNEasy Plus kit (Qiagen). The concentrations of RNA were quantified by NanoDrop. cDNA were generated by High Capacity RNA-to-cDNA kit (Applied Biosystems). RT-PCR were subsequently performed.

Ifnβ1 Elisa assay of bone marrow-derived macrophages

Bone marrow-derived macrophages (BMM) were obtained from C57BL/6 mice at the age of 8 week old. BMM were incubated at 37 °C and 5% CO_2 incubator in RPMI media supplemented with 30% L929 media, 20% heat-inactivated FBS, and 1% penstrep. The new media were added on day 3. 0.5 x 10^6 cells were seeded into 12 well-plate overnight before being incubated with PBS, cGAMP alone (10ug/ml), nanosatellites alone, and the vaccine. Lipopolysaccharide (LPS) was used as a positive control. The cell supernatant was collected at 24 hours after incubation for IFN-β quantification assay (Biolegend) according to the company protocol.

Dendritic cell maturation assay

Bone marrow-derived dendritic cells (BMDC) were obtained from C57BL/6 mice of 8 week old. The cells were cultured in RPMI media supplemented with 10% heat-inactivated FBS, 1% penstrep, glutamine, non-essential amino acid, sodium pyruvate, 2-mercaptoethanol, and 10 ng/ml GM-CSF (Peprotech,USA). The new completed

media supplemented with 20 ng/ml GM-CSF were added on day 3. 0.5 x 10^6 cells were seeded into 12 well-plate on day 6 and incubated overnight. The cells were then treated with PBS, cGAMP alone (10ug/ml), the peptides, vaccine (cGAMP 10ug/ml) or Lipopolysaccharide (200 ng/ml) (eBiosciences). 48 hours after incubation, the cells were washed 3 times with PBS before harvest. The Fc blocker CD16/32 (clone 93, eBiosciences) was used to block non-specific binding before staining with the surface marker antibodies. The cells were then staining with MHC-II-FITC (clone M5/114.15.2, eBiosciences) and CD86 PE (clone GL1, eBiosciences) for maturation markers, and DAPI for viability. The data were analyzed using Flow Jo software.

Nanosatellite vaccine uptake study in BMM

E7 peptide labeled with 6-FAM was conjugated with nanosatellites for cell uptake study compared with free E7-FAM peptide. Bone marrow derived macrophages isolated from C57BL/6 mice' femurs and tibias and were cultured for 6 days in 10 mm non-tissue culture dishes supplemented with conditioned RPMI media with 30% L929 media, 20% FBS, 1% penicillin and streptomycin. On day 6, 4 x 10^4 cells were seeded in to a black 96-well plate overnight to let the cells attach to the plate and supplemented with the conditioned RPMI media without L929. Next day, the media was removed and replaced with phenol red-free and FBS free RPMI media. Nanosatellite vaccine and other controls were incubated with the cells for 2 and 6 hours and then the cells were washed 3 time with PBS. The fluorescent signal was read at the excitation 490 nm and emission 520 nm.

Magnetic resonance imaging (MRI) of lymph nodes in mice

The MRI were preformed using Agilent 7 tesla at TE= 30ms and TR= 4,000ms

NS conjugated with the modified E7 peptides were administered to C57BL/6 mice via subcutaneous injection at tail-base at the iron concentration 50μg/mouse. The mice were on isoflurane vaporizer to maintain anesthetic condition. The mice were imaged before the NS injection to serve as self-control, at 4 hours, and 24 hours post-injection.

In vivo immunization and cancer treatment studies.

The animal studies were followed a protocol approved by Institutional Animal Care & Use Committee (IACUC) at University of Michigan. C57BL/6 mice of age 6-8 weeks (Jackson Laboratory) were subcutaneously implanted with 0.4x 10^6 MOC2 cells at the neck area on day zero. The mice (5/group) were immunized with PBS, 2'3' cGAMP (50 μg/100 μl), peptides (18.5 nmol/100 μl), nanosatellite vaccine (2'3' cGAMP 50ug and peptide 18.5 nmol conjugated with the NS/100 μl), anti PD-L1 antibody (100μg/100μl) (BioXcell, USA). 100 μl of anti PD-L1 antibody was administered to the mice by intraperitoneal injection twice a week. The other formulations (100 μl) were administered by subcutaneous injection at the tail base once a week for 3 weeks. The tumors were monitored and the volume of the tumors were calculated by 0.52 x length x $width^2$.

Flow cytometric characterization of tumor-infiltrating lymphocytes.

Excised tumors were mechanically dissociated and subjected to Ficoll-Paque density gradient centrifugation. Separated TILs were washed twice in RPMI and counted. The

following antibodies were used for flow cytometry: anti-CD3 (BD Biosciences, clone 17A2), anti-CD4 (Biolegend, clone RM4-5), anti-CD8 (Biolegend, clone 53-6.7), anti-CD279 (Biolegend, clone 29F.1A12), and a tetramer recognizing H-2Db-restricted HPV16 E7 epitope RAHYNIVTF (NIH tetramer core). Cell viability was assessed using a fixable viability dye eFluor 780 (Thermo Fisher Scientific). All staining was done in FACS buffer (2% FBS in PBS). Acquisition and compensation was performed on Beckman Coulter CyAn ADP. FlowJo V10 software was used to analyze the data.

Primers for quantitative real-time PCR assays

Gene Name	**Forward (5'->3')**	**Reverse (5'->3')**	**Species**
cxcl10	5’-AATGAGGGCCATAGGGAAGC	5’-AGCCATCCACTGGGTAAAGG	Mm
cxcl9	5’-GAGCAGTGTGGAGTTCGAGG	5’-TCCGGATCTAGGCAGGTTTG	Mm
Ifnb1	5’-CCAGCTCCAAGAAAGGACGA	5’-CGCCCTGTAGGTGAGGTTGAT	Mm
gapdh	5′-TGCACCACCAACTGCTTAG	5′-GGATGCAGGGATGATGTTC	Mm
pan-Ifna	5’-CCTGAGAGAGAAGAAACACAGCC	5’-TCTGCTCTGACCACYTCCCAG	Mm
hprt1	5’-GATTAGCGATGATGAACCAGGTT	5’-CCTCCCATCTCCTTCATCACA	Mm
IFNB1	5'-CATTACCTGAAGGCCAAGGA	5′-CAATTGTCCAGTCCCAGAGG	Hs
IFNA4	5'-CCTAGAGGCCGAAGTTCAAG	5'-TTGTGCCAGGAGTATCAAGG	Hs
CXCL10	5'- CTCCAGTCTCAGCACCATGA	5'- GCTCCCCTCTGGTTTTAAGG	Hs
CXCL9	5'-GTGGTGTTCTTTTCCTCTTGGG	5'-ACAGCGACCCTTTCTCACTAC	Hs
ISG54	5′-ACGGTATGCTTGGAACGATTG-3′	5′-AACCCAGAGTGTGGCTGATG	Hs
GAPDH	5′-TTCGACAGTCAGCCGCATCTTCTT-3′	5′-CAGGCGCCCAATACGACCAAATC	Hs
HPRT1	5'- ATGCTGAGGATTTGGAAAGG	5'- CAGAGGGCTACAATGTGATGG	Hs
ISG15	5’-CTGAGAGGCAGCGAACTCAT-3’	5’-AGCATCTTCACCGTCAGGTC-3’	Hs

4.6 Acknowledgements

This work has been done in collaboration with Yee Sun Tan, Xiaobo Luo, Xinyi Zhao, Blake Heath, Toktam Moghbeli, Yu Lei, Hongwei Chen, and Duxin Sun. We thank Dr. David Mooney for providing the MOC2-E6/E7 cell line.

This work is part of the manuscript conducted by Tan Y.S**., Sansanaphongpricha S**., Xie Y., Donnelly C, Luo X., Zhao X., Bellile E., Heath B.R., Chen Q., Polverini P.J., Carey T.E., Nor J., Young S.W.M., Ferris R., Wolf G.T., Sun D.*, Lei Y.* A Type I Interferon-inducing Nanosatellite Vaccine Mitigates Immune Suppression in Head and Neck Squamous Cell Carcinoma, in submission.

4.7 References:

1. Ferlay, J. *et al.* Cancer incidence and mortality worldwide: Sources, methods and major patterns in GLOBOCAN 2012. *Int. J. Cancer* **136,** E359–E386 (2015).
2. Sanderson, R. J. & Ironside, J. A. D. Squamous cell carcinomas of the head and neck. *BMJ* **325,** 822–7 (2002).
3. Siegel, R., Miller, K. & Jemal, A. Cancer statistics , 2015 . *CA Cancer J Clin* **65,** 29 (2015).
4. Zhao, Y. *et al.* Targeted nanoparticle for head and neck cancers: overview and perspectives. *Wiley Interdiscip. Rev. Nanomedicine Nanobiotechnology* e1469 (2017). doi:10.1002/wnan.1469
5. Rothenberg, S. M. & Ellisen, L. W. The molecular pathogenesis of head and neck squamous cell carcinoma. *J. Clin. Invest.* **122,** 1951–7 (2012).
6. Weber, R. *et al.* Human papillomavirus and survival of patients with oropharyngeal cancer. *N. Engl. J. Med.* **363,** 24–35 (2010).
7. Chaturvedi, A. K. *et al.* Human papillomavirus and rising oropharyngeal cancer incidence in the United States. *J. Clin. Oncol.* **29,** 4294–4301 (2011).
8. Seiwert, T. Y., Salama, J. K. & Vokes, E. E. The chemoradiation paradigm in head and neck cancer. *Nat. Clin. Pract. Oncol.* **4,** 156–171 (2007).
9. Ferris, R. L. *et al.* Nivolumab for Recurrent Squamous-Cell Carcinoma of the Head and Neck. *N. Engl. J. Med.* **375,** 1856–1867 (2016).
10. Seiwert, T. Y. *et al.* Safety and clinical activity of pembrolizumab for treatment of recurrent or metastatic squamous cell carcinoma of the head and neck (KEYNOTE-012): an open-label, multicentre, phase 1b trial. *Lancet Oncol.* **17,** 956–965 (2016).
11. Starr, P. Encouraging Results for Pembrolizumab in Head and Neck Cancer. *Am. Heal. drug benefits* **8,** 16 (2015).
12. Ferris, R. L. Immunology and immunotherapy of head and neck cancer. *J. Clin. Oncol.* **33,** 3293–3304 (2015).
13. Zitvogel, L., Galluzzi, L., Kepp, O., Smyth, M. J. & Kroemer, G. Type I interferons in anticancer immunity. *Nat Rev Immunol* **15,** 405–414 (2015).
14. Dubensky, T. W., Kanne, D. B. & Leong, M. L. Rationale, progress and development of vaccines utilizing STING-activating cyclic dinucleotide adjuvants. *Ther. Adv. Vaccines* **1,** 131–43 (2013).
15. Woo, S. R., Corrales, L. & Gajewski, T. F. The STING pathway and the T cell-inflamed tumor microenvironment. *Trends Immunol.* **36,** 250–256 (2015).
16. Barber, G. N. STING: infection, inflammation and cancer. *Nat. Rev. Immunol.* **15,** 760–770 (2015).
17. Corrales, L. *et al.* Direct Activation of STING in the Tumor Microenvironment Leads to Potent and Systemic Tumor Regression and Immunity. *Cell Rep.* **11,** 1018–1030 (2015).
18. Leoncini, E. *et al.* Induction of tumor regression by intratumoral STING agonists combined with anti-programmed death-L1 blocking antibody in a preclinical squamous cell carcinoma model. *Head Neck* **36,** 1391 (2017).
19. Marur, S., D'Souza, G., Westra, W. H. & Forastiere, A. A. HPV-associated head and neck cancer: A virus-related cancer epidemic. *Lancet Oncol.* **11,** 781–789 (2010).
20. Schoenfeld, J. D. Immunity in head and neck cancer. *Cancer Immunol. Res.* **3,** 12–7 (2015).
21. Bachmann, M. F. & Jennings, G. T. Vaccine delivery: a matter of size, geometry, kinetics and

molecular patterns. *Nat. Rev. Immunol.* **10,** 787–96 (2010).
22. Liu, H. & Irvine, D. J. Guiding principles in the design of molecular bioconjugates for vaccine applications. *Bioconjug. Chem.* **26,** 791–801 (2015).
23. Moon, J. J., Huang, B. & Irvine, D. J. Engineering nano- and microparticles to tune immunity. *Adv. Mater.* **24,** 3724–46 (2012).
24. Hamdy, S., Haddadi, A., Hung, R. W. & Lavasanifar, A. Targeting dendritic cells with nano-particulate PLGA cancer vaccine formulations. *Adv. Drug Deliv. Rev.* **63,** 943–955 (2011).
25. Gamvrellis, A. *et al.* Vaccines that facilitate antigen entry into dendritic cells. *Immunol. Cell Biol.* **82,** 506–516 (2004).
26. Irvine, D. J., Hanson, M. C., Rakhra, K. & Tokatlian, T. Synthetic Nanoparticles for Vaccines and Immunotherapy. *Chem. Rev.* **115,** 11109–11146 (2015).
27. Chithrani, B. D., Ghazani, A. a & Chan, W. C. W. Determining the size and shape dependence of gold nanoparticle uptake into mammalian cells. *Nano Lett.* **6,** 662–8 (2006).
28. Smith, D. M., Simon, J. K. & Baker, J. R. Applications of nanotechnology for immunology. *Nat. Rev. Immunol.* **13,** 592–605 (2013).
29. Gravitz, L. A fight for life that united a field. *Nature* **478,** 163–164 (2011).
30. Caudle, A. S., Yang, W. T., Mittendorf, E. A. & Kuerer, H. M. The impact of nanoparticle ligand density on dendritic-cell targeted vaccines. *Biomaterials* **32,** 3094–3105 (2011).
31. Chang, T. Z., Stadmiller, S. S., Staskevicius, E. & Champion, J. A. Effects of ovalbumin protein nanoparticle vaccine size and coating on dendritic cell processing. *Biomater. Sci.* **5,** 223–233 (2017).
32. Chen, H. *et al.* Facile Fabrication of Near-Infrared-Resonant and Magnetic Resonance Imaging-Capable Nanomediators for Photothermal Therapy. *ACS Appl. Mater. Interfaces* **7,** 12814–12823 (2015).
33. Volatron, J. *et al.* Ferritin Protein Regulates the Degradation of Iron Oxide Nanoparticles. *Small* 1–13 (2016). doi:10.1002/smll.201602030
34. Mazuel, F. *et al.* Massive Intracellular Biodegradation of Iron Oxide Nanoparticles Evidenced Magnetically at Single-Endosome and Tissue Levels. *ACS Nano* **10,** 7627–7638 (2016).
35. Alric, C. *et al.* The biodistribution of gold nanoparticles designed for renal clearance. *Nanoscale* **5,** 5930–9 (2013).
36. Longmire, M., Choyke, P. L. & Kobayashi, H. Clearance properties of nano-sized particles and molecules as imaging agents: considerations and caveats. *Nanomedicine (Lond).* **3,** 703–717 (2008).
37. Chou, L. Y. T., Ming, K. & Chan, W. C. W. Strategies for the intracellular delivery of nanoparticles. *Chem. Soc. Rev.* **40,** 233–245 (2011).
38. Shi, J., Kantoff, P. W., Wooster, R. & Farokhzad, O. C. Cancer nanomedicine: progress, challenges and opportunities. *Nat. Rev. Cancer* **17,** 20–37 (2016).
39. Takai, Y., Nishiyama, K., Yamamura, H. & Nishizuka, Y. Guanosine 3'5'-Monophosphate-dependent Protein Kinase from Bovine Cerebellum. *J. Biol. Chem.* **250,** 4690–4695 (1975).
40. Fan, Y. & Moon, J. J. Nanoparticle Drug Delivery Systems Designed to Improve Cancer Vaccines and Immunotherapy. *Vaccines* **3,** 662–85 (2015).
41. Laurent, S. *et al.* Magnetic iron oxide nanoparticles: synthesis, stabilization, vectorization, physicochemical characterizations, and biological applications. *Chem. Rev.* **108,** 2064–110 (2008).
42. Mornet, S. *et al.* Magnetic nanoparticle design for medical applications. *Prog. Solid State Chem.* **34,** 237–247 (2006).
43. Manolova, V. *et al.* Nanoparticles target distinct dendritic cell populations according to their size.

Eur. J. Immunol. **38,** 1404–1413 (2008).
44. Bousso, P. T-cell activation by dendritic cells in the lymph node: lessons from the movies. *Nat. Rev. Immunol.* **8,** 675–84 (2008).
45. English, D. & Andersen, B. R. Single-step separation of red blood cells, granulocytes and mononuclear leukocytes on discontinuous density gradients of Ficoll-Hypaque. *J. Immunol. Methods* **5,** 249–252 (1974).
46. Hong, R. *et al.* Glutathione-mediated delivery and release using monolayer protected nanoparticle carriers. *J. Am. Chem. Soc.* **128,** 1078–1079 (2006).
47. Chiu, Y. H., MacMillan, J. B. & Chen, Z. J. RNA Polymerase III Detects Cytosolic DNA and Induces Type I Interferons through the RIG-I Pathway. *Cell* **138,** 576–591 (2009).
48. Zhang, X. *et al.* Cyclic GMP-AMP containing mixed Phosphodiester linkages is an endogenous high-affinity ligand for STING. *Mol. Cell* **51,** 226–235 (2013).
49. Chen, H. *et al.* Highly crystallized iron oxide nanoparticles as effective and biodegradable mediators for photothermal cancer therapy. *J. Mater. Chem. B* **2,** 757 (2014).
50. Chen, H. *et al.* Biocompatible polysiloxane-containing diblock copolymer PEO-b-PγMPS for coating magnetic nanoparticles. *ACS Appl. Mater. Interfaces* **1,** 2134–2140 (2009).

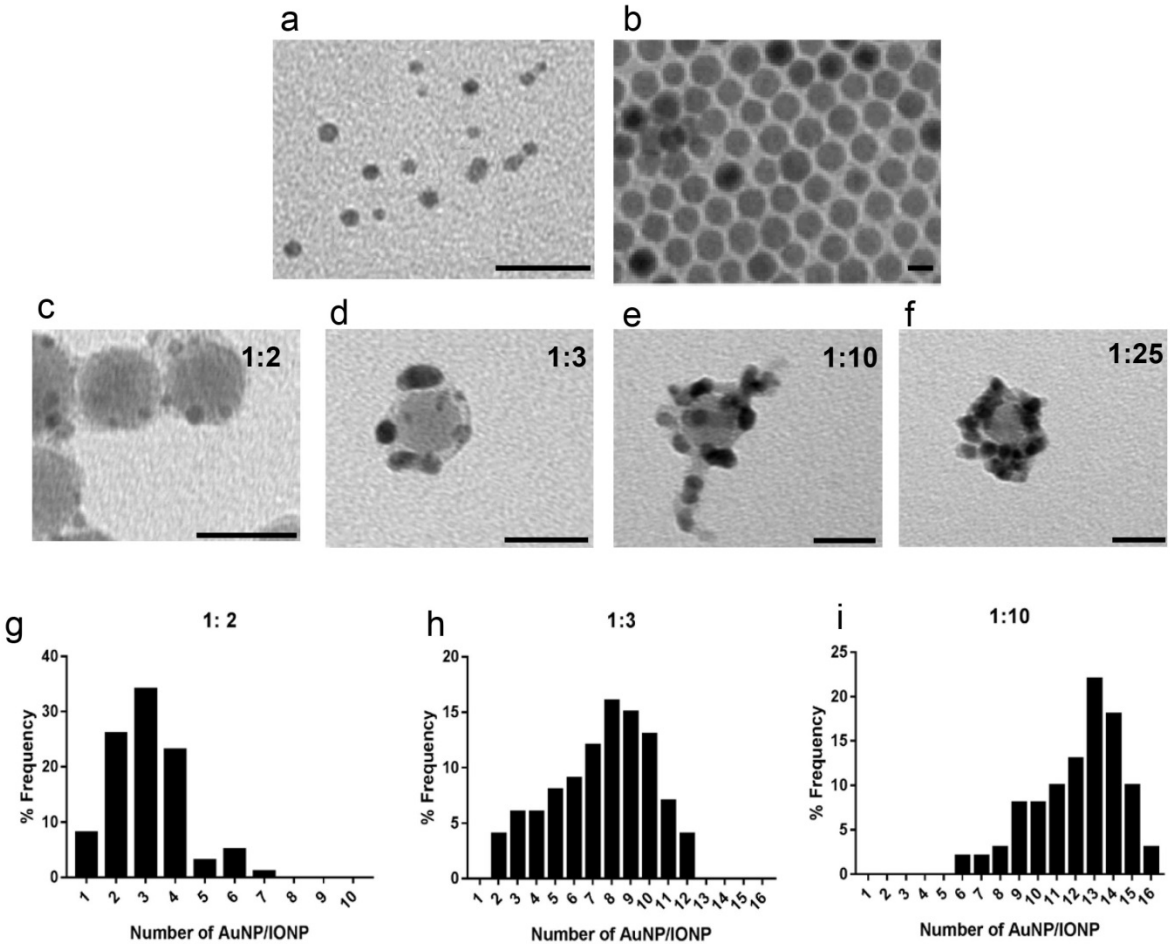

Figure 4.1. Nanosatellite particles compositions. a) and b) are TEM images of gold sulfide and iron oxide nanoparticles respectively. c-f) represent the TEM images of the nanosatellites with different molar ratios of gold sulfide and iron oxide nanoparticles. g- i) the bar graphs show the number of gold nanoparticles/iron oxide core when the different molar ratios were used to make the nanosatellites. The most stable nanosatellite system with the decent number of the gold sulfide nanoparticles is 1:3 molar ratio, which was used for the further conjugation with peptides. Scale bars represent 20 nm.

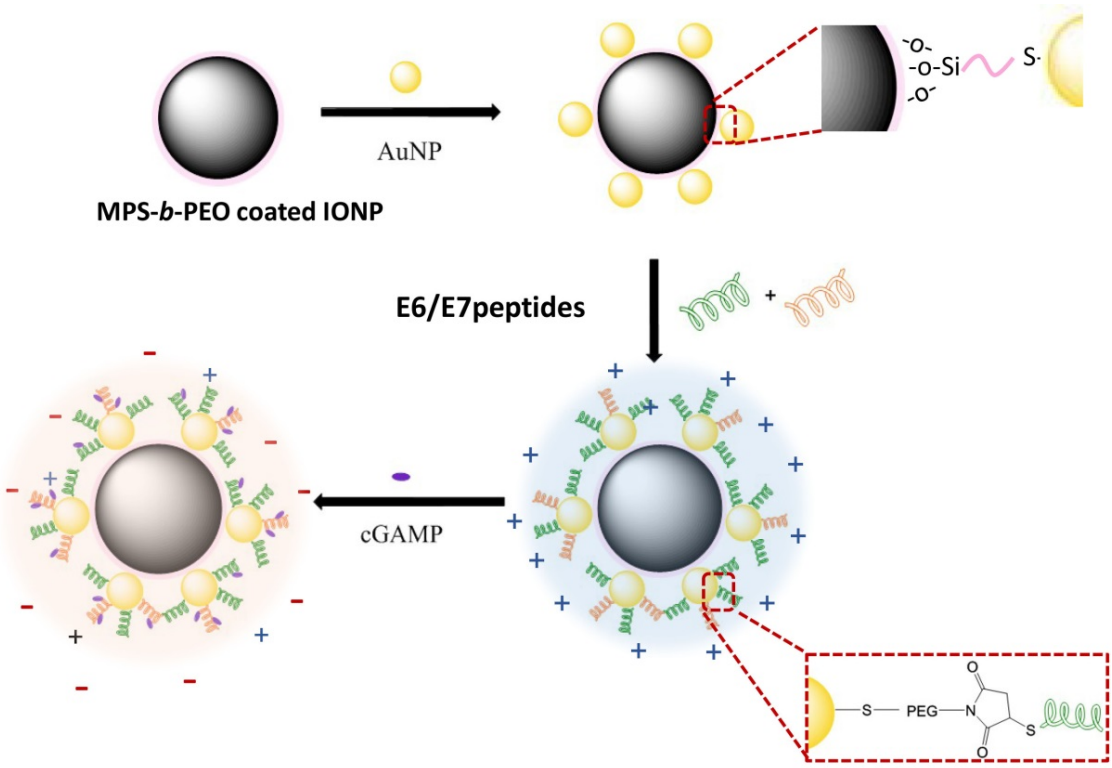

Scheme 4.1. a cartoon picture describes the process of the E7/E6 antigenic peptides and cGAMP adjuvant conjugation. The gold sulfide nanoparticles were attached to the iron oxide core by a unique polymer MPS-*b*-PEO. Modified E7/E6 peptides were covalently conjugated with the gold satellites via maleimide-thiol functional PEG linkers. The cGAMP adjuvant was electrostatically bound to the E7/E6 peptide in the last step.

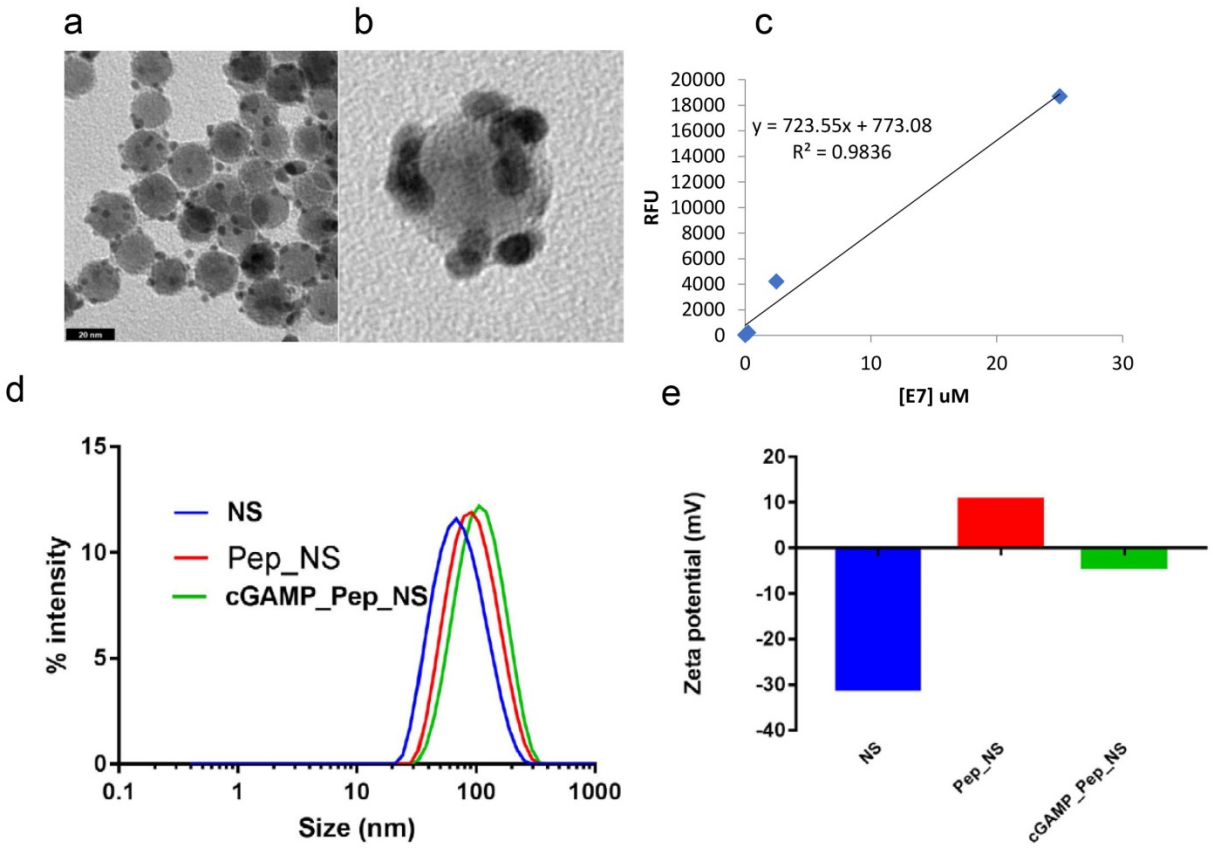

Figure 4.2. Nanoparticle characterizations. a) and b) show the TEM images of the nanosatellites with a diameter *ca*. 25 nm. c) a calibration curve of the peptide conjugation for determining the conjugation efficiency. The conjugation efficiency is 91%. d) Hydrodynamic diameter measured by a dynamic light scattering method. The D_h slightly increase after peptide and cGAMP conjugation. e) the chart demonstrates the surface charges of the naked nanosatellites (blue), peptide conjugated NS (red), and cGAMP conjugated NS (green). The surface charges dramatically changed in each step indicating the successful conjugation.

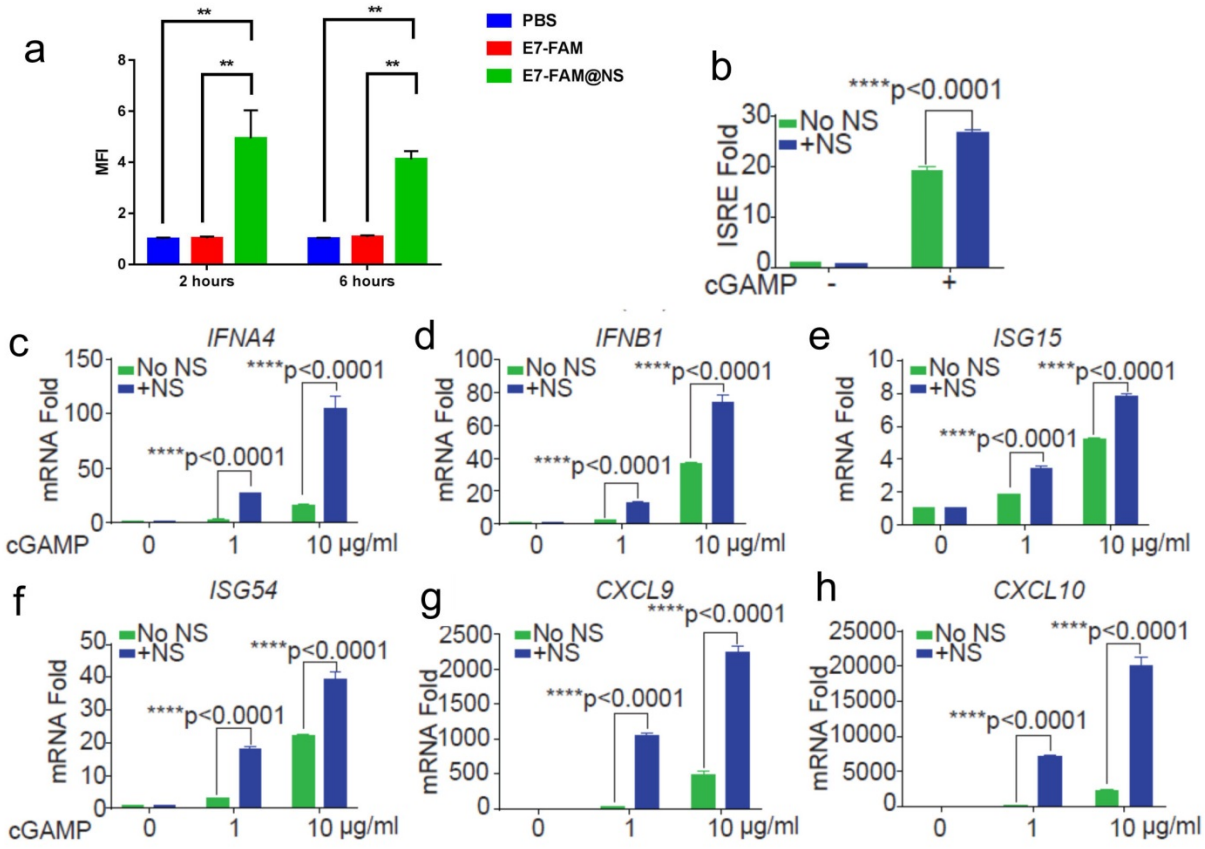

Figure 4.3. *In vitro* assays show nanosatellites enhance peptide uptake, promote ISRE activity and upregulate IFN-I related genes. a) Nanosatellites enhance the antigenic fluorescent labelling peptide E7-FAM uptake in BMM after 2 and 6 hours of incubations. b) ISRE promoter activity in THP1- blue reporter cells were effectively induced by the nanosatellite vaccine after the cells were incubated with the nanosatellite vaccine compared to cGAMP alone, nanosatellite alone or PBS. c-h) THP1 cells were treated with different doses of cGAMP with or without the nanosatellites delivery vehicle. The mRNA abundance of the indicated IFN-I signaling genes were quantitated by real time PCR. Nanosatellite vaccine strongly induces the type I FN related genes upregulation in a dose-dependence of cGAMP.

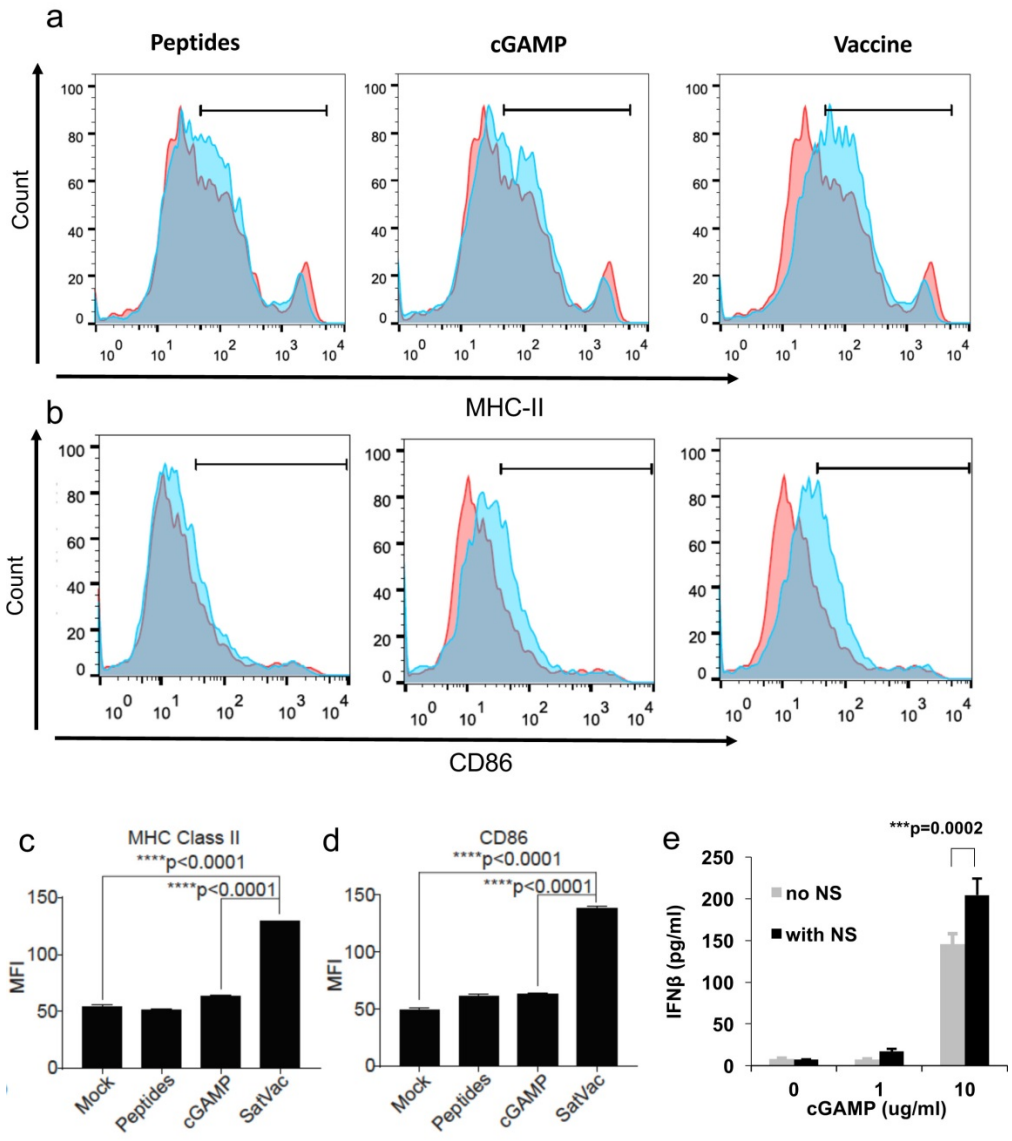

Figure 4.4. DC maturation assays. a-b) demonstrate that the nanosatellite vaccine induces the expression of the maturation markers of DC such as MHC-II and CD86. The red color represents PBS control and the blue color indicates the different treatments for each group. c-d) represent the mean fluorescence intensity of the flow cytometry analysis of MHC-II and CD86 expression on DC after being incubated with E7/E6 peptides, cGAMP, and the vaccine. The assays were done in triplicates. e) Nanosatellite vaccine also promotes the secretion of IFNβ in BMDM measured by ELISA

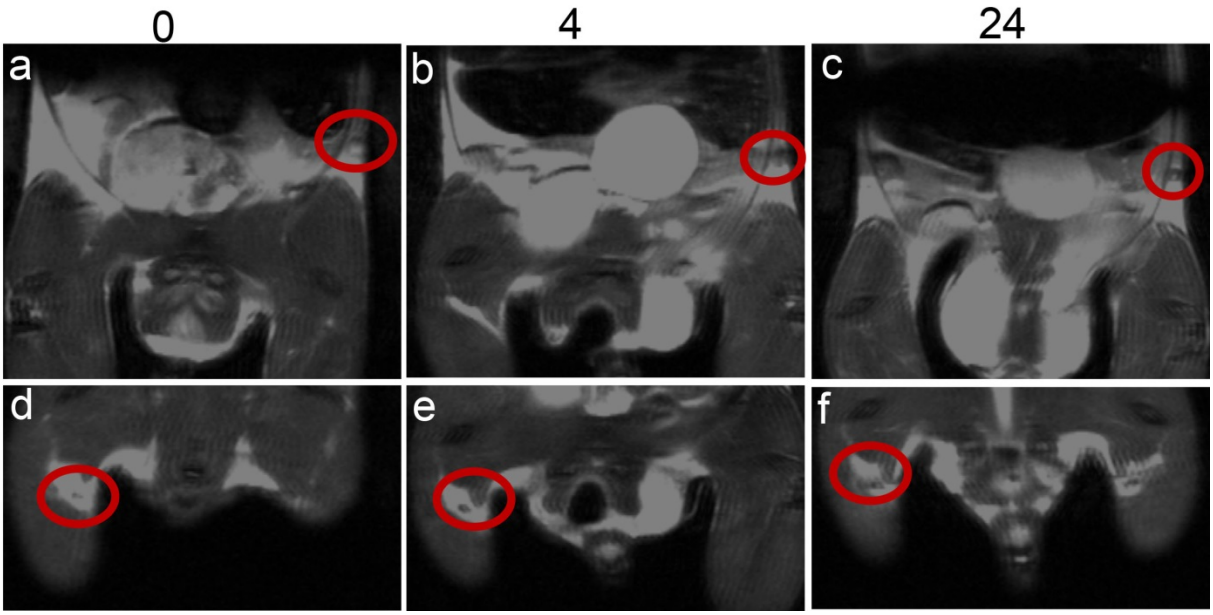

Figure 4.5. *In vivo* magnetic resonance images of the inguinal popliteal lymph nodes at the pre-injection and 4- and 6- hours post subcutaneous injection at the tail base. The images clearly show that the nanosatellite vaccine can travel to the inguinal and popliteal lymph nodes within 4 hours after injection and accumulate there at least 24 hours. In a) to c), the highlighted red circle refers to the inguinal lymph node, while in d) to f), the highlighted region is the popliteal lymph node.

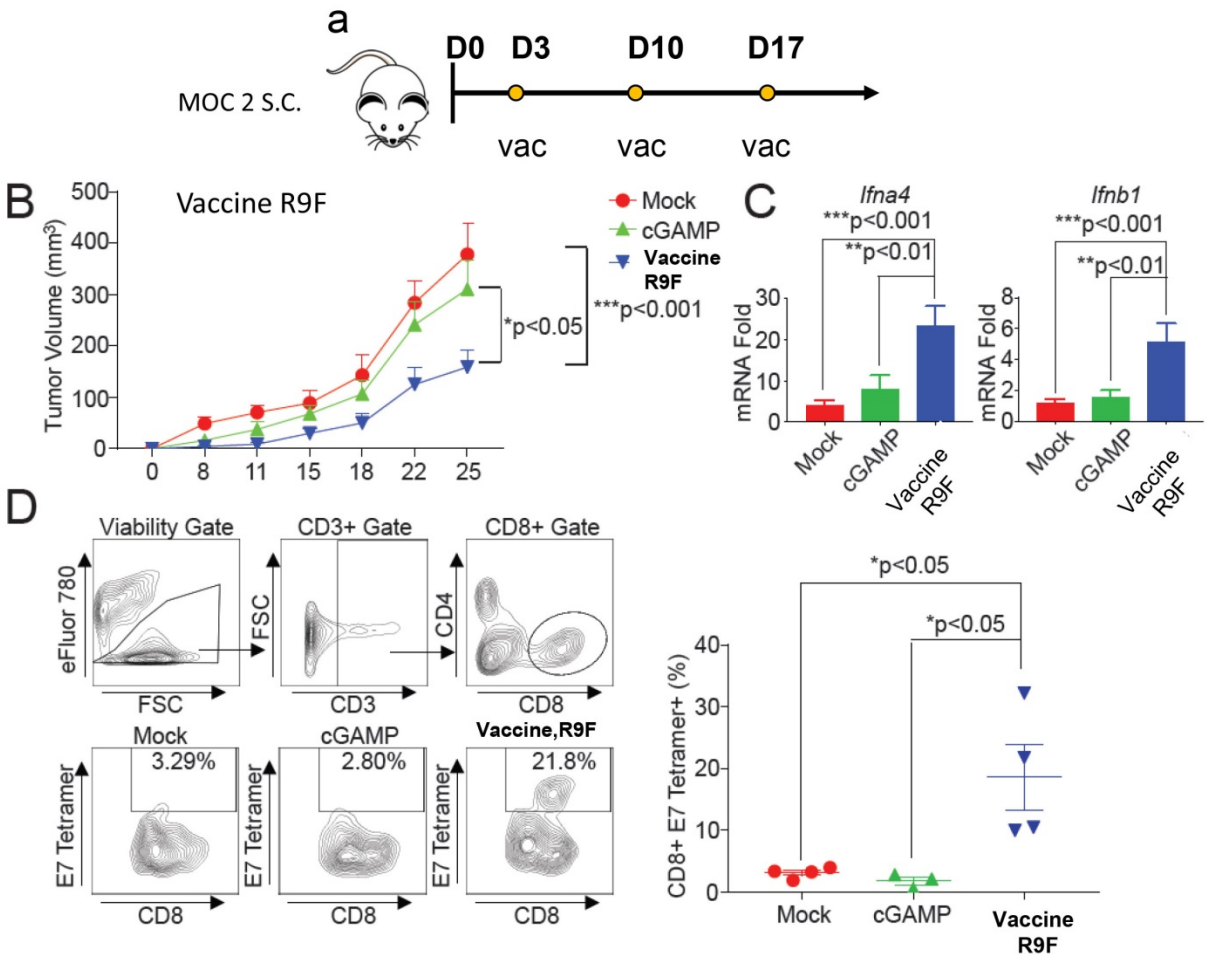

Figure 4.6. *In vivo* vaccination in tumor-bearing mice. a) a schematic picture describes vaccination schedule. The treatments stared 3 days after tumor implantation of MOC2 cells. Other controls were also given at the similar schedule with the vaccine R9F. b) Tumor measurements of mice with indicated treatments.The nanosatellite vaccine R9F significantly suppress the tumor growth in mouse xerograph model. c) The mRNA were isolated from the tumor tissue and quantified by real-time PCR. The vaccine R9F promotes the upregulation of *Ifna4* and *Ifnb1 in vivo* compared to other controls. d) Flow cytometry analysis of E7-specific CTL isolated from tumors. The vaccine R9F proves effective to boost the E7-specific $CD8^+$ T cell immunity.

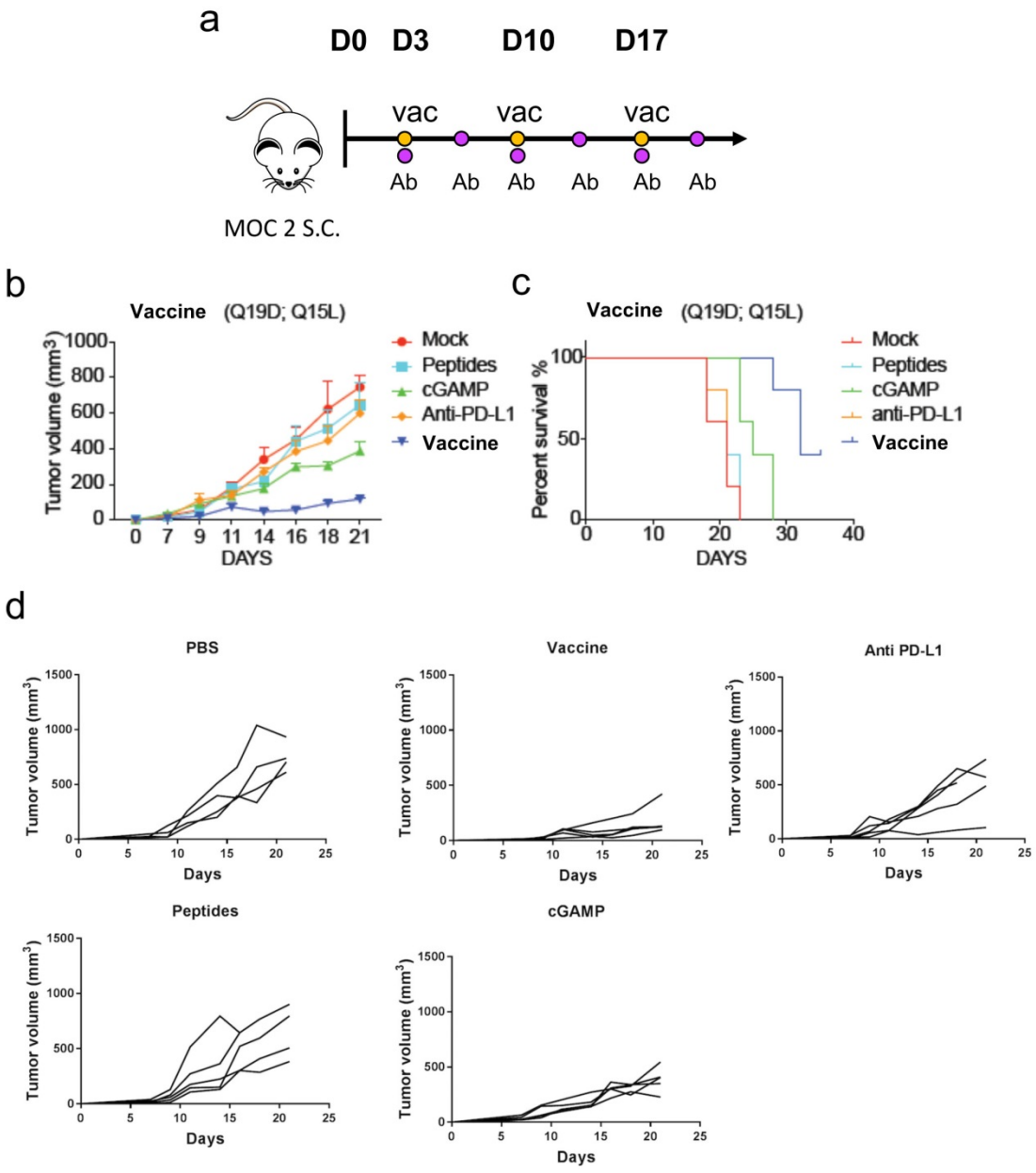

Figure 4.7. *In vivo* study of tumor-bearing mice with vaccine Q19D. a) A schematic picture describes vaccination and anti PD-L1 antibody injection schedule. The treatments started 3 days after subcutaneous tumor implantation. Other controls were also given at the similar schedule with the vaccine Q19D. b) Tumor measurements of mice with the indicated treatment. The nanosatellite vaccine Q19D significantly reduces tumor burden in mouse xerograph model. c) Kaplan-Meier survival curves of the mice described in a) and b). Nanosatellite vaccine Q19D shows longer survival of the tumor-bearing mice compared to other groups of treatments. d) The charts show the individual tumor growth details of each mouse from figure b across 5 groups, PBS control, nanosatellite vaccine (Q19D), peptides, cGAMP, and anti PD-L1 antibody treatments.

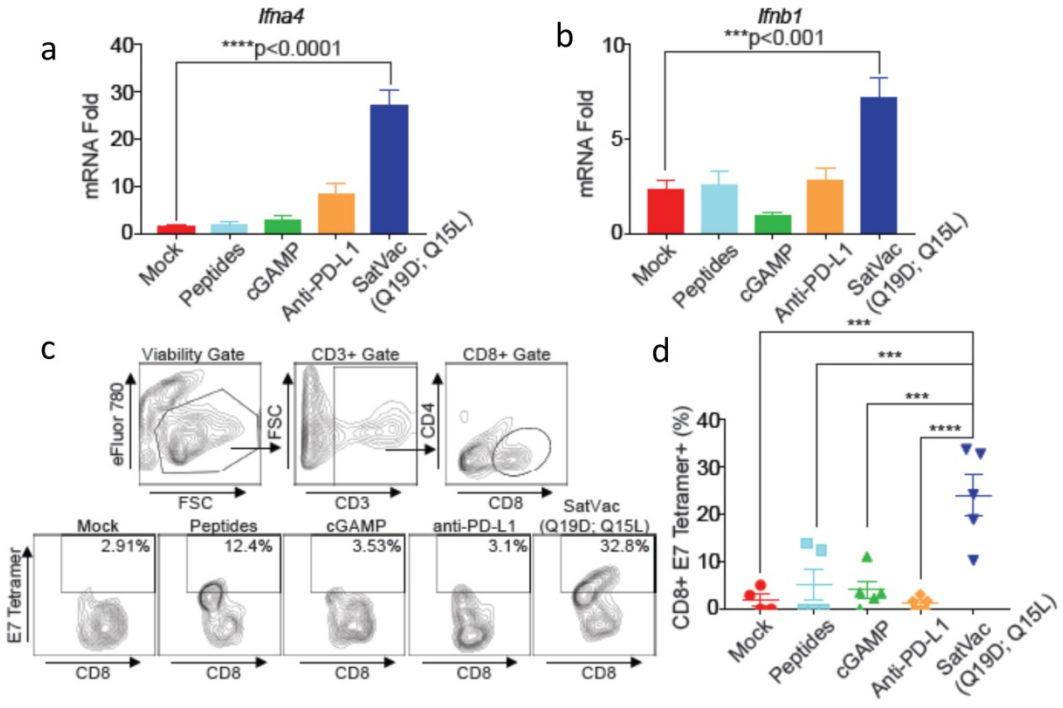

Figure 4.8. a-b) the mRNA levels of pan- ifna4 and ifnb1 significantly increase the mice treated with vaccine Q19D. c-d) Flow cytometry analysis of E7-specific CTL isolated from tumors. The vaccine Q19D effectively promotes the E7-specific $CD8^+$ T cell immunity.

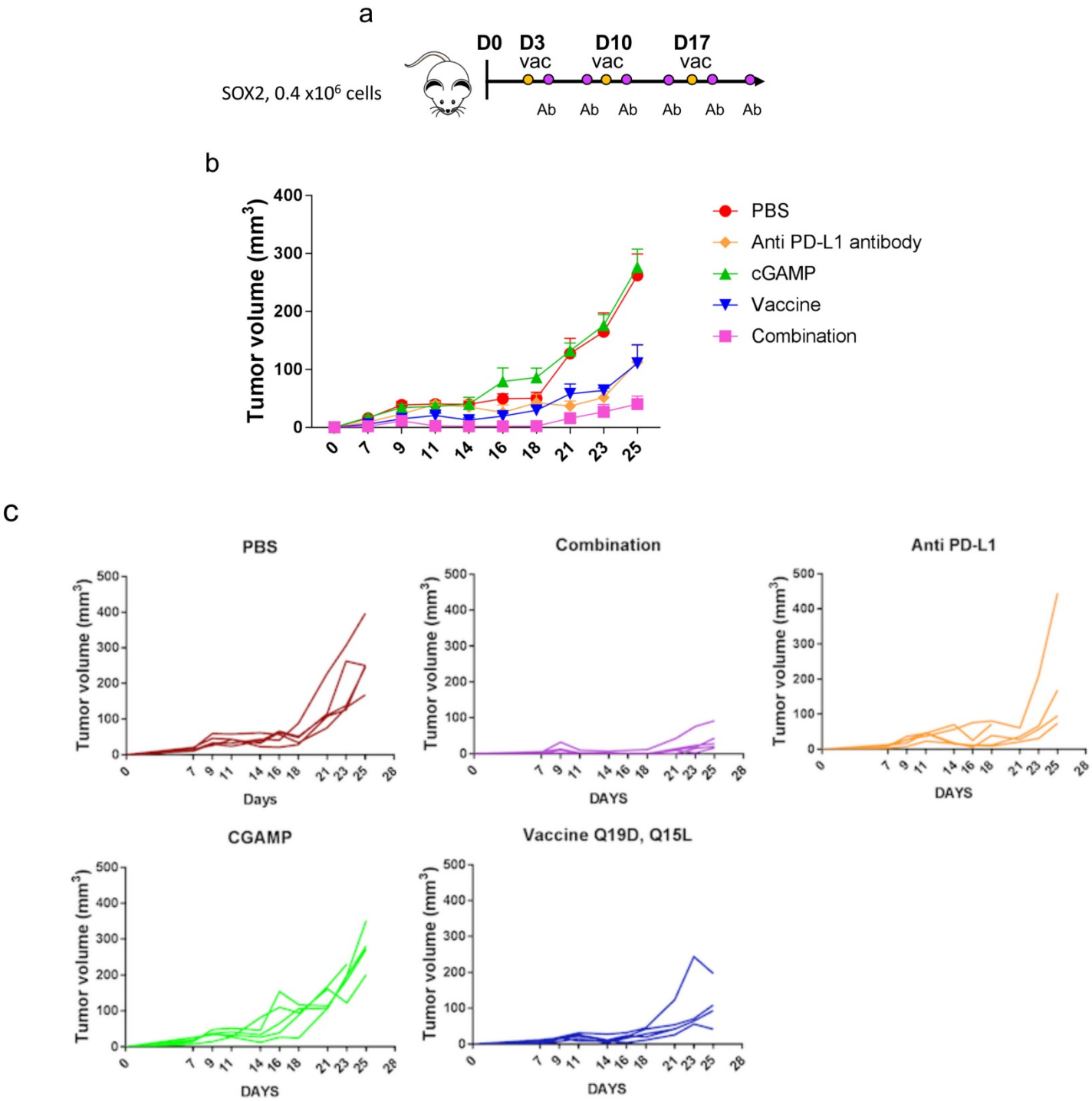

Figure 4.9. *In vivo* study of the SOX 2-positive tumor-bearing mice. The treatment in each group was started at day 3 after the tumor implantation. a) a cartoon picture demonstrates the treatment timeline. All treatments were given once a week for three weeks but anti PD-L1 antibody was given twice a week for three week. b) the combination therapy shows significant tumor suppression compared to other groups at day 25 after tumor implantation. The nanosatellite vaccine (Q19D) and anti PD-L1 antibody also show a certain level of tumor suppression. c) The details of tumor growth curves from figure b were plotted individually.

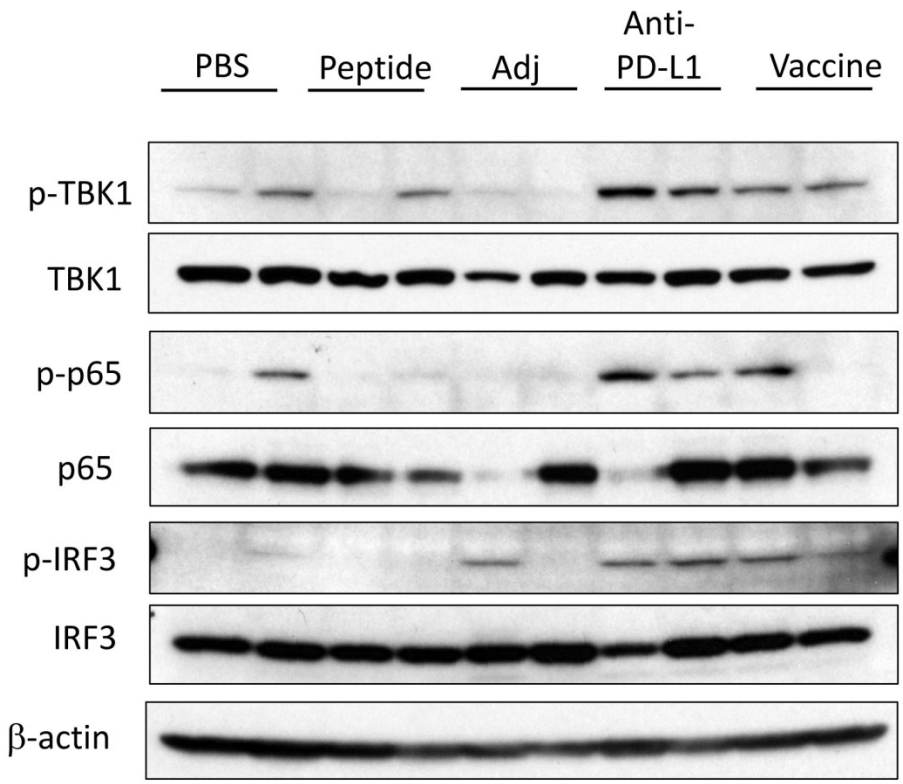

Figure 4.10. The tumor tissues from mice with different treatments were harvested. Tumor tissues from mice were randomly selected from each group of the treatments and the western blotting was performed. Nanosatellite vaccine and anti PD-L1 stimulate STING pathway as shown by the increase in the phosphorylation of TBK1, p65, and IRF3 proteins, which can subsequently promote type-I IFN production.

CHAPTER 5

CONCLUSIONS, SIGNIFICANCES, AND FUTURE PERSPECTIVES

The work presents in this dissertation mainly focuses on the developments and applications of structures made from gold and iron oxide nanoparticles. We investigate the mechanism to control the formation of secondary structures and fabricate two different types of the secondary structures, asymmetrical Janus and symmetrical nanosatellite structures. Additionally, we demonstrate the applications of our secondary nanostructures for enhanced photothermal effect and drug delivery.

We also focus on using two different polymers, thermo-cleavable polymer and poly (γ-MPS-*b*-PEO), for different structure formations. The thermo-cleavable polymer is used to form asymmetrical Janus structure formation in chapter 2. We then further studied the utilization of the thermo-cleavable polymer for controlled drug and nanoparticle release in chapter 3. The poly (γ-MPS-*b*-PEO) is used to form nanosatellite structures in chapter 4.

In chapter 2, we report the multi-building block Janus nanostructure formation by seed-mediated self-assembly method. This method is reported for the first time by our group. This novel thermo-cleavable inducing self-assembly overcomes limitations of

current multi-building block Janus manufacturing. This novel method is both simple and scalable. We use AuNP and IONP as a proof of concept for the multi-building block Janus production; however, this method can potentially be used for other types of inorganic nanoparticles such as quantum dots or silica particles. We then further explored the unique applications of the formed asymmetrical Janus nanostructures (JNS) for enhanced photothermal effect. We hypothesize that the proximity between the nanoparticles synergize the cumulative and Coulomb effects generating electron clouds in JNS. The data indicate strong temperature increase of the JNS over control than other controls after NIR laser light irradiation. The uneven temperature distribution on the surface of JNS is due to different light absorption capacity, making the JNS rotate actively under NIR light as measured by optical tweezers. The exceptionally active Brownian motion of the JNS raise the possibility of a fuel-free Janus motor for cargo delivery. Most previously reported Janus motors required fuel such as hydrogen peroxide or strong acid to react with the particles to generate the gas for propulsion; hence, these fuel-required Janus motors have very limited bio-medical applications. Conversely, our Janus motor's active motion is precisely driven by the NIR laser light, which acts as an on-off switch. However, improved techniques to examine and detect the Janus motor movement are required for future studies, and we acknowledge the lack of sensitivity and accuracy of today's technology for a nanoscale Janus motor motion tracking. In summary, the multi-building block Janus formed by temperature-triggered self-assembly is a good candidate for photothermal therapy, and represents a potential avenue for future fuel-free Janus motors.

In chapter 3, we continued investigating the use of the thermo-cleavable polymer to control drug release system. We found that IONP co-encapsulated with Dox in the thermo-cleavable micelles can be released after NIR laser trigger. This method represents an on-demand drug release. IONP function as a photothermal converter generating heat, which subsequently disrupts the micelles and releases both Dox and IONP at the same time. We expect that the released IONP, which have smaller size than the whole micelles, can penetrate deeper into tumor mass. A second treatment of the photothermia may eradicate the deep tumor mass. This NIR-triggered drug release can be used to treat inoperable metastatic tumors. Although deeper investigations of NIR laser-triggered drug release method in animal models are still required, this controlled drug release system may be a source of hope for inoperable metastatic cancer treatment.

In chapter 4, another secondary structure made from AuNP and IONP is highlighted in addition to the asymmetrical secondary Janus structures reported in chapter 2. We developed and characterized these nanosatellite structures for vaccine delivery. We used HPV^+ head and neck cancer as a model for the treatment because there is a treatment gap for viral-induce cancer and current HPV vaccines since current vaccines have not been approved for the head and neck cancer (HNSCC) treatment. More importantly, the number of HPV^+ HNSCC patients presently exceeds the number of HPV^+ cervical cancer patients. Interestingly, there is no public awareness of this HPV^+ HNSCC and therefore incidence of HPV^+ HNSCC is increasing in the future. This suggests that there is an urgent need to develop an HPV^+ vaccine for HNSCC

treatment. Our animal studies show the promising results and it is possible to warrant a clinical trial. Although the treatments in our experiments started very early when the tumors were comparative smaller than what physicians encounter, this vaccine could be used in a combination with or after ionizing radiation or surgery. Moreover, the nanosatellite vaccine platform does not only limit the use for the HNSCC treatment but also can extend the applications to personalized medicines using a neo antigen specifically to an individual patient for the best result.

Finally, the goals of this thesis are to invent new materials for cancer theranostics by using photothermal effect, active rotational motion, controllable drug delivery, or stimulate host's anti-tumor immunity. This thesis underscores the roles of nanoparticles for advanced medical applications.

APPENDIX A

GOLD/IRON OXIDE NANOCOMPOSITES FOR DUAL CANCER THERAPY AND IMAGINGS

A.1 Abstract

It has been well-known that one of the most common treatments for cancers is ionizing radiation. This method employs gamma rays to generate reactive oxygen species to damage DNA strands resulting in suppression of cell proliferation and causing cell death. However, the current ionizing radiation lacks of specific target causing damage to normal tissues especially repeatedly high dose ionizing radiation treatments. This leads to undesirable adverse effects to patients. Recently, photothermal therapy (PTT) has gained a lot of attention due to the high efficiency and less invasion. In this study, we developed and investigated an ionizing radiation and photothermal effect of the gold and magnetic iron oxide nanocomposite micelles (GMC). GMC demonstrate good photothermal and enhanced ionizing properties in 4T1 breast cancer cells *in vitro*. Moreover, the GMC also used as an MRI and CT contrast agent.

A.2 Introduction

Presently, radiation therapy or ionizing radiation is one of the most commonly used techniques in clinical cancer therapy such as breast cancer[1], head and neck cancer[2], and prostate cancer [3]. The radiotherapy could be used in a combination with chemotherapy or with surgery to increase success rate of treatments[4,5]. The current techniques for ionizing radiation could be divided into two major categories 1) Eternal-beam radiation therapy in which photon beams are delivered from an external source penetrating into the skin and reaching the tumor in the body[6]. 2) Internal radiation therapy or brachytherapy in which the radioactive material is either temporarily or permanently placed inside or on the patient body to deliver the radiation to the proximal area of disease[7]. Unfortunately, the ionizing radiation in either ways is non-specific to the tumors. The radiation doses used to kill the tumor cells are not different from those killed normal cells. Although the proliferating tumor cells have slightly higher mitochondria activity than normal cell, tumor cells develop resistance to the radiation over the period of time. As a consequence, the doses must be increased[8]. Normal tissues exposed to the radiation are unavoidably damaged causing serious side effects to the patients. In a decade, several high atomic number particles including gold nanoparticles have been intensively studied. These particles can generate Auger electrons after being irradiated with photoelectron beams such as gammy or X-rays, which subsequently yields high ionization density locally[8]. These local secondary electrons can generate reactive oxygen species and actively interact with DNA strands

resulting in DNA damage and halting cell proliferation[9]. Hainfeld and coworker (2004) pioneered the use of gold nanoparticle for radiotherapy. The authors proved that 1-year survival rate in tumor-bearing mice treated with 1.9 nm gold nanoparticles and radiotherapy was 4.3 times higher than the mice treated with radiotherapy alone at the same doses of X-rays. Chang M.Y. and coworkers (2007) showed that 13 nm gold nanoparticles induced B16F10 melanoma cell apoptosis *in vitro* after the cells were incubated with the gold nanoparticles and being treated with the radiation[10]. Roa et al (2009) investigated the cell cycles of the radiation-resistant human prostate cancer cells after being treated with glucose-coated gold nanoparticles (Glu-AuNP) and radiation. The Glu-AuNP and radiation combination treatment accelerated G0/G1 phase but arrested G2/M phase resulting in the increase of radio-sensitivity of the cells[11]. Moreover, due to their high atomic number, gold nanoparticles have also been explored as a computed tomography (CT) contrast agent. The CT imaging is one of the most useful techniques used in clinical practice. The CT contrast agent used currently is iodinated compounds, which have very short half-life and iodine itself has lower atomic number than gold. Therefore, it is feasible to use gold nanoparticle to improve the quality of CT imaging in clinic. *In vitro* data revealed that pegylated gold nanoparticles provided attenuation coefficient 5.7 times higher than a commercial iodinated contrast agent[12].

Besides, photothermal therapy (PTT) has been attracting a great deal of attention in a past decade. This technique takes advantages of a photothermal contrast agent to convert photons to phonons resulting in the release of heat energy or high temperature.

Iron oxide nanoparticles (IONP) and gold nanoshells have been known for their photothermal capability. Iron oxide nanoparticles have been reported to generate heat energy under magnetic fields or magnetic hyperthermia and NIR laser irradiation or photothermal effect. The magnetic and conversion abilities depend upon the crystallinity and volume of the particles[13–15]. Crystalized iron oxide nanoparticles absorb the light at near-infrared wavelength, 650-900 nm and emit heat energy[16]. NIR laser irradiation is considered safe for in vivo use under the low laser power because body fluid, such as hemoglobin, has low absorption in this wavelength[17–19]. Similarly, to iron oxide nanoparticles, gold nanoshells can also absorb the near infrared light and emit phonon. Gold nanoshells have gained a lot of attention since last a decade and have been being investigated in a clinical trial for head and neck cancer, and lung cancer treatment. However, there is still a serious concern about their safety and accumulation in the body. The sizes of gold nanoshells generally vary from 10-200 nm with silicon shell, which has very limited clearance[18]. For these reasons, iron oxide nanoparticles may be a better alternative choice for PTT because they are biodegradable to endogenous substance such as ferric and ferrous.

Although small sizes of gold and iron oxide nanoparticles are preferred for both radiotherapy and photothermal therapy, they have very rapid clearance. The high doses of nanoparticles are required. We propose to use gold/iron oxide micelles, which are composed of multiple small gold and iron oxide nanoparticles to prolong the half-life of the nanoparticle without compromising the radiation and photothermal properties of the small nanoparticles as well as imaging capability.

In our study, we explored the dual ability of gold and magnetic iron oxide nanoparticle nanocomposite micelles (GMC) for ionizing radiation and PTT in murine breast cancer cells as well as imaging properties. Oleic acid-coated iron oxide nanoparticles with the size of 15 nm and 2 nm dodecane thiol-coated gold nanoparticles co-encapsulated in DA-*b*-PEO polymeric micelles were synthesized, characterized and investigated for in vitro properties.

A.3 Results and discussion

A.3.1 Nanoparticles synthesis and characterization

Hydrophobic dodecane thiol gold nanoparticles (AuNP) were synthesized by a previously reported method. The synthesized AuNP have the diameter *ca* 2 nm characterized by transmission electron microscope (TEM) (figure A.1a). The AuNP do not have an absorption peak at UV-visible region because the diameter is too small, which correspond to the previous report. The AuNPs are stable for over a month after synthesis. There is no absorption wavelength shift or a sign of aggregation formation (figure A.1b). The DA-*b*-PEO and 15 nm iron oxide nanoparticles (IONP) were synthesized as previously mentioned in Chapter 2. AuNP and IONP were encapsulated together in DA-*b*-PEO polymeric micelles. TEM images suggest that AuNP and IONP formed dense random clusters inside the micelles due to a hydrophobic interaction (figure A.1d and e). Hydrodynamic diameter of the gold and magnetic iron oxide micelles (GMC) is 172.7 nm with polydispersity index 0.106 measured by a dynamic light scattering method (figure A.1f).

A.3.2 Enhanced nanoparticle uptake, Photothermal effect, and ionizing radiation

We investigated the cell uptake of the GMC in a normal incubation condition and acceleration condition under the magnet. 4T1 murine breast cancer cells were incubated with the GMC with or without a magnet under the cell culture plates at different time points. The data suggest that the cell uptake of the gold and iron in 4T1 cells is increasing at 2, 4, and 6 hours after incubation. The concentrations of gold in 4T1 cells increase to 1.4, 6.4, and 3.1 times higher than the concentration of gold in GMC without the magnet acceleration at 2, 4, and 6 hours, which agrees with the concentration of iron in the cells at the same time points. The concentrations of iron increase up to 1.8, 4.2, and 4.4 times higher than those without acceleration by a magnet (figure A.2). This suggest that the concentration AuNP uptaken into the cells could be enhanced by the magnet acceleration because the AuNP were encapsulated together with IONP in micelles. When the magnet induces the cell uptake of IONP, the AuNP are also internalized into the cells simultaneously. The increase of cell uptake of AuNP is important for ionizing radiation and CT scan because the theranostics of AuNP require very high dose of AuNP. *In vivo* intravenous dose of 1.9 nm gold nanoparticles used for ionizing radiation is extremely high (2.7g/kg)[20] and 4g/kg for CT imaging[21]. However, the dose of AuNP used for ionizing radiation and CT imaging can be reduced with the magnet-enhanced cell uptake of GMC.

A.3.3 Photothermal effect of GMC

The photothermal efficacy of GMC was investigated using a NIR laser, 885 nm, 1W/cm^2, with the spot 5x8 mm. 10 minutes after the laser irradiation, the temperature of

the media containing GMC increased 42.9 °C from the initial temperature, while the temperature increase of the water control was only 9.4 °C. The IONP micelles were also used as a positive control to compare whether the insertion of AuNP into the IONP in the GMC disrupts the photothermal efficacy of IONP in the GMC. The IONP micelles raised 51 °C from the initial temperature, which is relatively higher than GMC at the same concentration of Fe (figure A.3a). There are two possibilities of the different temperature increase between the GMC and IONP at the same concentration of Fe. First, the insertion of AuNP between the IONP may disrupt the ability of IONP to convert photons to phonons and the release of phonon to the media. Second, Au interferes absorption wavelength of IONP when the concentration of Fe was measures by colorimetric methods. This can create an error in Fe concentration calculation in GMC, which turn into overestimate the concentration of Fe in the sample. In this case, we used 2 nm AuNP, which cannot contribute to the temperature increase because the size of AuNP are too small and do not have absorption at UV-VIS and NIR regions[22,23] (figure 3b). This agrees with previous reports. However, the data suggest that GMC can generate high temperature after NIR laser irradiation due to IONP and GMC could be used as photothermal contrast agent at NIR wavelength.

A.3.4 Ionizing radiation effect of GMC in breast cancer cells

We performed clonogenic assays to determine the effect of GMC in enhancing radiotherapy and DNA damage in 4T1 murine breast cancer cell lines. 4T1 cells were incubated with GMC or cell culture media overnight. The cells were washed twice before the radiation treatments. The cells were subsequently treated with an X-rays

ionizing radiation source, 320 kV, at 2, 4, and 6 Gy. The colony formations were monitored for 7 days. The data demonstrate that GMC enhance the sensitization of radiotherapy at 4 and 6 Gy. The cell survival fractions decrease 4.33-fold and 4.25-fold at 4 and 6 Gy respectively; although, there was no different in survival fraction at 2 Gy because the dose is too low to sensitize the ejection of electrons on Au shells (figure 4). The previous studies also reported the similar effect at the dose of 2 Gy with low concentration of AuNP[22,24]. The enhanced sensitization of the radiotherapy can dramatically improve the treatment and minimize the adverse effects of high dose radiation treatments. The enhanced sensitization of radiation by AuNP results from first, the exponential release of Auger electrons from shells of Au atom after being triggered by the radioactive source causing a vast generation of reactive radical species locally. Second, the AuNP internalized into the cells and colocalized at the cytosolic membrane and endosome, which have a proximal distance to the nucleus, leading to the higher DNA damage and affect cell proliferation and apoptosis[10,25,26]. However, the *in vivo* intravenous dose of 1.9 nm gold nanoparticles used for ionizing radiation is extremely high (2.7g/kg) due to rapid renal clearance of the small gold nanoparticles. The time to peak of the tumor accumulation was 5 minutes after IV injection[20,27]. In order to avoid the rapid clearance of small AuNP, GMC could become a new alternative because the size of GMC is large enough to stay longer in body. Nevertheless, we hypothesize that after endosomal uptake in a cellular level, GMC could be degraded into small AuNP and excrete out of the body, while IONP in GMC could be metabolized into ferric and ferrous.

A.3.5 *In vitro* MRI and CT imaging of GMC

A computed tomography (CT) imaging are widely used in current clinical practice to cancer diagnosis. One of the most commonly used CT contrast agent is Iodine due to the high atomic number. AuNP are also a great candidate for CT imaging as Au atom has higher atomic number than Iodine. The X-ray beams exciting the electrons of Au atom to ionize cause resonance absorption from atom in the medium and increase the absorption coefficient of the medium[28]. AuNP yield a far higher attenuation of an X-ray beam than Iodine at the similar thickness and concentration[29]. We then examined the use of GMC for *in vitro* CT imaging. We first compared the CT imaging capability of Au micelles and our GMC to determine whether the insertion of IONP impact the ability of AuNP for CT imaging at the same concentration of Au. The data indicate the phantom CT images between the Au micelles and GMC have relatively similar contrast (figure 5a). We also determined the linear transformation of the measured attenuation coefficients demonstrating as Hounsfield unit (HU) based on the radiodensity of distilled water at standard pressure and temperature. The increased linear transformation for CT imaging using AuNP as a contrast agent began at the concentration of Au 0.5 mg/ml in both GMC and Au micelles (figure 5b). However, there was no significant different of the CT contrast between GMC and Au micelles, implying that GMC could be used as the CT contrast media similar to AuNP.

Another imaging technique widely used in hospital setting is magnetic resonance imaging (MRI). MRI provides a safer technique and higher resolution images compared to CT scan. IONP have been intensively studied for MRI as they can lower T_2 relaxation

resulting better contrast images. In our report, we determine if our GMC could be used for MRI. The phantom MRI shows that the GMC can clearly darken the solution providing a better contrast (figure 6a). Moreover, T_2 relaxivity of GMC is very high, 285 $mM^{-}1.S^{-1}$, which is much higher than the T_2 relaxivity of a commercial brand, Feridex, 98.3 $mM^{-1}.S^{-1}$ (figure 6b).

A.4 Conclusion

In this study, we developed gold/iron oxide nanoparticles encapsulated in polymeric micelles. GMC exhibit strong imaging properties for both CT and MRI, which is very useful for cancer diagnosis. Dual imaging can also be performed at the same time to increase the accuracy of tumor position and size. For treatments, these micelles demonstrate the enhanced ionizing radiation (IR) proved by the clonogenic assay. GMC also show a great photothermal property under NIR light. The temperature increases dramatically after NIR light trigger. Therefore, GMC is a very promising agent used for dual treatment for both ionizing radiation and photothermal therapy (PTT). We expect that the dual therapy of IR and PTT will improve the effectiveness of cancer treatment; however, more studies are needed.

A.5 Materials and methods

Materials: furfuryl alcohol (98%), triethanolamine (TEA,99%), dioxane (99.5%, extra dry), and1,1,2,2 tetrachloro ethane (TCE,98.5%) were purchased from Acros Organics. Petroleum ether (certified ACS grade), and dichloromehane (certified ACS grade) were

purchased from Fisher Scientific. Ethyl acetate (anhydrous, 99.8%), tetrahydrofuran (THF, anhydrous 99.8%), adipoyl chloride, bismaleimido diphynyl methane (BMD), Gold (III) chloride solution (99.99%), 1-dodecanethiol (98%), Tetraoctylammonium bromide (98%), Sodium borohydride, and dimethyl sulfoxide (DMSO, 99.5%) were purchased from Sigma-Aldrich. Thiol methoxy polyethylene oxide 5KDa was purchased from NanoCS. Doxorubicin HCl (99.5%) was purchased from Polymed therapeutics.

Synthesis of 2nm dodecenethiol gold nanoparticles: Two-phase method was used to synthesized 2nm dodecenethiol gold nanoparticles as reported by previous literature[30,31]. Briefly, an aqueous solution of gold (III) chloride solution (30mM) was homogeneously mixed with tetraoctylammonium bromide (50mM) in toluene. After the toluene phase became orange, the aqueous phase was discarded. Dodecanethiol (2mmol) was added into the toluene phase following by slowly dropping sodium borohydride (0.4M, 25 ml). The solution was stirred rigorously. The color of the solution changed from orange to deep brown within a few minutes. After the solution was stirred for 3 hours, the organic phase was separated and evaporated in rotation evaporator. The product was washed 3 times in 200 ml of ethanol to get rid of excess dodecenethiol.

Synthesis of homogeneous Au/IONP micelles (GMC): Oleic acid coated-IONPs (1mg) and dodecanethiol AuNPs (1 mg) were dissolved together in THF and subsequently added into 20 mg of DA-*b*-PEO solution in THF under stirring. The

resulting solution was slowly dropped into water under vigorous agitation. The product was purified twice by weight-separated centrifugation.

Characterization of nanoparticle: TEM imaging were prepared by the solvent evaporation method. Briefly, the solution (5 µL) of each sample were dropped onto carbon-coated copper TEM grids and allowed to dry overnight. TEM images were acquired on a transmission electron microscope (TEM, Phillips CM-100, 60 kV). Hydrodynamic diameters were measured by using Malvern Zeta Sizer Nano S-90. Concentrations of Au were quantified by Inductively Coupled Plasma - Optical Emission Spectroscopy (ICP-OES) (Perkin-Elmer Optima 2000 DV). The samples were digested in aqua regia overnight before measurement. Concentration of Fe was measured by colorimetric method. Briefly, 10 mL of GMC was digested in concentrated HCl solution. After two days, sodium citrate was added to adjust the solution pH to 3.5. Then 2 mL of hydroquinone (10 g/l) and 3mLof o-phenanthroline (2.5 g in 100 mL of ethanol and 900 mL of water) were added to the solution followed by adjusting to a specific volume using Milli-Q water. Five standard Fe solutions using $Fe(NH_4)_2(SO_4)_2.6H_2O$ were also made. To determine the solution concentration of iron, calibration curves were generated by measuring the optical absorbance of solutions at 508 nm.

Cell uptake study: 4T1 murine breast cancer cell were seeded in 6-well plates at the density of 0.45 million cells/plate. The cells were incubate at 37 °C overnight and next day GMC (50nM) were incubated with the cells with or without magnet-induce cell uptake. The cells were washed twice by phosphate buffer saline (PBS) and digested

with aqua regia at 2, 4, and 6 hours for elemental analysis by ICP-OES. Standard curves for Au and Fe were generated using Yitrium as an internal standard.

Photothermal effect: IONP and GMC (0.2 mg/ml Fe, 100 ul) in aqueous media were exposed to NIR laser light 885 nm, 2.5 W/cm^2, spot size 5x8 mm. The temperature of the solutions was measured using a thermal camera (FLIR, Boston, MA).

Clonogenic assay: 4T1 were seeded at 5x104 cells/well in 6-well plates overnight to allow the cells attach to the plates. Next day, the cells were incubated with GMC or PBS. After 24 hours, the cells were irradiated at 2, 4, 6 Gy or mock radiation using X-rays orthovoltage 320kV. After the radiation, the cells were washed twice with PBS, trypsinized and seeded according to the radiation doses 0, 2, 4, and 6 Gy at the density of 100, 250, 1000, and 4000 cells/well in 6-well plates. The cells were maintained in 37 °C, 5% CO_2 for 7 days without changing media. The cells were then fixed with methanol: acetic acid 7:1 and stained with crystal violet. The colonies that contain $\geq$ 50 cells were counted. The surviving fraction was calculated as (colonies counted)/(cells seeded x (plating efficiency/100)). Each point on the survival curve were done in triplicate.

Phantom CT imaging: CT images were performed using Siemens Inveon with Au micelles or GMC at the concentration of Au 0, 0.1, 0.5, 1, and 2 mg/ml. Air was used to set the radiosensitivity at standard temperature and pressure as -1000 HU. The images were collected and the linear transformation of the measured attenuation coefficients

was calculated using an in-house software provided by Center for Molecular Imaging (CMI), University of Michigan.

Phantom magnetic resonance imaging: GMC at the concentration of Fe at 0, 0.018, 0.036, 0.09, 0.143, and 0.18 mM were constructed for MRI, T_2 mapping, and R_2 relaxivity. A multiecho fast spin-echo was used to simultaneously collect a series of data points at different echo times (TE = 15–90 ms with an increment of 15 ms). AN in-house software was used to calculated R_2 relaxivity.

A.6 Acknowledgements

Other people who contribute in this work include Dr. Hongwei Chen and Dr. Duxin Sun. We acknowledge Molecular Imaging Laboratory for transmission electron microscope, Center for Molecular Imaging (CMI), and the Experimental Irradiation Core. We thanks Dr.Mary Davis for advice regarding clonogenic assay.

A.7 References

1. Whelan, T. J. *et al.* Regional Nodal Irradiation in Early-Stage Breast Cancer. *N. Engl. J. Med.* **373,** 307–16 (2015).
2. Bonner, J. A. *et al.* Radiotherapy plus cetuximab for locoregionally advanced head and neck cancer: 5-year survival data from a phase 3 randomised trial, and relation between cetuximab-induced rash and survival. *Lancet Oncol.* **11,** 21–28 (2010).
3. Hamdy, F. C. *et al.* 10-Year Outcomes after Monitoring, Surgery, or Radiotherapy for Localized Prostate Cancer. *N. Engl. J. Med.* 1–10 (2016). doi:10.1056/NEJMoa1606220
4. Roach, M. *et al.* Phase III trial comparing whole-pelvic versus prostate-only radiotherapy and neoadjuvant versus adjuvant combined androgen suppression: Radiation Therapy Oncology Group 9413. *J. Clin. Oncol.* **21,** 1904–1911 (2003).
5. Ragaz, J. *et al.* Premenopausal Women With Breast Cancer. *N. Engl. J. Med.* **337,** 956–62 (1997).
6. Cooper, D. R., Bekah, D. & Nadeau, J. L. Gold nanoparticles and their alternatives for radiation therapy enhancement. *Front. Chem.* **2,** 1–13 (2014).
7. Patel, R. R. & Arthur, D. W. The emergence of advanced brachytherapy techniques for common malignancies. *Hematol. Oncol. Clin. North Am.* **20,** 97–118 (2006).
8. Kwatra, D., Venugopal, A. & Anant, S. Nanoparticles in radiation therapy : a summary of various approaches to enhance radiosensitization in cancer. *Transl. Cancer Res.* **2,** 330–342 (2013).
9. Townley, H. E., Rapa, E., Wakefield, G. & Dobson, P. J. Nanoparticle augmented radiation treatment decreases cancer cell proliferation. *Nanomedicine Nanotechnology, Biol. Med.* **8,** 526–536 (2012).
10. Chang, M. Y. *et al.* Increased apoptotic potential and dose-enhancing effect of gold nanoparticles in combination with single-dose clinical electron beams on tumor-bearing mice. *Cancer Sci.* **99,** 1479–1484 (2008).
11. Roa, W. *et al.* Gold nanoparticle sensitize radiotherapy of prostate cancer cells by regulation of the cell cycle. *Nanotechnology* **20,** 375101 (2009).
12. Kim, D., Park, S., Jae, H. L., Yong, Y. J. & Jon, S. Antibiofouling polymer-coated gold nanoparticles as a contrast agent for in vivo X-ray computed tomography imaging. *J. Am. Chem. Soc.* **129,** 7661–7665 (2007).
13. Shen, S. *et al.* Magnetic nanoparticle clusters for photothermal therapy with near-infrared irradiation. *Biomaterials* **39,** 67–74 (2015).
14. Zhen, G. *et al.* Comparative Study of the Magnetic Behavior of Spherical and Cubic Superparamagnetic Iron Oxide Nanoparticles. *J. Phys. Chem. C* **115,** 327–334 (2011).
15. Laurent, S. *et al.* Magnetic iron oxide nanoparticles: synthesis, stabilization, vectorization, physicochemical characterizations, and biological applications. *Chem. Rev.* **108,** 2064–110 (2008).
16. Weissleder, R. A clearer vision for in vivo imaging. *Nat. Biotechnol.* **19,** 316–317 (2001).
17. Loo, C., Lowery, A., Halas, N., West, J. & Drezek, R. Immunotargeted nanoshells for integrated cancer imaging and therapy. *Nano Lett.* **5,** 709–11 (2005).
18. Kennedy, L. C. *et al.* A new era for cancer treatment: gold-nanoparticle-mediated thermal therapies. *Small* **7,** 169–83 (2011).
19. O'Neal, D. P., Hirsch, L. R., Halas, N. J., Payne, J. D. & West, J. L. Photo-thermal tumor ablation in mice using near infrared-absorbing nanoparticles. *Cancer Lett.* **209,** 171–6 (2004).

20. Hainfeld, J. F., Slatkin, D. N. & Smilowitz, H. M. The use of gold nanoparticles to enhance radiotherapy in mice. *Phys. Med. Biol.* **49,** N309–N315 (2004).
21. Hainfeld, J. F., Smilowitz, H. M., O'Connor, M. J., Dilmanian, F. A. & Slatkin, D. N. Gold nanoparticle imaging and radiotherapy of brain tumors in mice. *Nanomedicine (Lond).* **8,** 1601–9 (2013).
22. Zhang, X. D. *et al.* Enhanced tumor accumulation of Sub-2 nm gold nanoclusters for cancer radiation therapy. *Adv. Healthc. Mater.* **3,** 133–141 (2014).
23. Hainfeld, J. F. *et al.* Infrared-Transparent Gold Nanoparticles Converted by Tumors to Infrared Absorbers Cure Tumors in Mice by Photothermal Therapy. *PLoS One* **9,** e88414 (2014).
24. McQuade, C. *et al.* A Multifunctional Nanoplatform for Imaging, Radiotherapy, and the Prediction of Therapeutic Response. *Small* 1–10 (2014). doi:10.1002/smll.201401927
25. Raoof, M. *et al.* Gold nanoparticles and radiofrequency in experimental models for hepatocellular carcinoma. *Nanomedicine Nanotechnology, Biol. Med.* **10,** 1121–1130 (2014).
26. Yang, Y.-S., Carney, R. P., Stellacci, F. & Irvine, D. J. Enhancing Radiotherapy by Lipid Nanocapsule-Mediated Delivery of Amphiphilic Gold Nanoparticles to Intracellular Membranes. *ACS Nano* 8992–9002 (2014). doi:10.1021/nn502146r
27. Hainfeld, J. F. *et al.* Gold nanoparticles enhance the radiation therapy of a murine squamous cell carcinoma. *Phys. Med. Biol.* **55,** 3045–3059 (2010).
28. Xi, D. *et al.* Gold nanoparticles as computerized tomography (CT) contrast agents. *RSC Adv.* **2,** 12515 (2012).
29. Jackson, P. A., Rahman, W. N. W. A., Wong, C. J., Ackerly, T. & Geso, M. Potential dependent superiority of gold nanoparticles in comparison to iodinated contrast agents. *Eur. J. Radiol.* **75,** 104–109 (2010).
30. Frenkel, a. I. *et al.* Size-controlled synthesis and characterization of thiol-stabilized gold nanoparticles. *J. Chem. Phys.* **123,** 1–6 (2005).
31. Brust, M., Walker, M., Bethell, D., Schiffrin, D. J. & Whyman, R. Synthesis of thiol-derivatised gold nanoparticles in a two-phase Liquid–Liquid system. *J. Am. Chem. Soc.* **7,** 801–802 (1994).

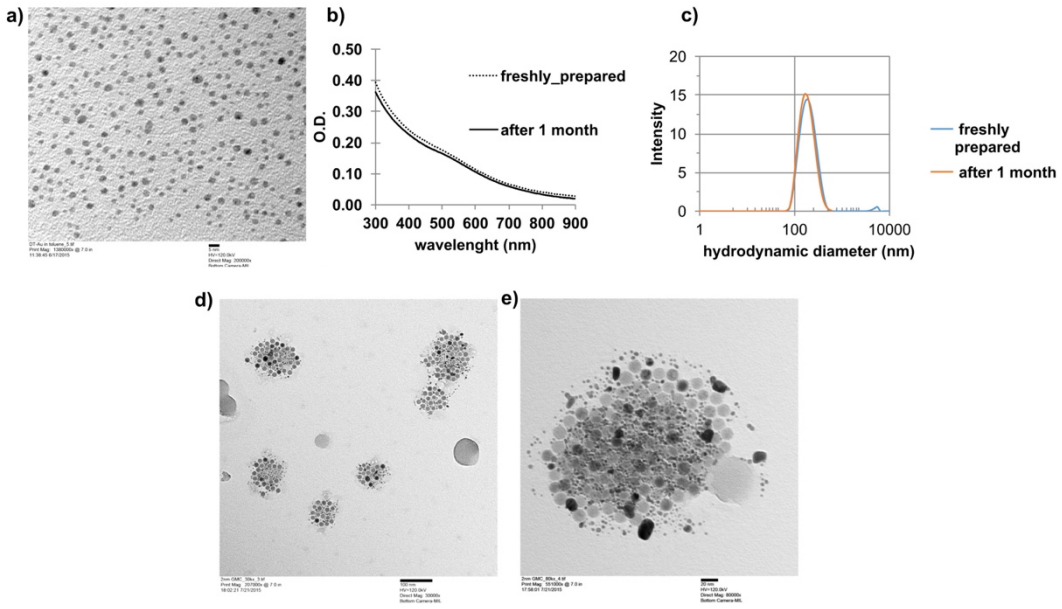

Figure A.1. a) a TEM image of 2nm dodecenethiol-coated AuNP synthesis by two-phase method. b) absorption spectra of freshly prepared and a month after prepared dodecenethiol-coated AuNP. The absorption spectra remain the same after one month of storage at 4 °C indicating a good stability of the dodecenethiol AuNP. 2 nm AuNP lack of absoption peak at 520 nm due to ultra small size. c) The chart shows hydrodynamic diameter of GMC *ca* 172.7 nm with PDI 0.106. The size of freshly prepared GMC and after being stored for a month are similar suggesting that GMC is stable for over a month. d) a TEM image of GMC demonstrates a homogeneously mixed between 2 nm AuNP and 15 nm IONP in GMC. e) a high magnification of GMC. AuNP and IONP form a cluster inside a hydrophobic core of the polymer.

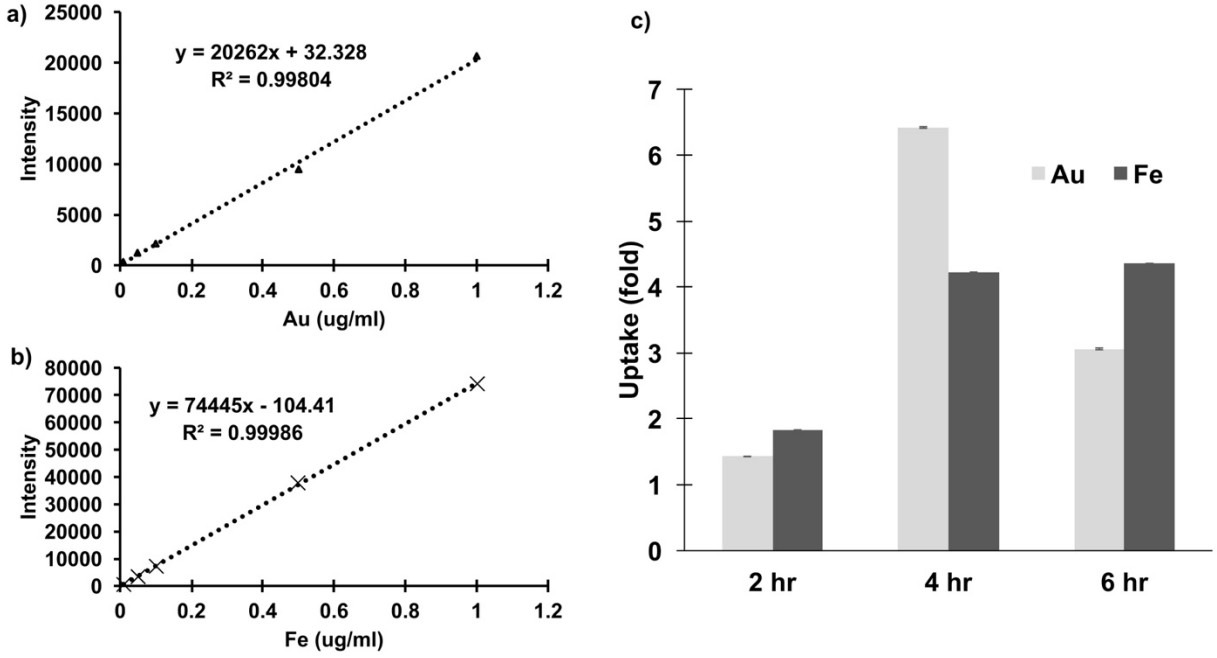

Figure A.2. a) and b) calibration curves of standard Au and Fe measured by ICP-OES. c) The graph shows the fold of the amount cell uptake of Au and Fe from GMC. The fold changes were calculated by the amount of the determined elements found in the cells induced by magnet divided by the amount of the determined elements found in the cells without magnet induction. The amount of Au is enhanced by the magnet induction because the AuNP were encapsulated in the same micelles with IONP. The peak time of magnet-induce Au uptake is at 4 hours. The amount of Au in cells was 6.4-fold higher with magnet induction compared to no magnet induction.

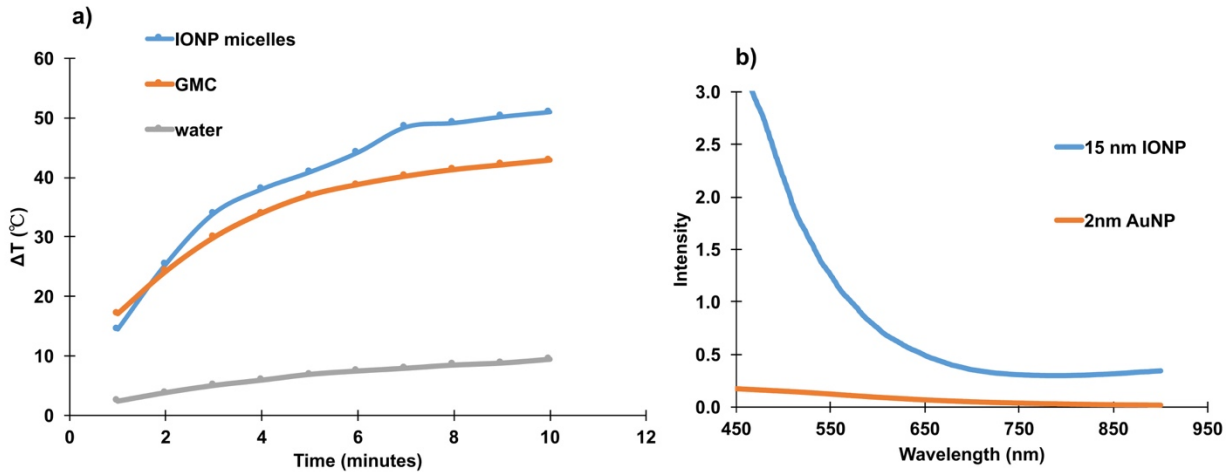

Figure A.3. a) The photothermal effect of IONP micelles, GMC, and water control during 10 minutes of NIR laser light irradiation at 885 nm, 2.5 W/cm^2 with a spot size of 5x8 mm. b) the absorption spectra of IONP and AuNP. IONP can absorb the NIR light, while 2 nm AuNP lack of light absorption.

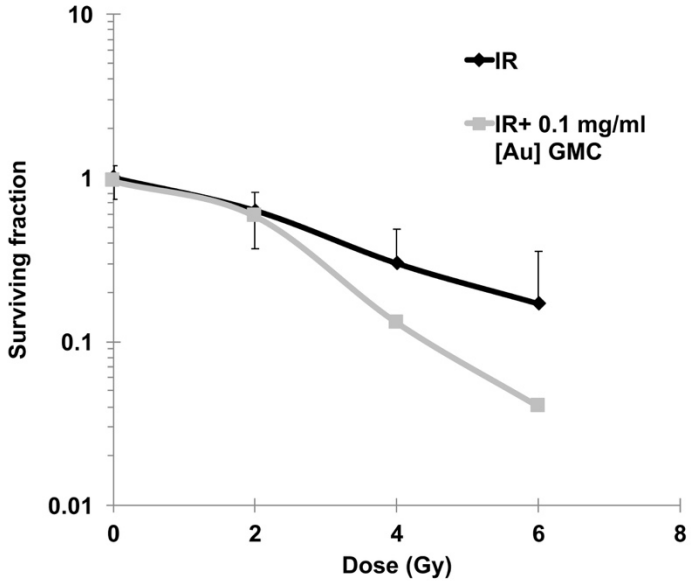

Figure A.4. The chart presents the surviving fraction of clonogenic assays at different irradiation doses. The data suggest that GMC at the concentration of Au 0.1 mg/ml enhance cell death after radiation treatment at dose 4, and 6 Gy.

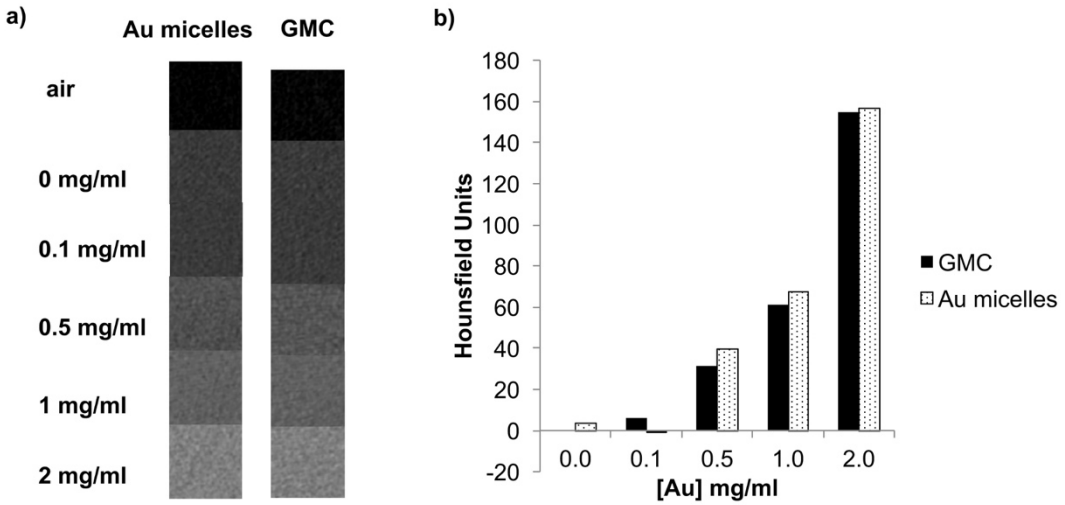

Figure A.5. Phantom CT scans of Au micelles and GMC at the same concentration of Au. a) Both GMC and Au micelles provide good contrast images indicating that the insertion of IONP in GMC does not impact the CT imaging property of AuNP. b) The linear transformation of the measured attenuation coefficients demonstrating as Hounsfield unit (HU) based on the radiodensity of distilled water at standard pressure and temperature. The increased linear transformations for CT imaging between Au micelles and GMC are relatively close and significantly different from water at the concentration of Au is equal to 0.5 mg/ml.

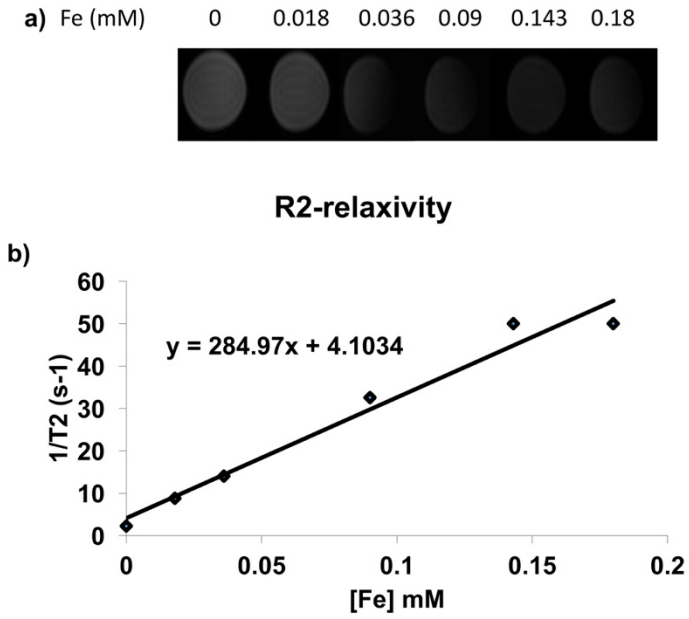

Figure A.6. GMC as an MRI contrast agent. a) A phantom MRI images at different concentration of Fe in GMC. The images show that GMC can increase the contrast of the solution in a Fe concentration dependence. b) The R_2 relaxivity was calculated from the T_2 relaxation of the solution.